CFD analysis to predict the effects of low-temperature heating on thermal comfort in a generic office

Pelkmans, Dean D.J.

Award date:
2021

CFD analysis to predict the effects of low-temperature heating on thermal comfort in a generic office

Author:
D.D.J. (Dean) Pelkmans

Supervisors:
dr. ir. Twan van Hooff,
dr. Luyang Kang,
Eindhoven University of Technology
ir. Marieke Krijnen
Royal HaskoningDHV

A thesis submitted in fulfillment of the requirements for the degree of Master in Building Physics and Services

in the

Department of the Built Environment

Eindhoven, July 2021

Student	D.D.J. (Dean) Pelkmans
Study load graduation	45 ECTS
Year of graduation	2021
Master's program	Architecture, Building and Planning
Master track	Building Physics and Services

This Master's thesis has been carried out with the rules of the TU/e Code of Scientific Integrity and is public information

Abstract

The built environment is responsible for approximately 40 % of the annual energy consumption. To reach sustainability goals soon, it is required to transition towards more efficient energy usage. This transition can be achieved in multiple ways, however, in this research, the implementation of a more efficient heating system (i.e. low-temperature heating) is investigated. The transition alone cannot be achieved without focussing on thermal comfort as people spend nowadays approximately 85 to 90 % of their time indoors. Therefore, the two are interconnected with each other.

Royal HaskoningDHV developed a Low-Temperature Calculator tool in which they assess the thermal comfort in the transition to energy efficiency related to low-temperature heating systems. However, the tool is based upon empirical formulae from literature and therefore the accuracy is considered to be questionable. The subject of the research is therefore to investigate through computational fluid dynamics (CFD) whether the transition from a traditional high-temperature to a low-temperature heating system can occur without a decrease in the thermal comfort perception.

In the Netherlands, there is a large retrofitting assignment for offices to acquire an energy label C classification. Therefore, the research is conducted in a generic office model using building and installation characteristics from the building period 1988 to 1992. In the transition from high-temperature to low-temperature heating, two approaches were defined. An immediate approach in which the traditional radiator is completely removed by a climate ceiling. Furthermore, a more step-wise approach is considered in which the capacity of the radiator is lowered (i.e. medium-temperature and low-temperature) and the loss in capacity is solved with a percentage of climate ceiling.

It is concluded from the research that the scenarios defined to transition from a high-temperature to a low-temperature heating system can be achieved without decreasing the thermal comfort compared to the initial scenario. However, in the case of the replacement of the radiator with the climate ceiling, it is required to provide additional measures in the thermal performance of the transparent facade element. Furthermore, it is concluded that the empirical formulae in the Low-Temperature Calculator tool of Royal HaskoningDHV provide results that are within the limits of the CFD results. Therefore, the use of the tool is considered to be accurate for the desired function.

Preface

The journey at the TUe started almost three years ago with the mission to improve and expand my knowledge concerning physics in the built environment which was lacking through my Bachelor's. What a journey it has been! I can proudly say that every step has been an experience that contributed to some extent to the person I am right now. The effort to improve and expand has resulted in the thesis which marks the end of this journey with gratitude.

I would like to thank the team of Royal HaskoningDHV and in particular Marieke Krijnen for providing the opportunity to graduate under their guidance throughout the process. The enthusiastic discussions we had given me insights into the strong connection between science and practice related to the subject. Furthermore, I would like to thank Twan van Hooff for his guidance and extensive knowledge of the performance of the simulations concerning the subject. Also, my gratitude to Luyang Kang for his role as advisor in conducting the simulations of the generic office case and as a supervisor in the final stage of the graduation.

Although the journey was joyful, there were moments in which my family, friends, and especially my girlfriend Fenne have played an enormous role in the motivation. Therefore, I would also like to dedicate the effort I made to them!

Contents

Nomenclature

List of symbols and acronyms

A	surface area [m^2]	R_l	heat resistance air to air [m^2·K/W]
A_i	effective surface area [m^2]	R_n	heat resistance of layer n [m^2·K/W]
c_p	specific heat capacity [J/kg·K]	RMSE	root-mean-square error [-]
D_H	hydraulic diameter [m]	t	outlet height [m]
DR	draught rate [%]	T	mean static temperature [°C]
E	heat load [W]	T_a	temperature at ankle level [°C]
FAC1.1	factor of 1.1 of the observations [-]	$T_{a,v}$	temperature gradient head and ankle [°C]
FAC1.3	factor of 1.3 of the observations [-]	T_f	Floor surface temperature range [°C]
FAC2	factor of 2 of the observations [-]	T_i	supply temperature [°C]
F_{p-n}	angle factor [-]	T_{ic}	ceiling surface temperature [°C]
F_s	safety factor[-]	T_{if}	floor surface temperature [°C]
h	inlet height [m]	T_n	temperature jump across layer n [°C]
H	height [m]	T_{op}	operative temperature [°C]
I	turbulence intensity [%]	T_r	heating system return temperature [°C]
k	turbulence kinetic energy [m^2/s^2]	T_s	heating system supply temperature [°C]
l_0	length scale [m]	T_v	temperature at head level [°C]
L	length [m]	T_o	backflow temperature [°C]
MRT	mean radiant temperature [°C]	U	velocity magnitude [m/s]
n	supply flow rate [h^{-1}]	U_0	inflow velocity [m/s]
O_i	observed value [-]	W	width [m]
p	formal order of accuracy [-]	V_{hs}	volume of heat source [m^3]
P	perimeter [m]	V	volume [m^3]
P_i	predicted value [-]	y^*	dimensionless wall distance [-]
q	volumetric heat generation [W/m^3]		
Q	volumetric flow rate [m^3/s]	ϵ	turbulence dissipation rate [m^2/s^3]
r	linear refinement factor [-]	λ	thermal conductivity [W/m·K]
R_{se}	external heat resistance [m^2·K/W]	ν	kinematic viscosity [m^2/s]
R_{si}	internal heat resistance [m^2·K/W]	ρ	density [kg/m^3]
Re	Reynolds number [-]		

List of abbreviations

2D	two-dimensional	LTH	low-temperature heating
3D	three-dimensional	LTC	low temperature calculator
CFD	computational fluid dynamics	MTH	medium-temperature heating
EWT	enhanced wall treatment	RANS	Reynolds-averaged Navier-Stokes
EXP	experiment	RNG	renormalization group k-ϵ turbulence model
GCI	grid-convergence index	SKE	standard k-ϵ turbulence model
HTH	high-temperature heating	SST	shear stress transport k-ω turbulence model
IEA	International Energy Agency	S2S	surface-to-surface radiation model
LRNM	low-Reynolds number modeling		

1 — Introduction

1.1 Background

The built environment in the Netherlands is responsible for approximately 40% of the total annual energy consumption. The transition within the built environment is required to achieve future energy-neutral targets defined by the government and other relevant organizations. Different measures can be implemented to reduce the annual fossil energy consumption of a building (e.g. retrofitting of the facade, improving the installation efficiency, and increase the use of renewable energy sources). The measure of interest within the subsequent research is the transition from traditional high-temperature heating (HTH systems (i.e. radiator or convector) to more efficient systems such as medium-temperature (MTH) and low-temperature heating (LTH) systems (e.g. climate ceiling, floor heating, etc.) [1]. The traditional HTH system uses a medium that is heated to temperatures in between 60 and 80 °C [2]. However, the more efficient MTH and LTH systems use a medium that is heated to lower temperatures (i.e. MTH = 40 to 60 °C, and LTH = 30 to 35 °C) [2]. Therefore, the implementation of these systems is desired as the energy usage decreases significantly.

However, removing the traditional systems could cause problems related to comfort in some building configurations. The traditional systems are often placed underneath transparent facade elements to provide a counteracting upward motion on the downdraught generated on the facade [3]. The downdraught is generated as the interior surface temperature of the transparent facade element causes a temperature gradient between the surface and the surrounding air in the building. Under the influence of the temperature gradient, a downward flow (i.e. downdraught) is experienced. Replacing the traditional system with the more energy-efficient MTH and LTH can decrease the counteracting upward motion and result in a decrease in comfort within the enclosure. As people nowadays spend between 85 and 90 % of their time indoors, it is important to achieve comfortable conditions which did not decrease from the initial situation [4] [5]. Therefore, the question arises whether the desired and required energy transition from HTH to LTH can provide similar or improved thermal comfort conditions compared to the initial situation.

1.2 Problem statement

Royal HaskoningDHV (RHDHV) uses a Low-temperature calculator (LTC) tool to assess whether the transition from a high-temperature to a low-temperature heating system decreases the thermal comfort perception in an enclosure. The LTC tool assesses thermal comfort based on empirical formulae which were derived from literature. These formulae, however, were derived from experimental and numerical studies which show several limitations compared to more realistic conditions (i.e. an empty room with no counteracting devices such as ventilation or heating) [6] [7].

RHDHV uses the LTC tool in the design phase of new buildings and the renovation of existing buildings to assess the thermal comfort. However, the results obtained in multiple building configurations deviate from realistic conditions (e.g. velocity in the occupied zone due to downdraught) and therefore the use of the LTC tool remains questionable. Through the conducted research answers will be provided in terms of accuracy of the LTC tool and whether improvements are needed.

1.3 Research objective

The main objective of the research is to investigate the effect of the transition from HTH to LTH systems on the thermal comfort perceived in an enclosure, with the use of computational fluid dynamics (CFD). The numerical results obtained through CFD provide extensive information on expected thermal comfort and downdraught conditions in an enclosure. Furthermore, the numerical results can be used to quantify the difference with the LTC tool under similar conditions in multiple configurations.

The main research question was developed together with RHDHV:

- Is it possible to transition from a traditional high-temperature heating system to a low-temperature heating system and realize thermal comfort conditions which are similar or improved compared to the initial case?.

In addition, one sub-question is formulated:

- Is the LTC tool accurate enough to assess thermal comfort in the transition from high-temperature heating to a low-temperature heating system?

1.4 Methodology and outline

To understand the influence of the transition from HTH to LTH on the flow regime and thermal comfort perception within an indoor environment, multiple methods can be distinguished: literature research, on-site measurements (i.e. full-scale), and CFD simulations. The use of CFD was considered to be advantageous compared to experimental testing within the conducted research. The simulations are relatively inexpensive and fast, are performed under well-controlled conditions to provide whole-flow field data of multiple flow variables, and allow parametric studies to be performed and evaluated. However, the accuracy and reliability of the results remain a concern, and therefore verification and validation are imperative [8]. Furthermore, literature research was conducted to provide a theoretical background on the research subject. The methodology used within the research is schematically depicted in Figure 1.1.

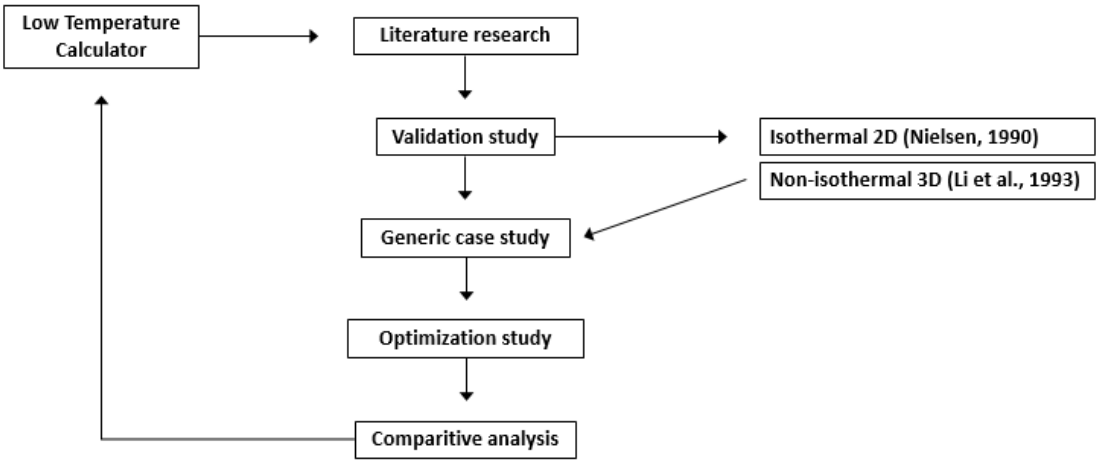

Figure 1.1: Methodology

In Chapter 2 more in-depth information is provided on the evaluation of thermal comfort, the LTC tool, the physics related to downdraught on a vertical surface, the empirical formulae used to assess downdraught, and findings of reference studies related to downdraught are summarized. Chapter 3 describes the characteristics of the case study which will be used to answer the research questions. Chapter 4 presents a twofold validation study, namely a two-dimensional (2D) isothermal benchmark test by Nielsen [9] and a three-dimensional (3D) non-isothermal full-scale experimental study by Li et al. [10]. In Chapter 5, the generic office model is further defined and multiple transition scenarios were investigated by conducting 3D steady Reynolds-averaged Navier-Stokes (RANS) simulations. In Chapter 6, the results of the numerical simulations are summarized. Chapter 7 presents an optimization study in which one transition scenario is subjected to improvement in terms of the installation concept and thermal performance of the transparent element of the facade. In Chapter 8 a comparative analysis is performed between the empirical and numerical results and the reliability of the LTC tool is evaluated. Chapter 9 discusses the overall findings and limitations of the research. Finally, in Chapter 10 the overall conclusion of the research is formulated.

2 — Theoretical background

This chapter is devoted to providing information on the evaluation of thermal comfort, understanding the physical nature of convection (i.e. downdraught), providing an overview of the empirical formulae derived in literature to assess downdraught, and summarize important findings related to downdraught concluded from multiple experimental and numerical studies from literature.

2.1 Thermal comfort

Thermal comfort is defined as the condition of mind which expresses satisfaction with the current thermal environment [11]. Dissatisfaction in comfort perception can be caused due to warm or cool discomfort on the whole body and/or unwanted local heating or cooling of an individual part of the body. The assessment of thermal comfort can be used to check the current environment with the use of multiple comfort criteria and to formulate requirements for improvement [11].

To perceive thermal comfort, the human body has to meet three conditions according to Fanger: the body is in heat balance through thermoregulation, the influence of the mean skin temperature and sweat rate is limited, and no local discomfort exists [12]. To relate the physical processes described to perceived thermal comfort, Fanger derived a thermal comfort equation that was based on the results of an experimental study. The experimental study was conducted with college-aged students which were exposed to steady-state conditions in a climate chamber wearing standardized clothing and performing standardized activities under different thermal conditions [12]. The participants of the experiment scored the perceived thermal sensation on a 7-point ASHRAE scale (i.e. +3 = hot, +2 = warm, +1 = slightly warm, 0 = neutral, -1 = slightly cold, -2 = cool, and -3 cold) [11]. An acceptable comfort perception was considered for the points +1 to -1 (i.e. slightly warm to slightly cold).

To create a predictive model which is applicable for different types of people in multiple building and climate configurations, Fanger derived the Predicted Mean Vote (PMV) model [12]. The model includes the measured environmental parameters air temperature (T), mean radiant temperature (MRT), air velocity (U), and relative humidity (RH) combined with the estimated activity level (MET) and insulation of the clothing (Clo) [12]. It presents an index that predicts the mean thermal sensation on the 7-point scale for a reference group under multiple thermal conditions, activity, and clothing levels. this resulted in the adaptation of the PMV model in multiple (inter)national standards and guidelines (i.e. NEN-EN-ISO 7730, ANSI/ASHRAE Standard 55, and CEN CR 1752). However, over the past years, the model received some criticism related to its geographical application, the use within different types of building and model input, and the representativeness of the conducted experiment [12].

As mentioned above, the PMV provides a mean value of the thermal sensation of a reference group exposed to similar environmental conditions. However, it does not include the thermal sensation which was scattered around the mean value according to the 7-point ASHRAE scale [12]. Therefore, in addition, the Predicted Percentage Dissatisfied (PPD) index was derived which provides a quantitative prediction of the percentage of dissatisfied people who feel uncomfortable in the current environment (i.e. either too warm or too cold) [11]. The remaining part of the reference group compared to the percentage dissatisfied will score the environment either slightly warm, neutral, or slightly cold.

Local thermal comfort causes dissatisfaction due to the unwanted cooling or heating of one particular body part and is mainly perceived by people performing light sedentary activities (i.e. metabolism of $\leq$ 70 W/m^2) [11]. The local discomfort can be caused through draught (DR) defined as an unwanted local convective cooling of the body, vertical air temperature gradients which causes local warm discomfort at the head and/or cold discomfort at the ankle of a seated person ($\Delta T_{a,v}$), too cold or too warm floor surface which is in direct contact with the feet (T_f), and asymmetry radiation caused by cold windows, uninsulated walls, or heating and cooling panels in the ceiling or wall [13]. The local discomfort parameters are quantified according to the percentage dissatisfied (PD) under particular conditions except for draught [11]. Draught is found to be more critical related to the other local thermal discomfort parameters and depends on the variables air velocity U, air temperature T, and turbulence intensity I [7].

Individual differences between people make it impossible to specify thermal conditions that satisfy everybody. However, certain conditions can be specified based on the percentage of dissatisfaction which is considered to be acceptable by the occupants of that environment. The thermal environment can be selected based on three categories (i.e. A to C) in which the whole body thermal sensation indices PMV and PPD, as well as the local discomfort parameters, are prescribed through maximum values (see Figure 2.1) [11]. In general, it can be stated that in practice existing buildings have the category C classification and a newly built building should always have at least the category B classification. It should be noted that the criteria to assess thermal comfort should meet the requirements simultaneously to obtain a specific category classification.

Category	Thermal state of the body as a whole		Local discomfort			
	PPD %	PMV	DR %	PD % caused by		
				vertical air temperature difference	warm or cool floor	radiant asymmetry
A	< 6	− 0,2 < PMV < + 0,2	< 10	< 3	< 10	< 5
B	< 10	− 0,5 < PMV < + 0,5	< 20	< 5	< 10	< 5
C	< 15	− 0,7 < PMV < + 0,7	< 30	< 10	< 15	< 10

Figure 2.1: Overview of maximum values for the indices PMV and PPD and local discomfort parameters per category [11]

2.2 Low Temp Calculator

The developed LTC tool by RHDHV assesses whether the transition from the traditional high-temperature systems to the desired low-temperature systems influences the thermal comfort perceived at an arbitrary point in an enclosure. It also evaluates whether the installed capacity in the initial building configuration provides enough possibilities to transition to low-temperature heating. The LTC tool is built in a Microsoft Excel environment which allows the user to evaluate multiple building configurations and conditions with relative ease through the use of (empirical) formulae. The initial results can then be fitted according to the desired thermal comfort as the input can be changed.

The LTC tool requires the input of the building characteristics (i.e. dimensions, thermal performance of the facade, and heating system), conditions (i.e. indoor and outdoor temperature), and assumptions for PMV (i.e. clo value, metabolic rate, relative humidity) to estimate the thermal comfort. Thermal comfort is evaluated at an arbitrary point of choice through the parameters: draught rate (DR), operative temperature T_{op}, the radiant asymmetry caused by a cold or warm ceiling or floor, and the PMV and PPD indices.

The LTC tool calculates the interior surface temperature of the opaque and transparent facade elements based on the specified indoor and outdoor temperature, and their thermal performance (i.e. U-factor for transparent ($W/m^2 \cdot K$) and R_c-value for opaque ($m^2 \cdot K/W$)). The surface temperature of the internal structures (i.e. walls, floor, and ceiling) can be defined according to the excepted conditions. The presence of a heating system (i.e. radiator or radiant panel) is modeled in the calculation as a planar surface with a surface temperature assigned to it. Once the surface temperatures are known in the enclosure, the operative temperature T_{op} and radiant asymmetry can be calculated through the use of standard formulae. DR is evaluated through the use of empirical formulae by Heiselberg which evaluate the maximum air velocity U_{max} near the floor region and the minimum air temperature T in the enclosure. Furthermore, the PMV and PDD indices are evaluated in the arbitrary point combining the assumptions made in terms of clo value, metabolic rate, and relative humidity, and the calculated parameters through the formulae.

2.3 Physical nature of downdraught

Convection can be differentiated based on two different mechanisms which generate the flow. Forced convection in which an external agent (i.e. fan or blower) is used to create motion that drives upon pressure differences. Natural convection in which no external agent is used and the motion of the fluid arises from differences in density [14]. The density can differ due to differences in temperature, concentration, and the presence of multiple phases within a fluid [15]. Therefore, the flow regime in natural convection is often not known beforehand compared to forced convection as it drives upon heat and mass transfer [14].

The physical nature of natural convection is further explained through heat transfer occurring from a heated vertical surface placed within an extensive medium of uniform temperature (see Fig. 2.2a) [14]. The fluid particles moving parallel to the vertical surface are heated through the mechanism of conduction as the surface temperature T_w is higher than the surrounding air temperature T_∞. As a result, the kinetic energy content of the fluid particles increases which decreases the density (i.e. thermal expansion). Due to the influence of the gravitational force g, buoyancy forces are generated which creates an upward motion in the fluid [15]. The upward motion persists as adjacent fluid particles move towards the position of the initially heated particles due to pressure differences.

The opposite is true for a fluid moving parallel to a cooled vertical surface in which the density increases due to a decrease in kinetic energy (i.e. thermal contraction). In that particular case (i.e. downdraught), a downward motion is generated under the influence of buoyancy forces (see Fig. 2.2b).

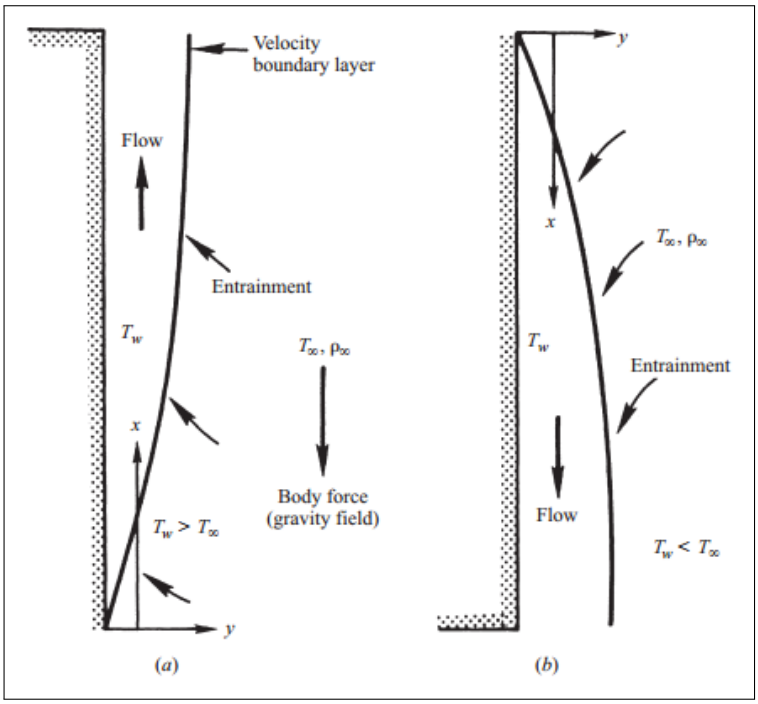

Figure 2.2: Natural convection flow over a heated and cooled vertical surface [14]

The vertical motion caused by the buoyancy forces is initially confined to a thin layer close to the vertical surface (i.e. natural-convection boundary layer) in which viscous forces are dominant [16]. In the origin of the boundary layer, the thickness of the layer is zero and increases as the flow proceeds up or downward due to a loss in momentum (see Fig. 2.2). The loss in momentum is caused by the fact that the fluid at the vertical surface satisfied the no-slip boundary condition. The no-slip condition assumes that the fluid has zero vertical velocity as the adhesive forces between the fluid-solid interface are stronger than the cohesion forces between the fluid-fluid interface. The boundary layer thickness, therefore, increases under the influence of the no-slip condition due to a decrease in momentum affecting adjacent fluid particles further away from the origin.

The temperature and velocity distribution within the natural-convection boundary layer are explained through the previously used example of a heated vertical surface (see Fig. 2.2) [14]. In the close vicinity of the vertical surface, the resistant force due to viscosity is too large for the buoyancy forces to overcome. Therefore, no upward motion is generated and heat transfer between the vertical surface and adjacent fluid occurs due to molecular heat diffusion (i.e. conduction) [14]. Further from the vertical surface, the buoyancy forces overcome the resistant force and through convection, the maximum velocity is achieved at a certain distance y. The temperature distribution will further decrease from the vertical surface until an equilibrium is achieved with the surrounding air temperature T_∞.

In the case of a cooled vertical surface, the temperature increases from the vertical axis until an equilibrium is achieved with the warmer surrounding air. The velocity distribution will be facing downward instead of upward as displayed in Figure 2.3.

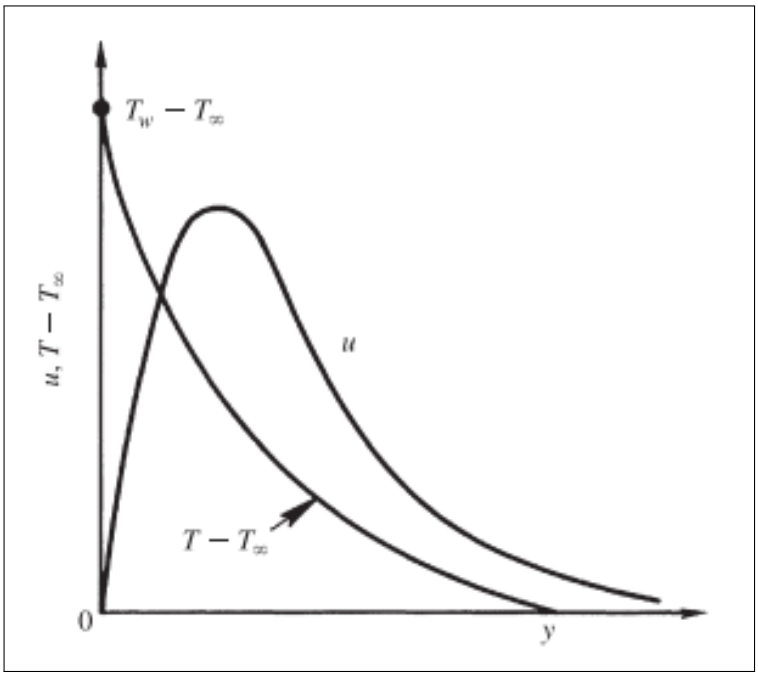

Figure 2.3: The velocity and temperature distribution in the natural convection flow over a vertical heated surface [14]

The above-mentioned characteristics of the natural-convection boundary layer are formulated for flows in an extensive medium. However, internal flows as considered within the research occur in a more confined enclosure and under the influence of different flow phenomena (i.e. separation, recirculation, etc.). To provide an example, Bejan et al. [14] concluded that a recirculation flow occurring within a more confined enclosure distorted the temperature field generated through conduction close to the vertical surface. Therefore, the accuracy in the near-wall region is of great importance to predict the temperature and velocity distributions correctly in internal natural convection flows.

2.4 Empirical formulae

Downdraught can be assessed in a preliminary phase of a design with the use of multiple formulae or so-called rules of thumb derived through experimental and numerical studies. In the assessment of downdraught from two parameters play an important role, namely the heat transmittance (U-factor) and the dimensions of the window [17].

Olesen [18] combined the above-mentioned parameters in two rules of thumb to indicate whether an allowable maximum velocity U_{max} would be exceeded within an enclosure. The formulae can be used for multiple transparent facade constructions in which U_{glass} decreases and will result in the allowance of larger window heights [17]. U_{max} can be estimated to prevent thermal comfort problems within the vicinity of cold vertical surfaces using Eqs. (2.1a and 2.1b) for the threshold values of 0.15 and 0.18 m/s:

$$U_{glass} \cdot h \leq 4.7 \qquad U_{max} = 0.18 \tag{2.1a}$$

$$U_{glass} \cdot h \leq 3.2 \qquad U_{max} = 0.15 \tag{2.1b}$$

where U_{glass} is the heat transmittance of the window glazing ($W/m^2 \cdot K$) and h the window height (m). The negative influence of the window frame can be implemented in the empirical formulae by calculating the combined heat transmittance of the window including the frame (i.e. U_{fr}) [17].

In addition, Eckert and Jackson [19] derived a formula to estimate U_{max} at the foot of a cold surface rather than within the occupied zone [19]. Solving the boundary layer equations of a turbulent flow structure on a flat plate resulted in the estimation of U_{max} using Eq. (2.2):

$$U_{max} = k \cdot \sqrt{\Delta\theta \cdot H} \tag{2.2}$$

where k is a coefficient determined by experimental studies ($m^{0.5}/K^{0.5}s$), $\Delta\theta$ the temperature difference between the surface and the surrounding air, and H the surface height. The influence of U_{max} on thermal discomfort, however, is more important within the occupied zone rather than at the foot of the cold surface. Therefore, Heiselberg (1994) conducted a full-scale experiment to estimate the rate of decrement of U_{max} according to the distance from the foot of the vertical surface [16].

The full-scale experiment was performed within an empty room with dimensions 7 x 6 x 3 m^3 (W x L x H) which was placed in a conditioned laboratory hall with a constant air temperature of 25 °C. One wall of the room was covered with 18 water-cooled panel radiators to resemble the cold vertical surface. The surface temperature of the vertical surface was 10–16 °C and the air temperature of the room was between 18-20 °C. The heat was supplied through the walls and ceiling due to transmission because of the temperature difference between the room and the laboratory hall (i.e. creates balance with the cold vertical surface). The measurements were performed between 0.01 and 0.5 m above the floor and 0.2 to 6.0 m from the vertical surface. Furthermore, no mechanical ventilation or heat sources were present and steady-state flow and temperature conditions were maintained throughout the experiment.

Heiselberg concluded that the flow field induced from the cold vertical surface can be divided into three zones (see Fig. 2.4):

- The zone close to the vertical surface in which the flow transitions from a vertical to a horizontal direction. The flow decreases linearly according to the characteristic height δ defined by Heiselberg as the height above the floor where the velocity has decreased to $\frac{1}{2}U_{max}$ [16];
- The zone in which entrainment occurs from the surrounding air into the colder flow;
- The zone in which (almost) no entrainment occurs and therefore the velocity and height of the flow region remain constant (i.e. stratified flow).

The above-mentioned observations made through the experiments performed by Heiselberg were implemented in the initial formulae of Eckert and Jackson (see Eq. (2.2)). Instead of calculating U_{max} at the foot of the cold vertical surface, Heiselberg derived empirical formulae to calculate U_{max} in the occupied zone at certain distances from the facade (2.3a-2.3c). In the occupied zone, the influence of U_{max} on thermal comfort is considered to be of importance compared to at the foot of the vertical surface.

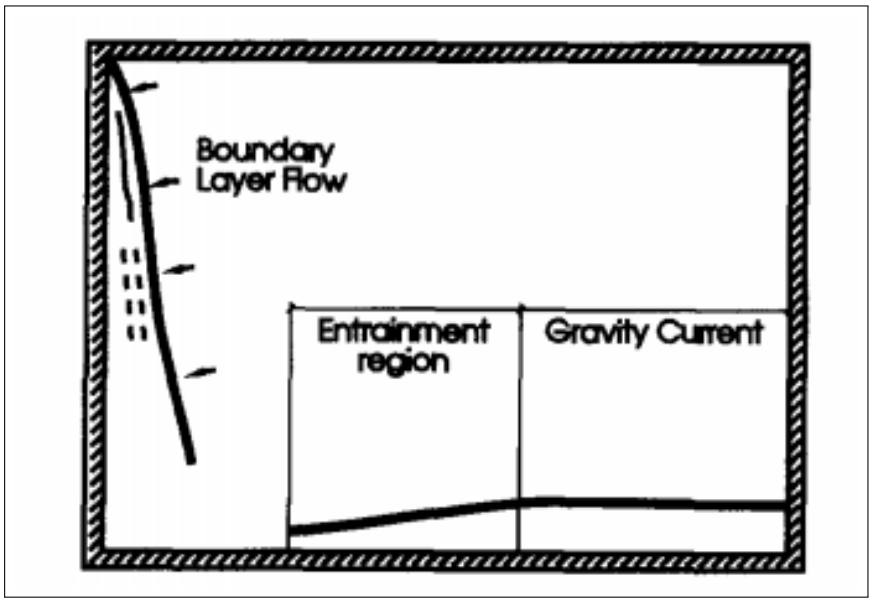

Figure 2.4: Flow development on the floor induced from the cold vertical surface [16]

$$U_{max}(x) = 0.055 \cdot \sqrt{\Delta\theta \cdot H} \qquad x < 0.4\ m \tag{2.3a}$$

$$U_{max}(x) = 0.095 \cdot \frac{\sqrt{\Delta\theta \cdot H}}{x + 1.32} \qquad 0.4 \leq x \leq 2.0\ m \tag{2.3b}$$

$$U_{max}(x) = 0.028 \cdot \sqrt{\Delta\theta \cdot H} \qquad x > 2.0\ m \tag{2.3c}$$

In contrary to Heiselberg, Manz and Frank [7] performed multiple numerical simulations to investigate the influence of internal heat sources and obstacles on the reliability of the empirical formulae. Manz and Frank concluded that the momentum of the buoyancy flows from internal heat sources increase U_{max} near the floor region. This results in the fact that the equations based on the experiment performed in an empty room by Heiselberg tends to underestimate U_{max} in realistic situations. Therefore, the empirical formulae of Heiselberg were corrected with a factor of 1.5 as described in Eqs. (2.4a-2.4c):

$$U_{max}(x) = 0.083\sqrt{\Delta\theta \cdot H} \qquad x < 0.4\ m \tag{2.4a}$$

$$U_{max}(x) = 0.143\frac{\sqrt{\Delta\theta \cdot H}}{x + 1.32} \qquad 0.4 \leq x \leq 2.0\ m \tag{2.4b}$$

$$U_{max}(x) = 0.043\sqrt{\Delta\theta \cdot H} \qquad x > 2.0\ m \tag{2.4c}$$

The corrected empirical formulae provide an upper band estimate for U_{max} within the occupied zone which takes into account typical internal heat gains for office rooms. Therefore, it could overestimate U_{max} in other building configurations.

Although the above-mentioned formulae are still used within practice, the experimental and numerical studies performed to derive them show several limitations [6]. The studies were performed in en empty room, the transparent facade elements were between 2 and 3 m in height, and no counteracting devices such as heating or ventilation were present. Therefore, the use of these formulae in office environments remains questionable. Also, the formulae provide no information regarding the spatial distribution and present only maximum values [7].

2.5 Additional research

In addition to the above-mentioned empirical formulae which assess downdraught multiple findings in the literature are summarized which describe the effect of obstacles on the experienced downdraught on the facade. This will contribute to the overall understanding of downdraught on the facade and in the near floor region.

Heiselberg [20] conducted an experimental study to investigate the effect of a structural system on the inside of large facades (i.e horizontal steel beams) on the boundary-layer flow to reduce downdraught and increase thermal comfort in the occupied zone. The steel beams in the structural system of the facade act as obstacles on the boundary-layer flow which results in different flow conditions (see Fig. 2.5).

The width of the obstacles has a large influence on the flow conditions occurring in the boundary-layer flow. Multiple experiments were conducted in which the Grashof number and different sizes of obstacles were used to find the critical width (w_{cr}) in which an intermediate flow pattern occurred. The Grashof number is a dimensionless number that describes the ratio between buoyancy and viscous forces acting on a fluid [14]. The intermediate flow pattern is characterized as unsteady in which both separation and recirculation are not completely observed (see Fig. 2.5). Once the obstacle width was smaller than w_{cr} the boundary-layer flow reattached to the vertical surface decreasing the velocity to some extent. Once the obstacle width was larger than w_{cr} the boundary-layer flow separated from the vertical surface and underneath the obstacle a new boundary-layer flow was generated. The separated flow penetrates further into the occupied zone. However, the reestablished boundary layer flow underneath the lowest obstacle on the facade determines the velocities in which the downdraught penetrates the occupied zone in the near floor region (see Fig. 2.5).

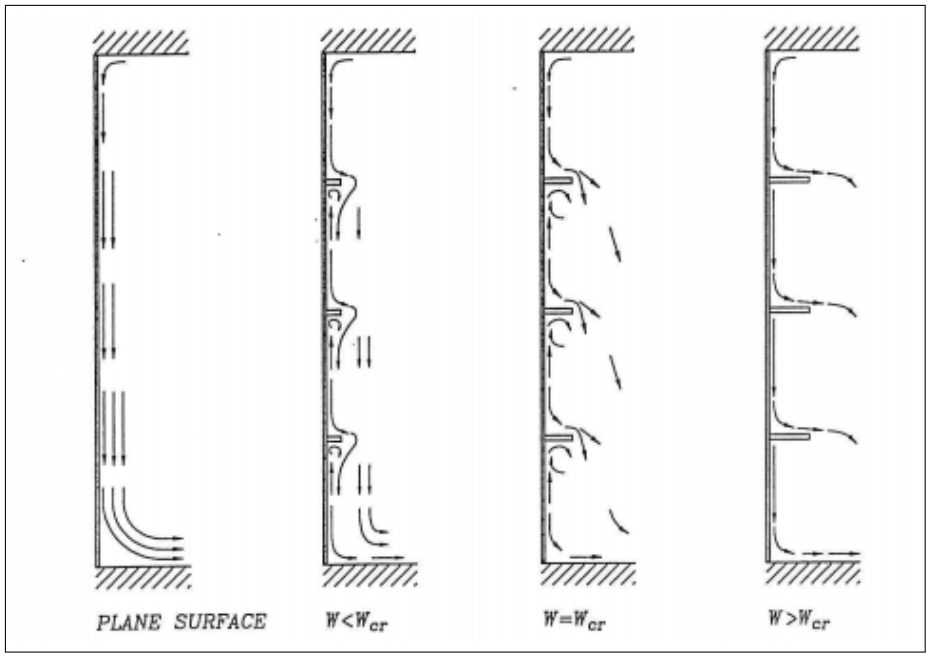

Figure 2.5: Flow characteristics induced from a cold vertical wall with different sized obstacles [20]

The height of the recirculation zone formed directly under the obstacle depends on the Grashof number and width of the obstacle. The separation of the boundary-layer flow and formation of the recirculation zone depend strongly on turbulent flow conditions (i.e. high Grashof numbers) [20]. The probability of turbulent flow conditions was increased if the distance between the obstacles were equal to or larger than 2 m in height. Heiselberg [20] concluded that a reduction in maximum velocity and temperature difference in the flow (i.e. between 10 and 40%) was achieved as the height of the recirculation zone increased.

Larsson and Moshfegh [3] investigated the effect of the thermal performance of transparent facade elements and the width of the window bay on the downdraught on the facade. Two windows were compared: a conventional window (U-factor = 1.8 W/m^2·K) and a well-insulated window (U-factor = 1.0 W/m^2·K). Furthermore, nine different window bay widths were examined [3].

In Figure 2.6 the flow characteristics under influence of the width of the window bay are shown. The downdraught on the facade created a recirculation cell in the corner of the window which increased with the width of the window bay. The increased cell affects the downdraught as it deflects the flow away from the wall underneath the window. However, if the deflection has not enough strength (i.e. loss of momentum due to the small width of window bay) the boundary-layer flow will reattach to the wall under the influence of the Coanda-effect. The effect decreases with an increased width of the window bay and nearly disappears once the width is larger than 70 to 90 mm [3].

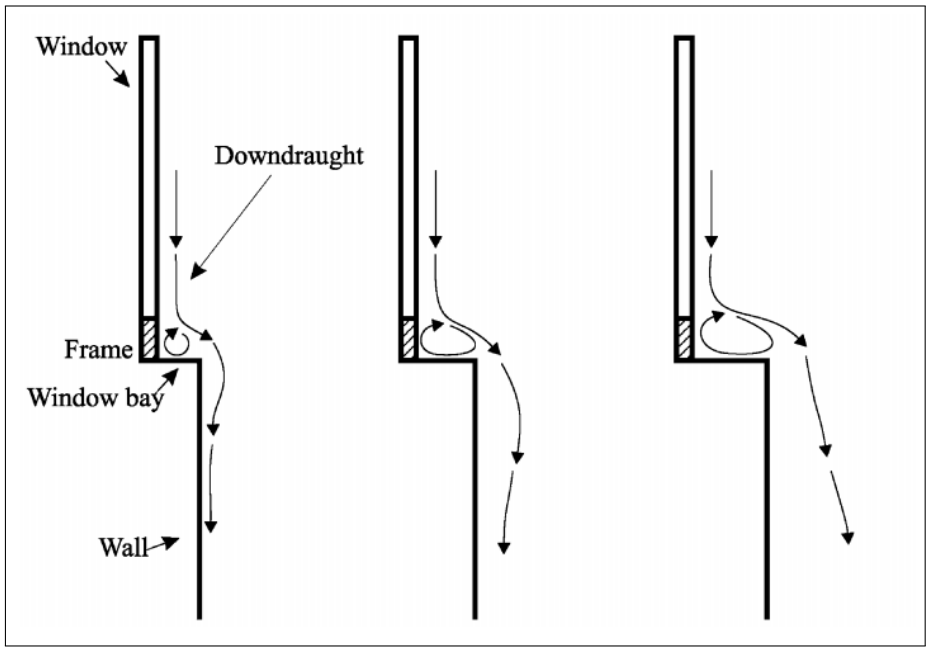

Figure 2.6: Principle of flow characteristics induced from a window with different widths of the window bay [3]

Larsson and Moshfegh [3] concluded that downdraught can be reduced by increasing the thermal performance of the windows. The maximum velocity and temperature difference in the flow was reduced increasing thermal comfort in the occupied zone. Furthermore, it was found that the influence of the window frame on downdraught is negligible compared to the window.

Ge and Fazio [21] investigated the characteristics of downdraught experienced under the influence of different windows in a metal curtain wall. Two windows were compared: a conventional window (U-factor = 2.76 W/m^2·K) and an insulated window (U-factor = 1.53 W/m^2·K). The horizontal profile of the metal curtain wall provides an obstacle that was similar to the window bay as discussed by Larsson and Moshfegh [3].

The resemblance between the horizontal profile and window bay resulted in similar flow characteristics near the obstacle. The obstacle reduced the momentum of the downdraught and deflected the flow away from the wall. The flow mixed with the surrounding air and resulted in a reduced velocity and increased temperature as it penetrates the occupied zone. Therefore, increased thermal performance of the window (i.e. well-insulated) resulted in better comfort conditions within the occupied zone [21].

Conclusion

The physical characteristics of natural convection (i.e. velocity and temperature distribution) indicate the importance of the near-wall region to be accurately solved in the numerical simulations. Therefore, in the generation of the computational grid extensive attention was given to that aspect of the numerical setup.

In addition to the empirical formulae of Heiselberg used in the LTC tool to evaluate U_{max} in the near floor region, the formulae of Manz and Frank were added in the analysis performed in this research. The implementation of these formulae could enhance the use of the LTC tool as it provides insight in the estimation of U_{max} under influence of heat sources typical for offices.

The use of obstacles in the region near the facade (i.e. window bay and horizontal structural elements) were not implemented in the generic office model to ensure the results can be interpreted over a wide range of office configurations.

3 — Generic office

3.1 General information

As mentioned in Section 2.3, RHDHV uses its LTC tool to assess whether the transition from high-temperature to low-temperature heating decreases the thermal comfort in the building configuration. An extensive part of the assignments related to this transition is focused on the thermal comfort within office buildings. Office buildings have on short-term a large retrofitting assignment to acquire a minimum energy label C classification required by the Dutch government per January 2023 [22]. The energy label indicates the energy efficiency of the building based on the annual primary fossil energy use expressed in kWh/(m^2·yr) [22].

An overview was made to quantify the retrofitting assignment for office buildings in the Netherlands based on their current energy label and building period (see Fig. 3.1). The differentiation between the building periods was specified according to the thermal performance of the building elements according to the NTA8800 [23]. In Figure 3.1 the relationship between the building period and number of office buildings that do not meet the minimum requirement of energy label C is displayed. Due to development in the thermal performance of building elements, efficiencies of installations, and improved regulations it can be noticed that an increase of office building with an energy label C or higher occurred over the last decades.

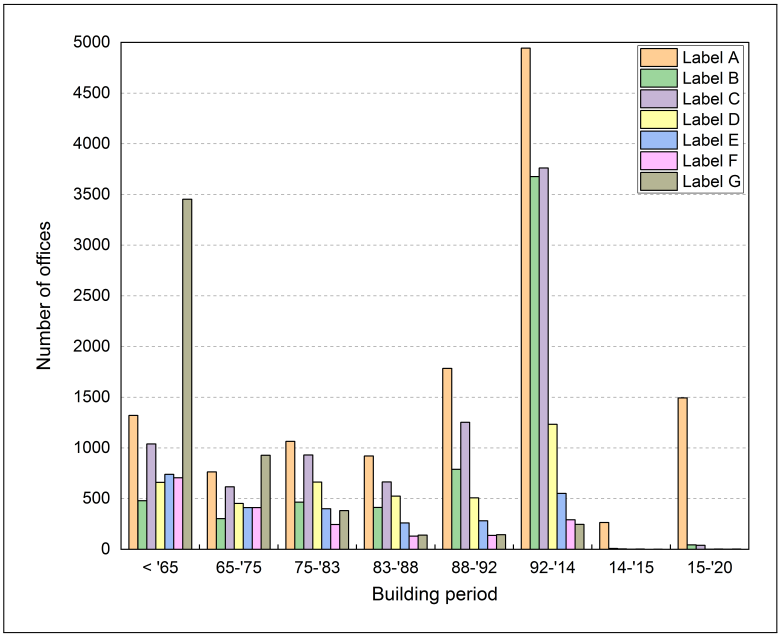

Figure 3.1: Overview of office buildings according to their energy label and building period [22]

To succeed in reducing the annual primary fossil energy use and reaching the required label C classification, multiple retrofitting methods can be distinguished. Firstly, the energy efficiency of the heating system can be increased in transitioning from high-temperature to low-temperature systems. Secondly, the thermal performance of the transparent and opaque building elements can be increased to decrease the transmission losses. Furthermore, a solution which is not considered within the research is to implement renewable energy sources . Nevertheless, the thermal comfort within the building should always be monitored in the process of retrofitting with care.

The effects of the required transition on thermal comfort were evaluated with the use of numerical simulations. The simulations are performed in a generic model which represents an office building with characteristics from the building period 1988 to 1992. The specific building period was chosen due to the intermediate thermal performance of the building elements in combination with the number of offices with an label D classification or lower. Although previous building periods have similar characteristics with moderate thermal characteristics, the chosen building period of 1998 to 1992 provides a representative situation in which the question can be answered whether improving the installation concept (i.e. HTH to LTH) would lead to an increase or similar conditions in thermal comfort compared to the initial building configuration or if it has to be combined with an increase in the thermal performance of the building elements. Depending on the specified answer to that question, similar measures can be implemented in older building configurations without a decrease in thermal comfort in the energy transition.

3.2 Building characteristics

The generic office model is made to provide results that can be interpreted over a wider range of office buildings which deviate to some extent from the generic characteristics. Therefore, an empty room with no furniture and heat sources (i.e. occupants, lighting, and other electrical devices) is considered as the results are then not restricted to one particular configuration. As mentioned in Section 2.4, an occupied room including internal heat sources does have an effect on the indoor conditions within the room (i.e. flow obstruction and flow acceleration due to thermal plumes). However, in the subsequent research the preference was on characterizing a generic office model. The building characteristics chosen for the generic office model represent the situation of an office in the building period 1988 to 1992.

The geometry of the generic model is established through the multiplication of a standardized grid size (= 1.8 m) and resulted in an rectangular enclosure with dimensions 3.6 x 5.4 x 2.7 m^3 (W x L x H) (see Fig. 3.2). The height of the enclosure deviates from the standardized grid size and is chosen to correspond to the validation study performed in Subsection 4.2.

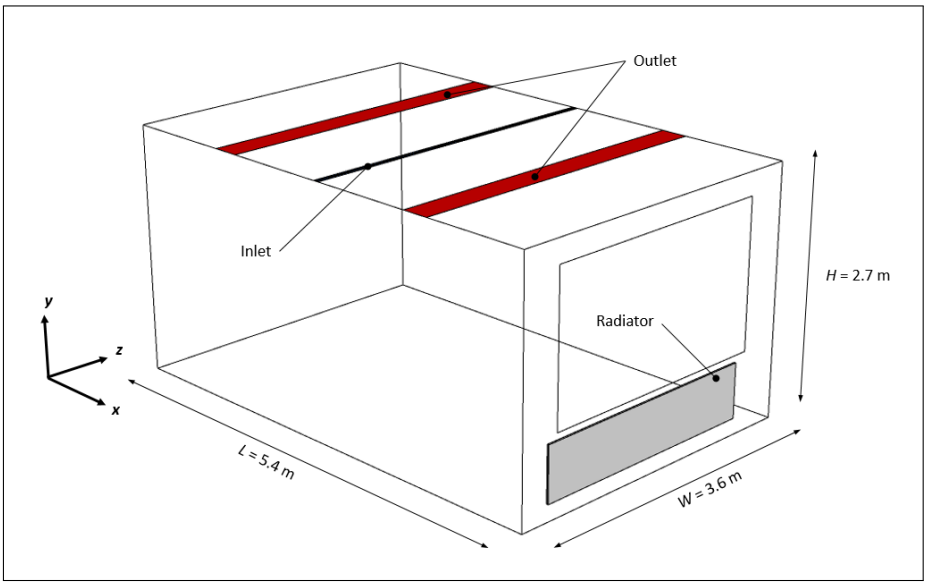

Figure 3.2: 3D generic office model geometry

The facades within the specific building period are often characterized as having a modular pattern in which repetitive windows are realized creating a neutral appearance (see Fig. 3.3) [24]. One window is placed in the model with dimensions 2.7 x 1.5 m^2 (W x H) to preserve the characteristic facade (see Fig. 3.2). The window is placed 0.95 m above the floor to ensure enough space is available for the radiator in a standardized setup. Furthermore, the window is placed 0.45 m away from both internal walls.

Figure 3.3: The characteristic facade design of two reference office buildings [24]

The ventilation air is supplied into the model through a centralized linear slot diffuser placed parallel to the facade. The linear slot diffuser is equipped with two slots that supply the air under an angle of 45 °. The two slots are placed along the entire width of the ceiling with the dimensions 0.024 x 3.6 m^2 (W x L) (see Fig. 3.4a-b). The flow is deviated under the desired angle due to the presence of a mechanism (i.e. valve) in the linear slot diffuser (see Fig. 3.5b). The valve in the diffuser reduces the inlet surface area (A) with approximately 55 % which results in an effective inlet surface area (A_i) of 0.06 m^2. The imposed inflow velocity is therefore calculated with the effective inlet surface area (A_i) and under the assumption that three persons are present in the office building which require fresh air with a flow rate (Q) of 35 m^3/h per person (i.e. 105 m^3/h or 0.03 m^3/s). Furthermore, the fresh air supplied to the model is preconditioned to a temperature of 18 °C.

The energy is provided into the enclosure by a traditional high-temperature radiator system placed underneath the window. High temperature is characterized as the supply and return temperature T_s and T_r of the system are heated up to 80 and 60 °C, respectively. An energy balance is performed to define the dimensions and the type of radiator (see Appendix A). The energy balance was conducted under the assumption of winter condition which are typical for the Netherlands with an outdoor temperature T_e of -5 °C. A type 10 radiator with one panel and no convectors is used with dimension 0.02 x 2.7 x 0.6 m^3 (W x L x H) [25]. The length of the radiator is equally wide as the window to compensate for downdraught on the facade. The radiator is placed in a standardized setup of 0.1 m above the floor and at a distance of 0.1 m fromthe facade (see Fig. 3.4a and c).

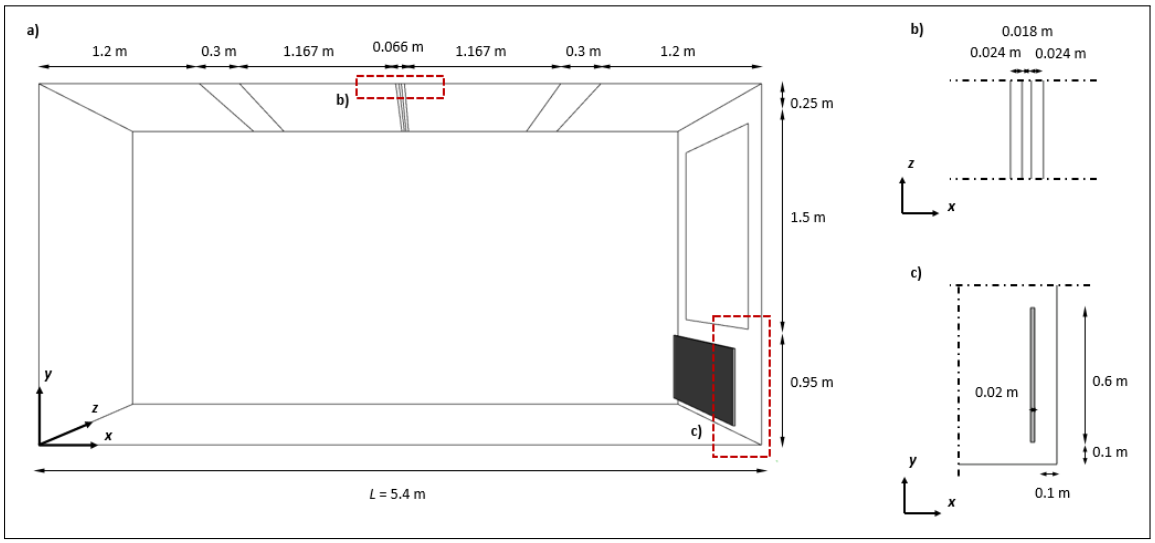

Figure 3.4: (a) 2D computational geometry. (b-c) Close-up view of geometry: (b) ventilation inlet; (c) radiator

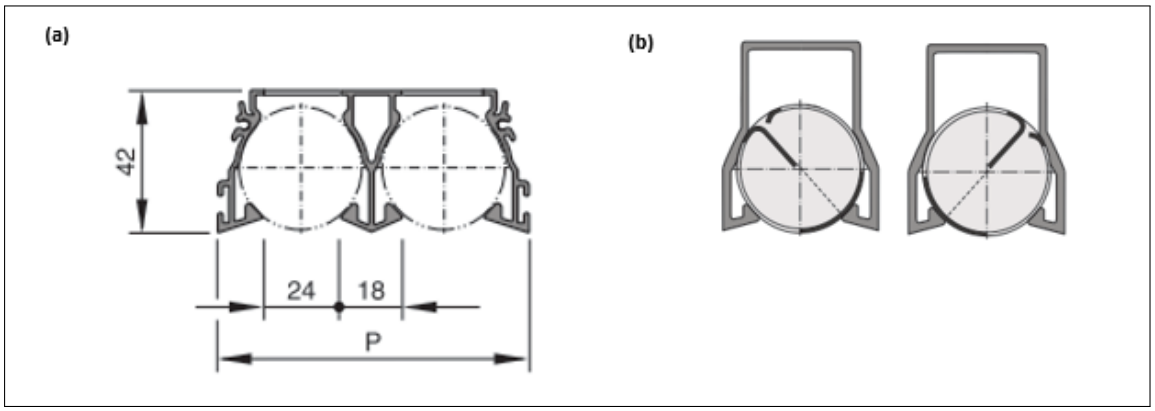

Figure 3.5: (a) 2D geometry of centralized linear slot diffuser: (b) reduced inlet area under an angle of 45° [26]

Heat loss within the generic office model is considered in two ways, namely an adiabatic relation between the internal building structures (i.e. floor, walls, and ceiling) as similar conditions in adjacent enclosures were assumed and heat transmission through the transparent and opaque facade elements. The adiabatic relation results in an heat flux of zero as no heat transfer occurs between the adjacent enclosures and the office model. The heat transmission is estimated based on representative values for the thermal performance of the transparent and opaque facade elements that provide an average from examples used within practice in the specific building period (i.e. forfaitair) [23]. The heat transmittance of the transparent facade element is a combined value for a structure of double glass in a metal frame that is not thermally interrupted and has a U-factor of 4.1 W/m^2·K. The thermal resistance of the opaque facade element has a R_c-value of 2.0 m^2·K/W.

Furthermore, in the model, no infiltration is considered due to its difficult nature to implement in steady-state simulation. The position and magnitude of infiltration on the facade are difficult to estimate and model in CFD because they differentiate according to the type of building envelope, the degradation of the building envelope, and under meteorological parameters (i.e. wind speed and direction) [27].

3.3 Transition scenarios

The model described in the previous section resembles the initial scenario which characterizes an office in the specified building period. However, the focus of the research is to investigate whether the thermal comfort decreases in the transition from HTH to LTH within an office environment under multiple conditions. Multiple scenarios for heating systems are designed to emphasize the different methods to achieve a system that uses LTH within an office (see Fig. 3.6).

In the design of the transition scenarios, extensive attention was paid to two key factors. The expertise of RHDHV was used to formulate common low-temperature systems which they applied in reference projects and the related investment costs for the stakeholder. Two approaches were distinguished to transition from a traditional high-temperature system to a low-temperature system. Firstly, approach 1 in which the existing radiator was radically replaced by a climate ceiling and requires the largest investment. However, it improves the use of floor space as the radiator is removed and the occupied zone can be extended towards the facade. It is therefore considered as a desired alternative for the stakeholder. Secondly, approach 2 in which the existing radiator was preserved, however, the capacity of the radiator decreased and a combination with another system was needed. Approach 2 can be considered as a more step-wise transition in which the capacity of the existing radiator can be lowered to MTH or LTH depending on the desire of the stakeholder in terms of retrofitting vision and investment. The characteristics of each transition scenario are briefly summarized below:

In Scenario 1 (see Fig. 3.6a), the initial scenario of the generic office model is displayed using the characteristics mentioned in Section 3.2.

In Scenario 2 (see Fig. 3.6b), the radiator is completely removed and replaced by a LTH climate ceiling system ($T_s = 35$ °C and $T_r = 30$ °C).

In Scenario 3 (see Fig. 3.6c), the capacity of the radiator was decreased by switching to MTH (i.e. $T_s = 50$ °C and $T_r = 40$ °C). The loss of capacity was compensated for by applying a climate ceiling (i.e. LTH).

In Scenario 4 (see Fig. 3.6d), the capacity of the radiator was decreased even further by switching to LTH (i.e. $T_s = 35$ °C and $T_r = 30$ °C). The loss of capacity was compensated for by applying a climate ceiling (i.e. LTH).

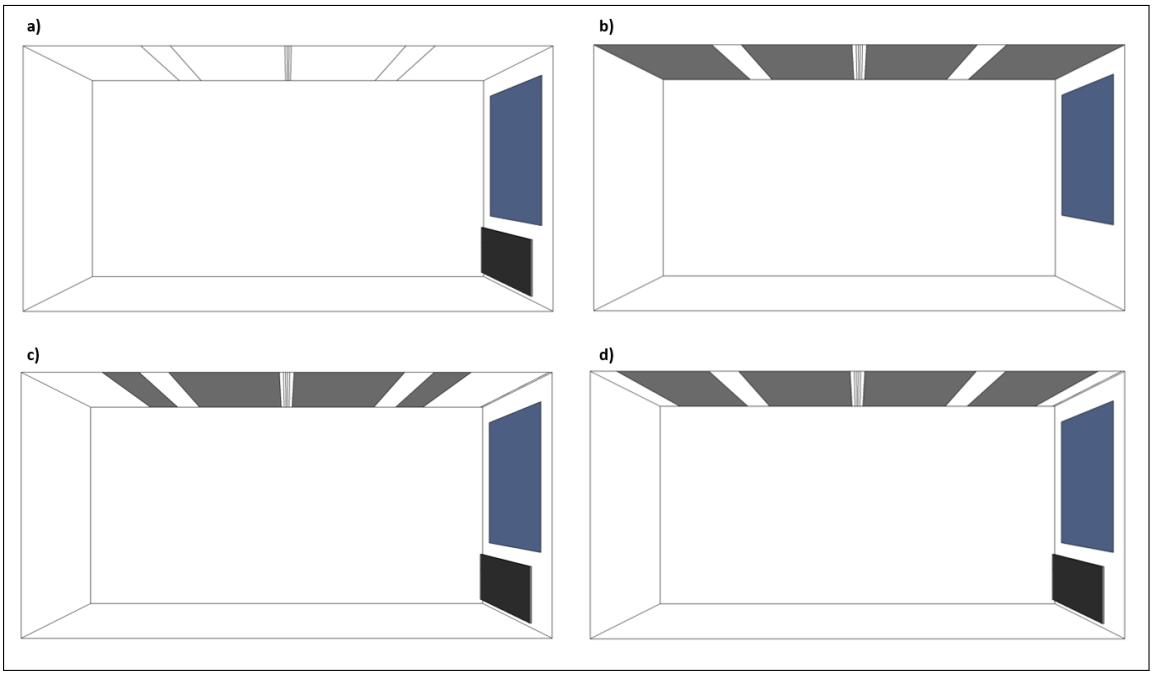

Figure 3.6: (a) Scenario 1: existing radiator (HTH). (b) Scenario 2: climate ceiling. (c) Scenario 3: radiator (MTH) + climate ceiling. (d) Scenario 4: radiator (LTH) + climate ceiling

4 — Validation

The reliability and accuracy of the CFD simulations for the generic office model have been assessed through an extensive validation study. The validation study is twofold and focuses on basic indoor airflow structures under multiple conditions: a 2D isothermal case of Nielsen [9] and a 3D non-isothermal case of Li et al. [10]. The computational settings and parameters that come from these validation studies are used in the subsequent case study.

4.1 Two-dimensional isothermal benchmark test (IEA)

The International Energy Agency (IEA) Annex 20 project "Air flow patterns within buildings" was launched in May 1988 to evaluate the performance of CFD as a design tool for single- and multi-zone air and contaminant flows [28]. Annex 20 provides experimental benchmark data obtained from 2D and multiple 3D experiments under both isothermal and non-isothermal conditions for basic flow phenomena (e.g. jet flow and convection) [28]. The experimental data was eventually used to compare and evaluate complex and simplified CFD codes to accurately predict air movement and temperature distribution.

The 2D benchmark case was conducted by Nielsen [29] to gain insight into the streamline pattern, vertical velocity and turbulence profile, and temperature distribution within simple enclosures with different geometries. Therefore, by performing a validation study on the benchmark case of Nielsen a general understanding of the accuracy of CFD simulations for indoor airflow is achieved. The case study *2D1* was chosen to validate the indoor airflow under isothermal conditions.

The experiment was performed in a small-scale wooden-frame box-like enclosure with dimension 0.6 x 1.8 x 0.6 (W x L x H) [29]. To visualize the streamline pattern, the sidewalls and ceiling were made of transparent material and illuminated through a light-box. The air was supplied through a nozzle that ends in a supply opening placed at the top of the model with a height of 7.2 mm. The supply opening was located along the entire width of the enclosure and was divided into five sections to examine the flow pattern in fully or partially opened inlet conditions. The air was extracted through blowers which were placed behind an outlet opening. An extra transparent floor and wall section was placed in the model to vary in length and height between multiple measurements. The velocity profile was measured with an anemometer and thermocouples were used to measure the temperature distribution [29].

Nielsen used a small-scale modeling technique which was considered to be advantageous compared to full-scale due to the use of smaller dimensions and systems, and the experiments are more flexible to investigate multiple geometries [29]. However, as small-scale modeling represents a full-scale situation it is important to achieve similitude between multiple parameters (i.e. pressure, temperature, and velocity) and ensure equal conditions are achieved. Through the examination of the dimensionless number of Reynolds (Re), Archimedes (Ar), and Prandtl (Pr) Nielsen concluded that similitude was achieved [29]. Therefore, the full-scale geometry was used in the validation study as reported in multiple publications of Nielsen [29] [9] [30].

4.1.1 Computational geometry

The 2D computational geometry used for the validation study was reproduced from the experimental setup of Nielsen [9]. The setup consist of a rectangular enclosure with the dimensions 9 m x 3 m (L x H) and an inlet height (h) and outlet height (t) of 0.168 m and 0.48 m, respectively (see Fig. 4.1). The computational geometry was simplified compared to the experimental setup by not including the extended section of the inlet (upstream) and outlet (downstream).

Two vertical measurement lines were defined at x = H and x = $2H$ along which the experimental and numerical data were compared.

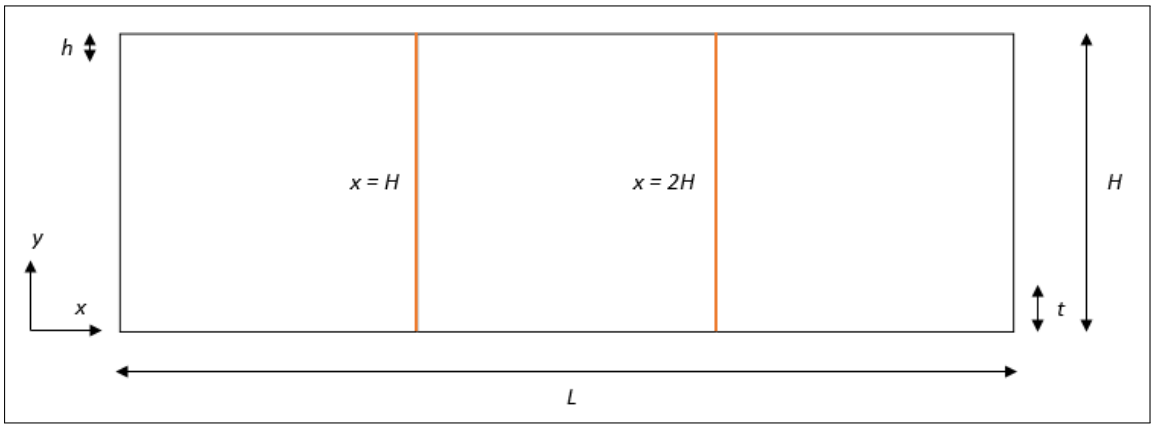

Figure 4.1: Computational geometry reproduced from the experimental setup of Nielsen [9].

4.1.2 Computational grid

To generate a grid-independent solution, three consecutive grids were built by applying a systematic refinement of the coarse grid by a factor of $\sqrt{2}$ in each direction. The constructed coarse, basic and fine grids contain 5,696 cells, 11,648 cells and 23,790 cells, respectively (see Fig. 4.2). The computational grids consist of hexahedral cells only.

Mean air velocities within most indoor environments are relatively low (i.e. ≤ 0.2 m/s) and can be characterized as low-Reynolds number flows [31]. The Reynolds number (Re) expresses the ratio between the inertial and viscous forces within a fluid. Theoretically, a low-Reynolds number flow indicates that viscous forces are more dominant, thereby reduce the motion, and create a laminar flow structure. However, in an indoor environment multiple flow structures can be distinguished (i.e. laminar, transitional, and turbulent). Therefore, the flow structure is considered to be quite complex and foremost not strictly laminar in the case of low Reynolds numbers [31].

To accurately predict the temperature and velocity distribution in the boundary layer it is important to solve the viscous sublayer in which viscous forces are dominant (see Subsection 2.3). To resolve the viscous sublayer, the dimensionless wall distance (y^*) needs to be controlled to enable low-Reynolds number modeling (LRNM) [32]. y^* is a non-dimensional wall distance based on the ratio between the product of the friction velocity (u_*) and distance (y) divided by the kinematic viscosity (ν). To enable LRNM, a recommended value for $y^* < 5$ should be maintained.

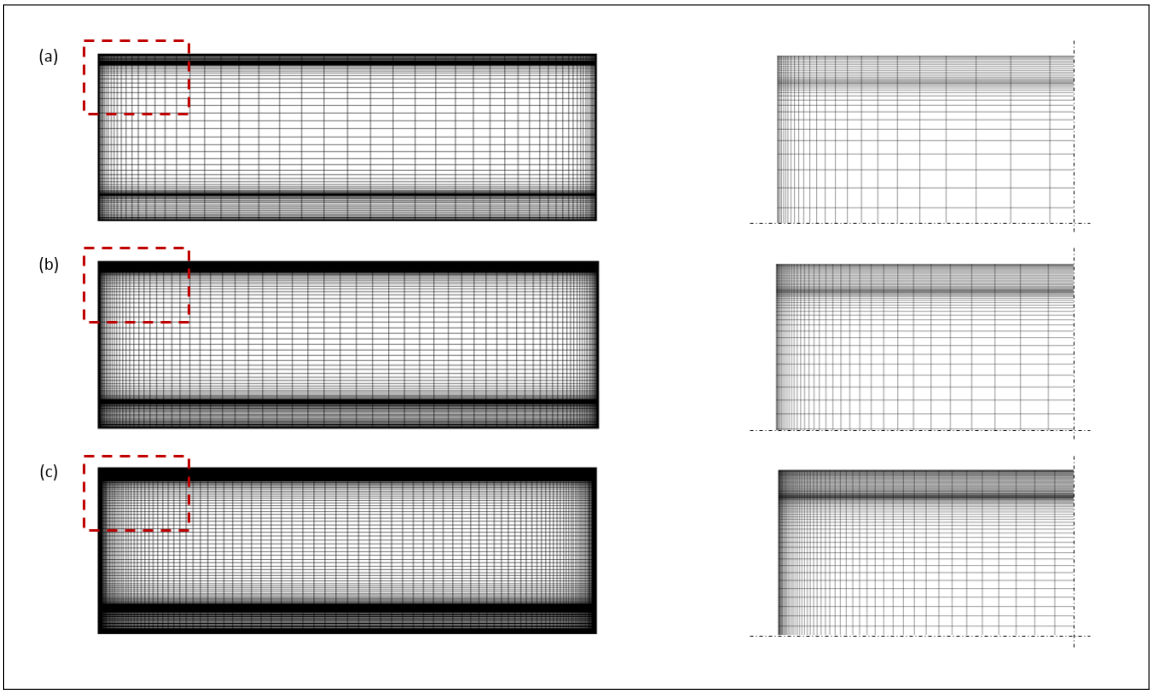

Figure 4.2: Computational grids (a) coarse = 5,696 cells, (b) basic = 11,648 cells, and (c) fine = 23,790 cells.

The y^* values were measured along the ceiling which represented the region of expected highest velocity due to the formation of the boundary layer flow from the inlet. The maximum y^* values on the ceiling are 21.1, 7.3, and 6.1 for the coarse, basic, and fine grid, respectively. The average y^* values on the ceiling are 12.0, 3.4, and 2.5 for the coarse, basic, and fine grid, respectively.

The three computational grids exceed locally the recommended value of $y^* < 5$ on the ceiling. However, the basic and fine grid have an average y^* value well below the recommended value. It is concluded that the basic and fine grid have a sufficient near-wall grid resolution to enable LRNM within the 2D isothermal benchmark test.

4.1.3 Boundary conditions

A uniform velocity, which was based on the Reynolds number of the experiment (i.e. $Re = 5000$), was imposed at the inlet of the computational model [9]. The inlet velocity was determined by using Eq. (4.1) with ν the kinematic viscosity ($= 15.3 \cdot 10^{-6}$ m^2/s at an air temperature of 20 °C), which resulted in a supply velocity of $U_0 = 0.455$ m/s.

$$Re = \frac{h \cdot U_0}{\nu} \tag{4.1}$$

The turbulent kinetic energy k was estimated at a value of $4.97 \cdot 10^{-4}$ m^2/s^2 using Eq. (4.2) in which the value of 0.04 represents the turbulence intensity I at the inlet of 4%. The turbulent dissipation rate ϵ was estimated at a value of $6.59 \cdot 10^{-4}$ m^2/s^3 using Eq. (4.3) in which $l_0 = h/10$ [9].

$$k = 1.5(0.04 \cdot U_0)^2 \tag{4.2}$$

$$\epsilon = k^{1.5}/l_0 \tag{4.3}$$

Furthermore, no-slip conditions were applied to the walls of the enclosure and zero static gauge pressure was applied at the pressure outlet.

4.1.4 Solver settings

The 2D steady Reynolds-averaged Navier-Stokes (RANS) equations were solved using the RNG k-ϵ turbulence model combined with the two-layer enhanced wall treatment (EWT) zonal model. To enable LRNM and resolve the flow down to the viscous sublayer within k-ϵ turbulence models, the EWT zonal model is required. The use of the turbulence model combined with EWT was chosen due to proven accuracy in previously conducted studies based on the experimental study of Nielsen [33] [34].

The SIMPLE algorithm was used for pressure-velocity coupling, pressure interpolation was of second-order, and the second-order discretization scheme was used for momentum, k and ϵ. The numerical simulations were performed using ANSYS Fluent 19.2 (2018).

Convergence of the scaled residuals was declared when they did not show any further reduction related to an increase in the number of iterations.

4.1.5 Grid-sensitivity analysis

The results presented in figures 4.3a and 4.3b show a large overlap between the basic and fine grid for both vertical lines in terms of dimensionless streamwise velocity U/U_0. Therefore, it is concluded that further refinement of the basic grid would not lead to more accurate results compared to the increase in computational costs.

The discretization error was quantified by using the uniform reporting method of Roache, also known as the grid-convergence index (GCI) [35]. The GCI was calculated between the basic and fine grid for the streamwise velocity U using Eq. (4.4)

$$GCI_{basic} = F_s \left| \frac{r^p \left[(U_{basic} - U_{fine}) / U_0 \right]}{1 - r^p} \right| \tag{4.4}$$

where F_s is a safety factor, taken as 1.25 due to the use of three consecutive grids, r is the linear refinement factor ($\sqrt{2}$) and p is the formal order of accuracy, taken as 2 for the use of second-order discretization schemes [35].

Figures 4.3c and 4.3d present the results for the estimated GCI. The average GCI along the two vertical lines of interest (x = H and x = $2H$) is estimated at 0.0027 and 0.0026, respectively. The results of the grid-sensitivity analysis show that the use of the basic computational grid was sufficient to proceed with the validation.

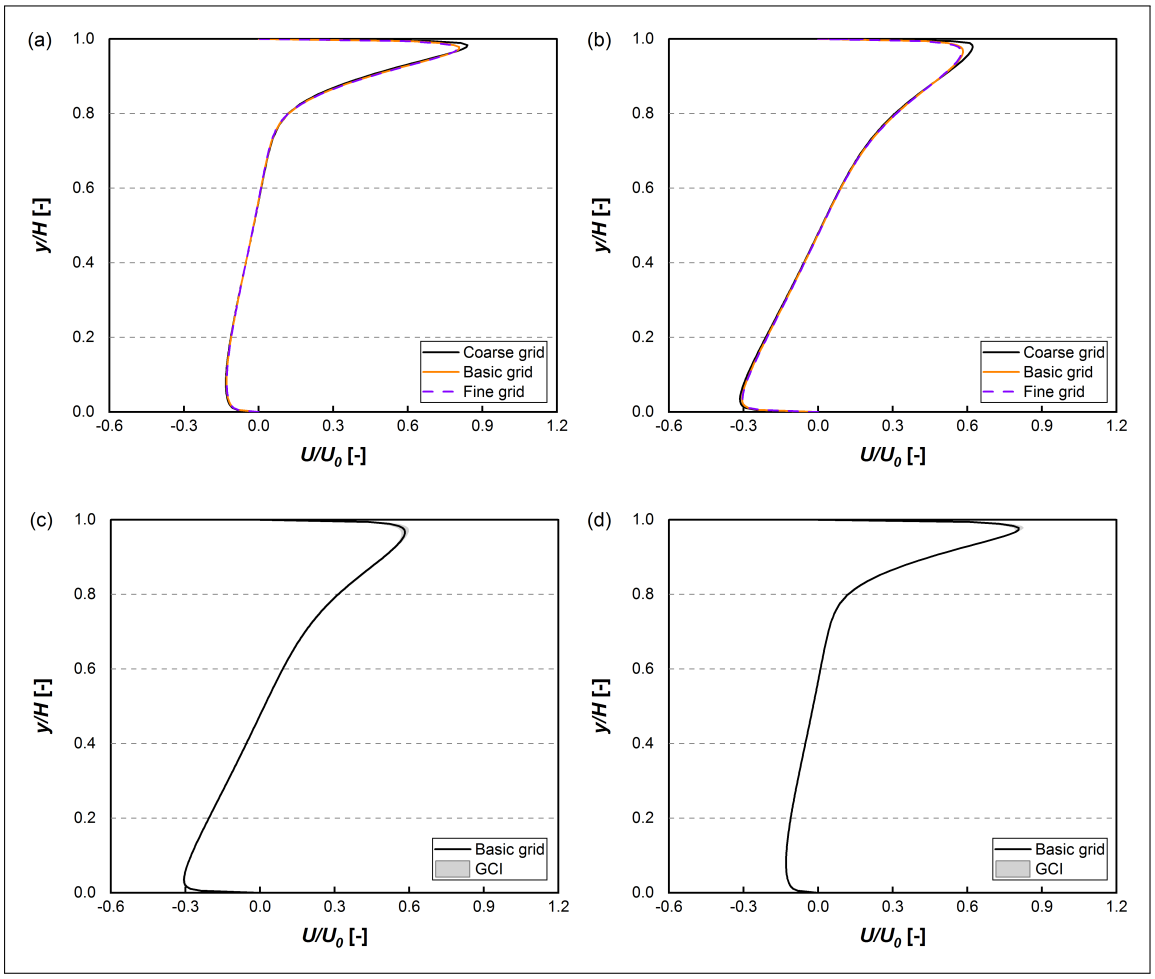

Figure 4.3: Results of grid-sensitivity analysis: U/U_0 at (a) x = H, (b) x = $2H$. GCI for basic grid at (c) x = H and (d) x = $2H$.

4.1.6 Results

As previously mentioned, in the rectangular enclosure two vertical lines were placed at x = H and x = $2H$. The experimental benchmark data obtained at those lines were used to validate the numerical results. Figure 4.4 shows the comparison along the two vertical reference lines for the dimensionless streamwise velocity U/U_0 and dimensionless turbulent kinetic energy $k^{0.5}/U_0$ between the experimental and numerical results.

Observing the results for U/U_0 and $k^{0.5}/U_0$, it can be stated that a good agreement was reached along the vertical reference lines for both parameters. The largest discrepancy occurred near the floor ($y/H < 0.2$) while the agreement was best for the upper region of the enclosure ($y/H > 0.8$). Due to the large velocity gradient near the ceiling caused by the boundary layer flow, the behavior of the flow regime in that particular region was considered as most important.

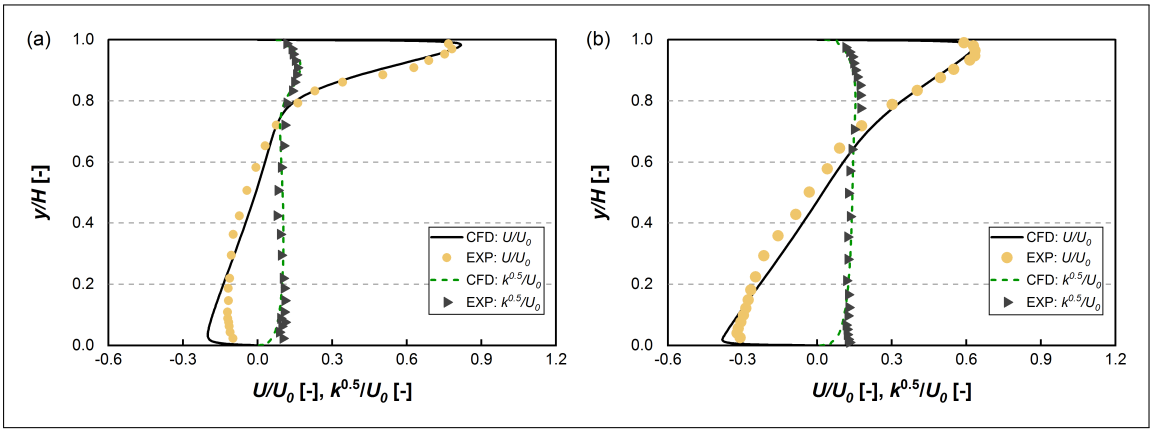

Figure 4.4: Validation assessment for U/U_0 and $k^{0.5}/U_0$: (a) x = H and (b) x = $2H$

Furthermore, two scatter plots are made (see Fig. 4.5) to indicate the error between the numerical and experimental results. The line of best fit, x = y, indicates a perfect agreement between both results. In Figure 4.5a the agreement of U/U_0 corresponds to a large extent with the conclusions made above. However, the error at some points in the upper region ($y/H > 0.8$) was between 10-20% with a few outliers above 30% for the line x = H. Although the near-wall mesh on the ceiling exceeds the threshold value to enable LRNM locally, the influence was considered to be negligible on the results as EWT guarantees also a reasonable velocity profile inside the buffer region (i.e. $3 < y^* < 10$) [32]. The differences in results could be caused due to the simplification of the computational geometry which could affect the results as the extended section of the inlet was not taken into account. Also, measurement errors and uncertainties could have occurred in obtaining the experimental benchmark data by Nielsen [9].

In Figure 4.5b, the difference of $k^{0.5}/U_0$ is for a large extend below 20% indicating a good agreement.

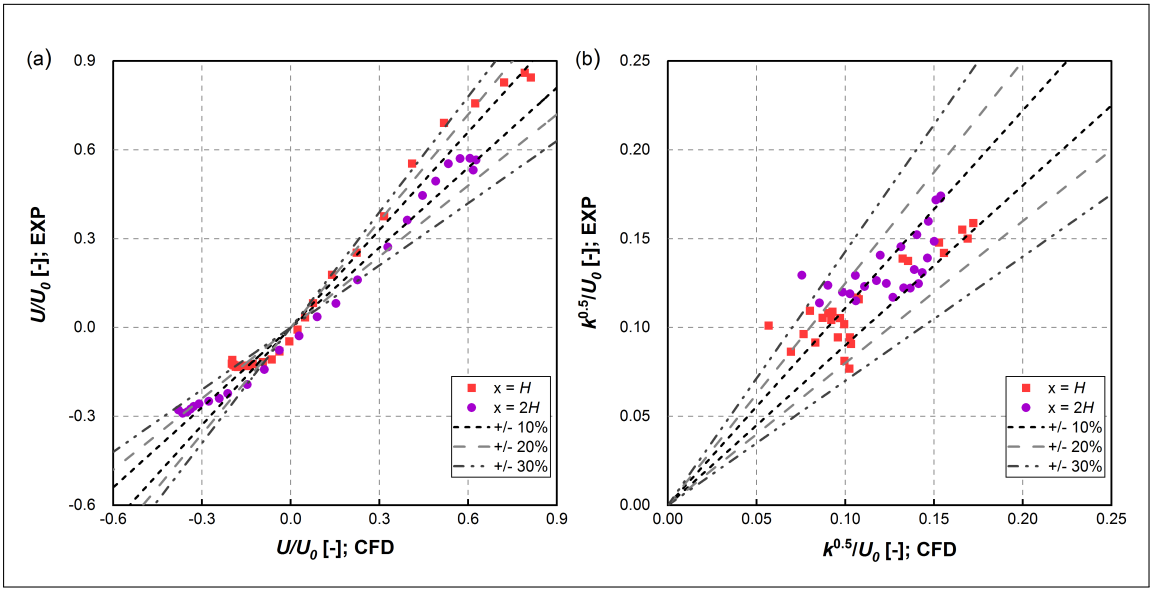

Figure 4.5: Comparison between numerical and experimental data: (a) U/U_0 and (b) $k^{0.5}/U_0$.

In addition to the scatter plots displayed in Figure 4.5, two validation metrics were calculated to quantitatively evaluate the performance of the numerical simulation. The validation metrics factor of 1.3 observations (FAC1.3) and factor of 2 observations (FAC2) were calculated using Eq. 4.5 and 4.6 [36]:

$$FAC1.3 = \frac{1}{n}\sum_{n=1}^{n} N_i \;\; with \;\; N_i = \begin{cases} 1 & for\ 0.77 \leq \frac{P_i}{O_i} \leq 1.3 \\ 0 & else \end{cases} \tag{4.5}$$

$$FAC2 = \frac{1}{n}\sum_{n=1}^{n} N_i \;\; with \;\; N_i = \begin{cases} 1 & for\ 0.5 \leq \frac{P_i}{O_i} \leq 2.0 \\ 0 & else \end{cases} \tag{4.6}$$

where O_i is the observed (experimental) value and P_i the predicted (numerical) value. The results shown in Table 4.1 display a very good agreement on the two validation metrics. It is concluded that the validation study using the RNG k-ϵ turbulence model accompanied with the specified boundary conditions and computational settings was sufficiently accurate in predicting both the dimensionless velocity U/U_0 and dimensionless turbulent kinetic energy $k^{0.5}/U_0$.

Table 4.1: Validation metric results for U/U_0 and $k^{0.5}$

	FAC1.3 (U/U_0)	**FAC2** (U/U_0)	**FAC1.3** ($k^{0.5}/U_0$)	**FAC2** ($k^{0.5}/U_0$)
Ideal value	**1**	**1**	**1**	**1**
x = H	0.76	0.92	0.76	1.00
x = $2H$	0.76	0.88	0.92	1.00

4.2 Three-dimensional non-isothermal study

In Section 4.1, the effects of isothermal conditions on the airflow were investigated. However, in a more realistic environment, non-isothermal conditions should be considered due to the presence of different heat sources. The purpose of the overall research is to investigate different heating systems and their effect on thermal comfort and the magnitude of downdraught within an enclosure. Although multiple studies were conducted providing experimental data on the subject, they were not considered to be suitable for use as a validation study due to a lack of information on the exact experimental setup [37] [38] [39]. Therefore, the non-isothermal validation study was eventually based on the data obtained from the full-scale experimental study of Li et al. [10]. The experimental study provides insight into radiative effects on the vertical temperature gradient and examines the gravity current experienced in a full-scale enclosure ventilated by displacement ventilation.

The experimental study was performed in a full-scale test room representing a typical office. The test room was placed within two different environments: a large enclosure that controlled the exterior surface temperature of three walls and a laboratory hall that controlled the conditions of the wall in which the inlet is situated and the ceiling [10]. A comprehensive analysis was performed in the test room as nine different cases (i.e. *B1* to *B5* and *A1* to *A4*) were tested based on differences in surface emissivity (ϵ), heat load (E), supply flow rate (n), and supply temperature (T_i). The interior wall surfaces were either covered with aluminum sheets (i.e. denoted by A) or painted black (i.e. denoted by B) indicating the difference in surface emissivity. The heat load was controlled through a cubical-shaped source in which 24 light bulbs of 25 W were placed and individually controlled to provide heat loads up to 600 W. Furthermore, multiple thermocouples were used to measure the air temperature along a vertical measurement pole, the interior and exterior surface temperatures, and the supply and outlet air temperatures. The measurement uncertainty throughout the experiment was estimated to be $\pm$ 0.1 °C [10].

The individual cases were extensively measured and monitored, however, Li et al. [10] reported the cases *B1*, *B2*, *B3*, and *A2* more completely compared to others [40]. The largest amount of information was provided for case *B1* and therefore it was decided to proceed with the validation study based on that particular case. Case *B1* has black painted interior surfaces, a heat load E of 300 W, a supply flow rate n of 1 h^{-1}, and a supply temperature T_i of 16.0 °C. As an addition to the experimental study, the numerical study of Gilani et al. [40] was used as it provides useful information on the possible implementation of the numerical setup.

4.2.1 Computational geometry

The full-scale experimental setup was reproduced to create a rectangular enclosure with dimensions 3.6 x 4.2 x 2.75 m^3 (W x L x H) [10]. The air was supplied into the enclosure through an inlet situated at floor level with dimensions 0.45 x 0.5 m^2 (W x H). Due to a perforation of 50%, the effective inlet surface area was reduced to 0.1125 m^2. The air was extracted from the enclosure through an outlet situated near the ceiling with dimensions 0.525 x 0.22 m^2 (W x H). A rectangular heat source with dimensions 0.3 x 0.4 x 0.3 m^3 (W x L x H) was placed 0.1 m above the floor and at 2.7 m from the inlet.

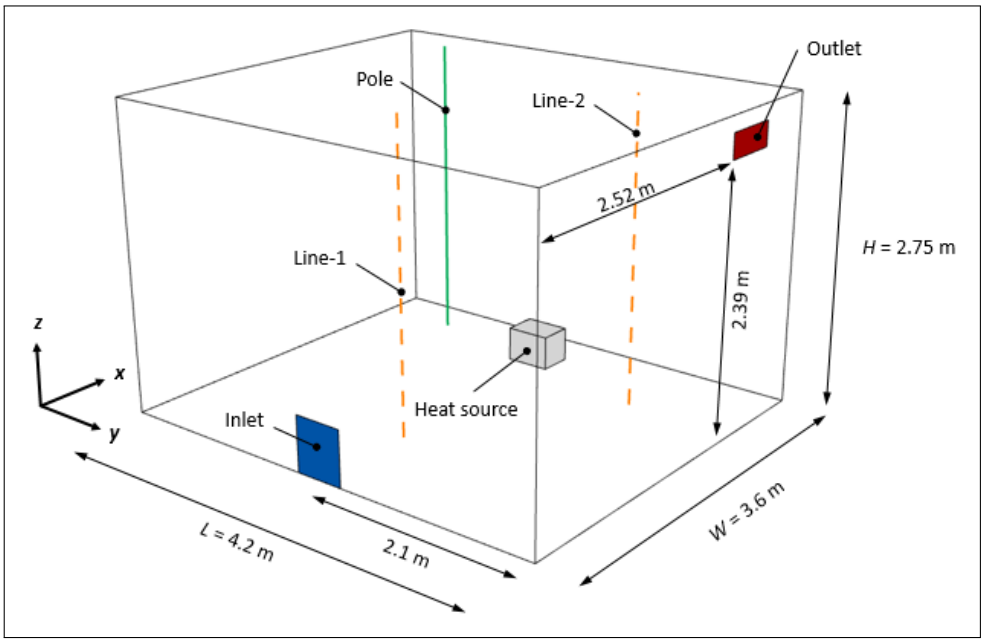

Figure 4.6: Computational geometry reproduced from experimental setup of Li et al. [10]

One vertical measurement pole and two vertical sampling lines were defined in the enclosure (see Fig. 4.6). The measurement pole was used in the experiment to measure the temperature profile from which the numerical results could be validated. The sampling line-1 and line-2 were defined to provide a more comprehensive grid-sensitivity analysis as an addition to the measurement pole as used in [10]. The XY coordinates for each vertical line were (3.2, 3.45), (1.0, 2.1), and (2.7, 1.0) for the pole, line-1, and line-2, respectively.

4.2.2 Computational grid

To generate a grid-independent solution, three consecutive grids were built by applying systematic refining and coarsening of the basic grid by a factor of $\sqrt{2}$ in each direction. The constructed coarse, basic and fine grids contain 522,340 cells, 1,397,363 cells, and 4,041,324 cells, respectively (see Fig 4.7). The computational grids consist of hexahedral cells only.

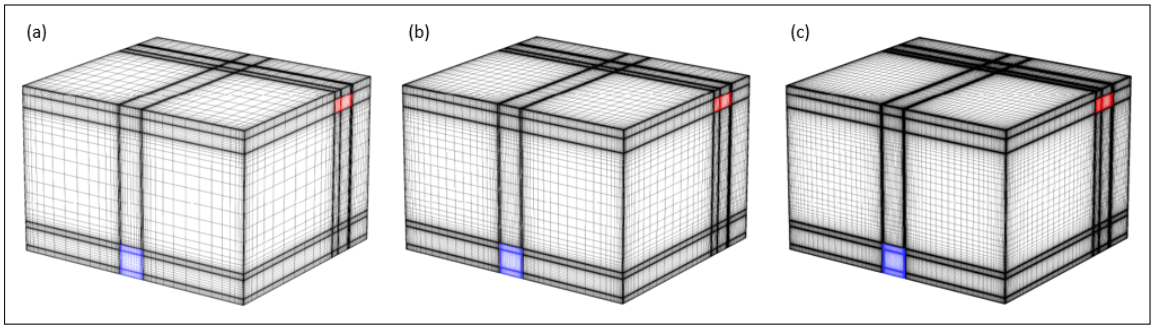

Figure 4.7: Computational grids (a) coarse = 522,340 cells, (b) basic = 1,397,363 cells and (c) fine = 4,041,324 cells.

The dimensionless wall distance y^* was measured in the regions of highest velocity, namely the upper part of the heat source due to buoyancy forces and the area of the ceiling above the source. To enable LRNM, the recommended value of $y^* < 5$ should not be exceeded (see 4.1.2).

The maximum y^* values on the ceiling are 8.56, 5.36, and 3.46 for the coarse, basic and fine grid, respectively. The average y^* on the ceiling are 3.43, 2.17, and 1.53 for the coarse, basic, and fine grid, respectively. The maximum y^* on the heat source are 8.64, 6.38, and 4.66 for the coarse, basic and fine grid, respectively. The average y^* on the heat source are 4.95, 3.37, and 2.41 for the coarse, basic and fine grid, respectively.

The coarse and basic grid exceed the recommended value of $y^* < 5$ locally on the ceiling and the edge of the heat source. However, all three computational grids have average y^* values well below the recommended value. It is concluded that the computational grids have a sufficient near-wall grid resolution to enable LRNM within the specified case.

4.2.3 Boundary conditions

As mentioned, the experimental data and setup of validation case *B1* was used as it provided the largest amount of data [40]. The assigned boundary conditions for case *B1* including additional conditions from the study of Gilani et al. [40] are discussed below.

The computational domain was divided into two separate zones, namely a fluid-type zone for the air inside the enclosure and a solid-type zone for the heat source. The individual zones were thermally coupled using a wall boundary condition on the interface between the fluid and solid zone. A source term was assigned to the solid heat source with a constant volumetric heat generation (q) of 8333 W/m^3, calculated using Eq. (4.7):

$$q = \frac{E}{V_{hs}} \tag{4.7}$$

where V_{hs} is the volume of the heat source (m^3) and E the heat load (= 300 W).

Furthermore, the density of the air (ρ) inside the enclosure was calculated as a function of temperature by applying the incompressible gas law. Other properties of air were set according to the default values in ANSYS Fluent 19.2 [32].

Inflow conditions

A uniform velocity (U_0) was imposed at the inlet of the computational model. The inlet velocity was determined at a value of 0.05 m/s by using Eq. (4.8):

$$U_0 = \frac{Q}{A_i} = \frac{nV}{A_i} \tag{4.8}$$

where Q is the flow rate (m^3/s), A_i the effective inlet surface area (m^2), n the number of air changes (= 1/h) and V the volume of the enclosure (m^3). The inlet air temperature (T_i) according to the experimental data was 16 °C. The inflow conditions for turbulence were characterized by the turbulence intensity $I = 10\%$ and a calculated hydraulic diameter $D_H = 0.47$ m using Eq. (4.9):

$$D_H = \frac{4A}{P} \tag{4.9}$$

where A is the inlet opening area (m^2) and P the perimeter of the inlet opening (m).

Outflow conditions

Zero static gauge pressure was applied at the outlet. The backflow temperature (T_o) according to the experimental data was 24.3 °C. The turbulence intensity was equal to the inflow condition, namely 10%. The hydraulic diameter D_H for the outlet was calculated using Eq. (4.9) and resulted in a value of 0.31 m.

Wall conditions

The vertical walls within the enclosure were assigned a fixed temperature based on the average value of the measured temperature at five different heights in the experiment (see Table 4.2) [40]. The temperature profile was assigned to the vertical walls in the enclosure under the assumption that the temperatures varied linearly with height.

Table 4.2: Temperature profile of vertical walls related to height

Height [m]	Temperature [°C]
0.08	22.4
0.73	23.4
1.39	24.0
2.04	24.5
2.68	24.4

The interior surface temperatures of the floor (T_{if}) and ceiling (T_{ic}) were not mentioned in the initial reference study. Therefore, in addition, the study of Gilani et al. [40] was used, which describes the procedure to estimate these interior surface temperatures. T_{if} and T_{ic} were estimated at a value of 23.85 and 24.2 °C, respectively. The detailed description of the procedure used in the calculation of the interior surface temperatures can be found in the case study of Gilani et al. [40]. Although the procedure used quite some assumptions, the results were considered to be of sufficient accuracy to use within the numerical simulation.

Furthermore, no-slip conditions were applied to the walls of the enclosure.

4.2.4 Solver settings

The 3D steady RANS equations were solved using the RNG k-ϵ model combined with the two-layer EWT zonal model to resolve the viscous sublayer. The k-ϵ models were in general developed for high Reynolds number flows in which the viscous sublayer by default was resolved by a (standard) wall function. However, as mentioned in Section 4.1.2 it is important to resolve the viscous sublayer to accurately predict the near wall flow (i.e. flow separation and reattachment) and heat transfer within the boundary layer [41].

Heat transfer between the boundary of a solid and fluid particle is realized through conduction due to the lack of motion as a result of the no-slip condition at the boundary (see Section 2.3). The fluid particle will eventually transfer the energy to adjacent fluid layers by convection until the temperature gradient reaches a so-called free stream temperature. The development of the temperature gradient from the surface to the free stream is also known as the thermal boundary layer (see Fig. 2.3) [42] [14]. The viscous sublayer dominated by viscous forces plays an important role in resolving heat transfer. Therefore, EWT (i.e. LRNM for k-ϵ models) was used while monitoring the dimensionless wall distance (y^*) in the near-wall region.

The SIMPLEC algorithm was used for pressure-velocity coupling, PRESTO! scheme for pressure interpolation and the second-order discretization scheme was used for momentum, k, ϵ and energy. The numerical simulations were performed using ANSYS Fluent 19.2 (2018).

The scaled residuals showed strong oscillating behavior such that convergence could only be obtained by examining the average solution at three different heights along the measurement pole, namely z = 0.05 m, z = 1.35 m, and z = 2.70 m. The average solution was obtained by enabling data sampling for steady statistics using a sampling interval of 1 once a stable oscillation was observed. The variable of interest for monitoring convergence was the mean static temperature T. The solution was considered converged once the difference in average values at each individual point over an interval of 5,000 – 10,000 iterations becomes less than 1% [33] [43].

4.2.5 Grid-sensitivity analysis

The results of the grid-sensitivity analysis displayed in Figures 4.8a, 4.8c, and 4.8e show there is a good agreement between the temperature profiles of the basic and fine grid. The differences between both profiles occur in the upper region of the enclosure ($z/H > 0.6$) over the measurement pole and sampling line-1 and line-2. However, especially for the measurement pole and sampling line-1, the agreement was considered to be good.

The discretization error was estimated by defining the GCI in a similar way as done in Section 4.1.5. The GCI was calculated between the basic and fine grid for the mean static temperature T using Eq. (4.10) with $F_s = 1.25$, $r = \sqrt{2}$ and $p = 2$.

$$GCI_{basic} = F_s \left| \frac{r^p \left(T_{basic} - T_{fine} \right)}{1 - r^p} \right| \tag{4.10}$$

Figures 4.8b, 4.8d and 4.8f show the results for the estimated GCI. The average GCI along the measurement pole and sampling line-1, and line-2 were estimated at 0.21, 0.18, and 0.23, respectively. The results of the grid-sensitivity analysis show that the use of the basic computational grid was sufficient to proceed with the validation.

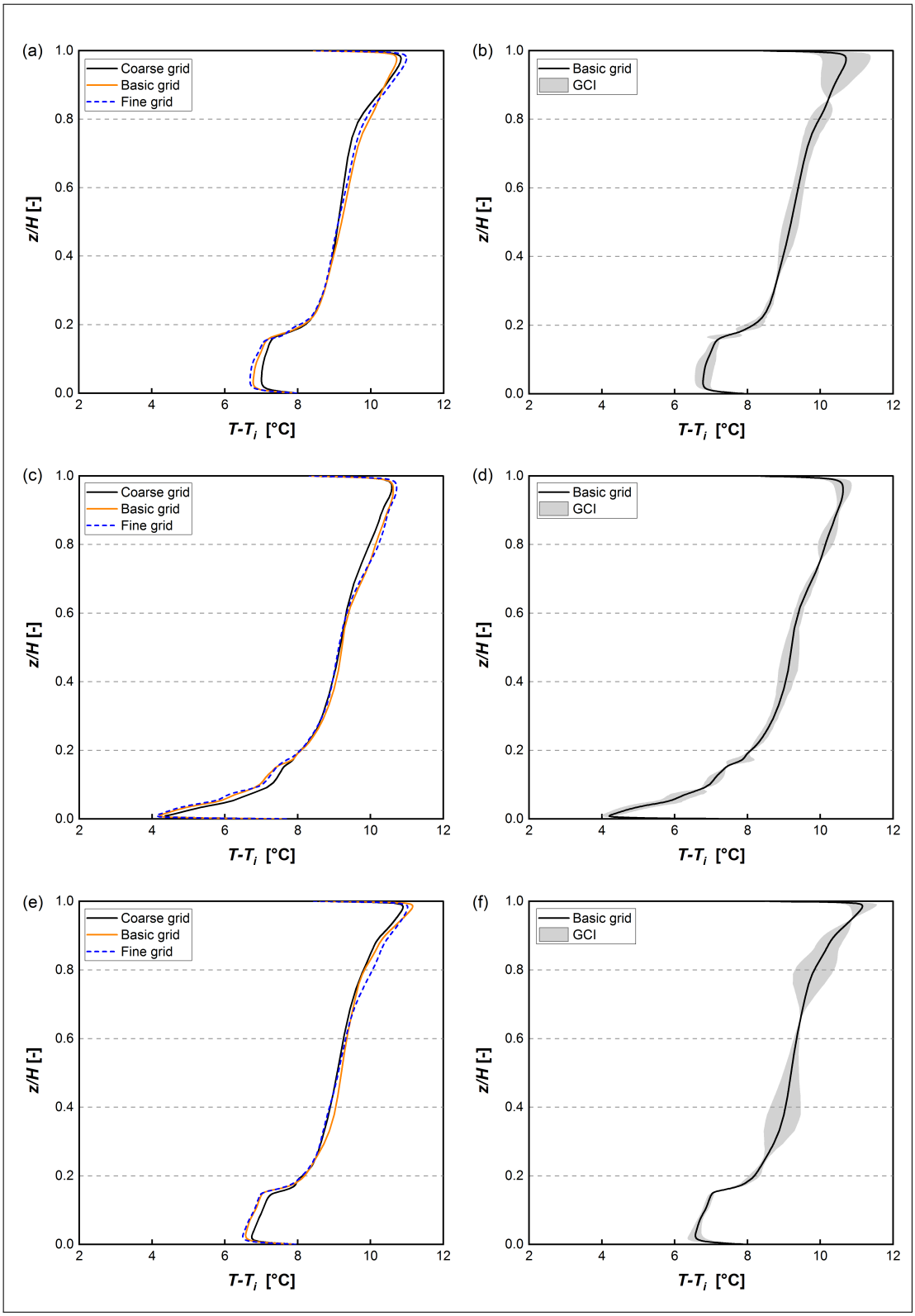

Figure 4.8: Results of grid-sensitivity analysis: $T - T_i$ at (a) measurement pole, (c) sampling line-1, (e) sampling line-2. GCI for basic grid: (b) measurement pole, (d) sampling-line 1, (f) sampling-line 2.

4.2.6 Results

In Figure 4.9a the numerical temperature profile is compared to the experimental data along the measurement pole. An overprediction in temperature was found in the lower region ($z/H < 0.1$) of the enclosure which indicates that the penetration depth of the colder low-velocity supply was less than in the experiments. Therefore, the temperature within the enclosure increased as noticed by the overprediction which was present along an extensive part of the measurement pole. The difference in the lower region of the enclosure could be caused by the additional boundary condition for the floor temperature (T_{if}) derived by Gilani et al. (see Section 4.2.3) [40].

However, similar to the experiment a clear stratification was observed within the enclosure with heavier air (lower temperature) in the lower region and lighter air (higher temperature) in the upper region. The flow was affected by the gravity current of the colder low-velocity supply and the thermal plume generated by the heat source [10] [40].

To indicate the error between the numerical results and the experimental data, a scatter plot was made. From Figure 4.9b, it is concluded that the differences between both data sets were relatively small. Most data points lie within the range of +/- 10%. The use of the basic computational grid together with the boundary conditions and computational settings resulted in a good agreement with the experimental data.

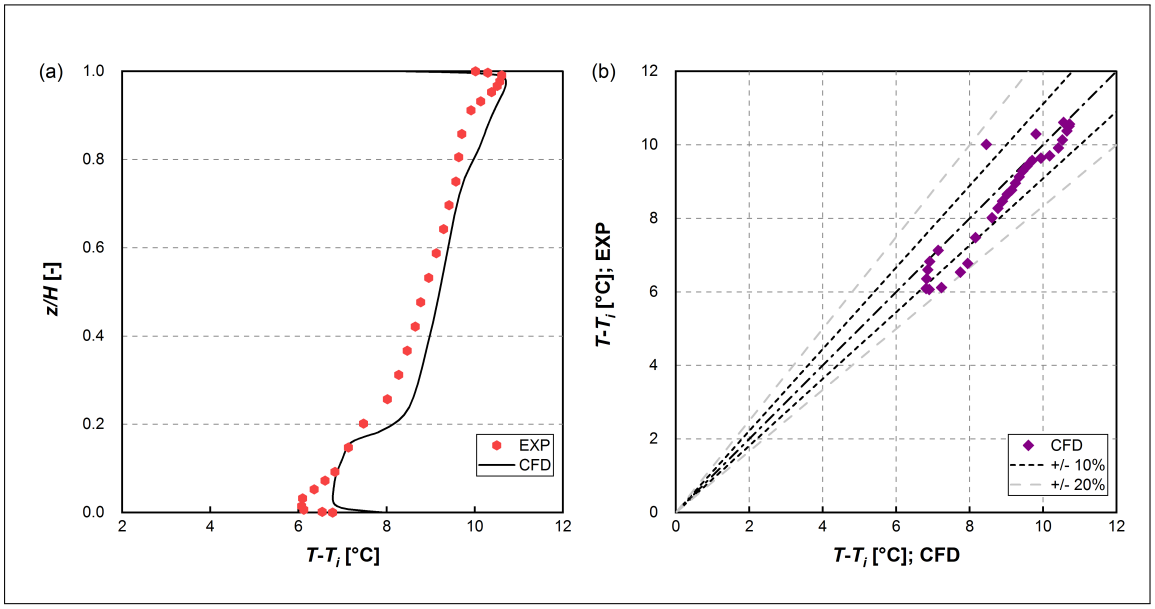

Figure 4.9: Validation and error assessment of $T - T_i$

4.2.7 Turbulence model sensitivity analysis

A sensitivity analysis was conducted to indicate the influence on the numerical results of different turbulence models in the 3D steady RANS simulations. In general, the performance of a turbulence model is considered to be problem-dependent due to differences in the physical characteristics of the study, the computational grid, boundary conditions, and settings. Therefore, a universal best-performing turbulence model for indoor airflow simulation is absent [40] [44].

However, multiple studies conducted on the performance of different turbulence models for indoor airflow simulation indicate that the two-equation models, in particular the Renormalization Group k-ϵ (RNG) and Shear Stress Transport k-ω (SST) turbulence models, perform with superior accuracy [31] [40] [45]. In addition, the Standard k-ϵ (SKE) turbulence model was added to the sensitivity analysis due to its robust character, simplicity and reasonable accuracy for a broad range of applications [31] [32].

As described in Section 4.2.4, the EWT two-layer zonal model was applied to resolve the viscous sublayer in the case of k-ϵ models. The k-ω model resolves the near-wall flow using the two-equation models k-ω in the inner region and k-ϵ in the outer region of the boundary layer. By applying blending functions, the k-ω model ensures a smooth transition between the two regions depending on near-wall mesh refinement (y^*) [32].

In Figure 4.10, the numerical results for each turbulence model are compared to the experimental data. It is concluded that the RNG k-ϵ model has the best agreement along the vertical pole.

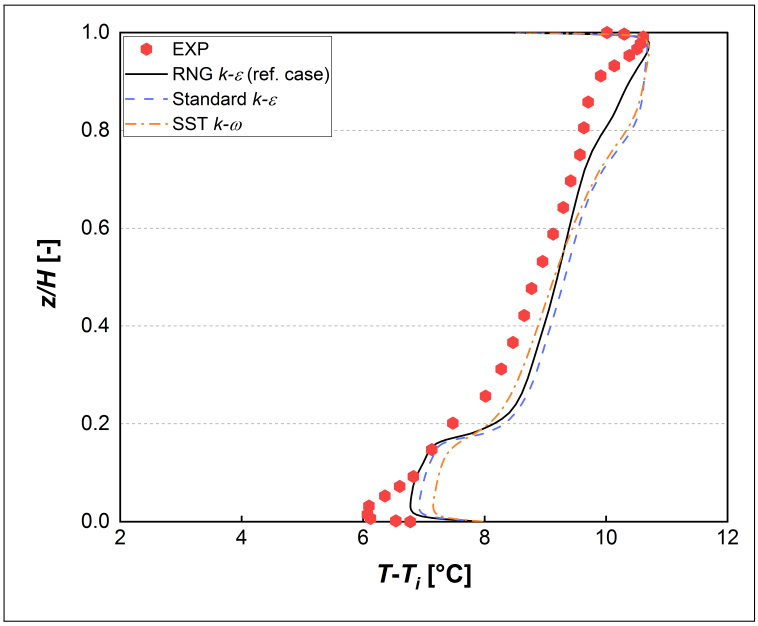

Figure 4.10: Turbulence model sensitivity analysis of $T - T_i$.

To quantify the error between the numerical results for each turbulence model and the experimental data, the validation metrics root-mean-square error (RMSE) and factor of 1.1 observations (FAC1.1) were calculated using Eq. 4.11 and 4.12:

$$RMSE = \sqrt{\frac{\sum_{i=1}^{n}(P_i - O_i)^2}{n}} \tag{4.11}$$

$$FAC1.1 = \frac{1}{n}\sum_{n=1}^{n} N_i \;\; with \;\; N_i = \begin{cases} 1 & for\ 0.91 \leq \frac{P_i}{O_i} \leq 1.1 \\ 0 & else \end{cases} \tag{4.12}$$

where O_i is the observed (experimental) value and P_i the predicted (numerical) value. The results of the validation metrics RMSE and FAC1.1 shown in Table 4.3 correspond with the observations made from Figure 4.10, namely that out of all turbulence models the RNG k-ϵ model was the best-performing model.

Table 4.3: Validation metric results for mean static temperature T

	RMSE	**FAC1.1**
Ideal value	0	1
Standard k-ϵ	0.71	0.77
RNG k-ϵ	0.60	0.80
SST k-ω	0.68	0.77

4.3 Conclusion

The 3D non-isothermal validation study confirmed that the RNG k-ϵ turbulence model performed with good accuracy , which is similar as in the 2D isothermal validation study. Although the use of a certain turbulence model was considered to be case-specific, it is decided to continue further with the research using the best-performing solver settings from the two validation studies.

5 — Case study

5.1 Generic office

In the subsequent chapter, the numerical setup of the generic office model described in Chapter 3 along with the used conditions and assumptions are summarized..

5.1.1 Computational geometry

The generic office model was represented by a rectangular enclosure with dimensions 3.6 x 5.4 x 2.7 m^3 (W x L x H (see Fig. 5.1). The height of the enclosure was chosen to correspond to the validation study performed in Subsection 4.2. Furthermore, additional information on the characteristics of the geometry were summarized in Subsection 3.2.

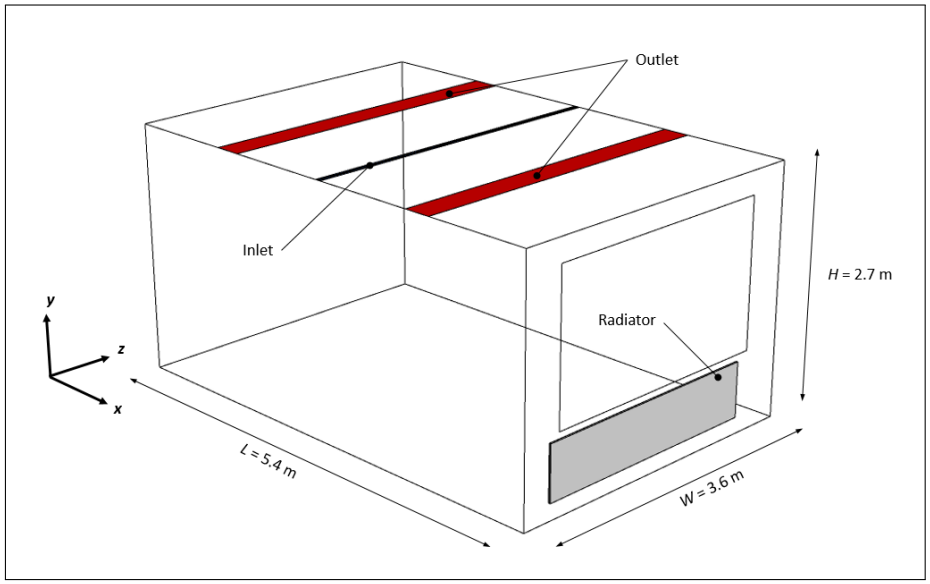

Figure 5.1: 3D Computational geometry

5.1.2 Computational grid

One computational grid suitable for all scenarios was constructed to accurately simulate and compare the individual scenarios by applying small adjustments (i.e. switch from a solid- to fluid radiator volume and provide the possibility to decrease the surface area of the climate ceiling). The computational grid was eventually separated into two sections to reduce the number of cells while remaining a high-quality grid for all scenarios (see Fig. 5.2). Firstly, in the boundary layer regions where convective heat transfer takes place, a structured boundary layer grid was formed using hexahedral cells only. Secondly, an unstructured inner region of the domain was formed using quadrilateral cells built with the quad pave face meshing method.

The computational grid consists of 2,686,970 hexahedral cells.

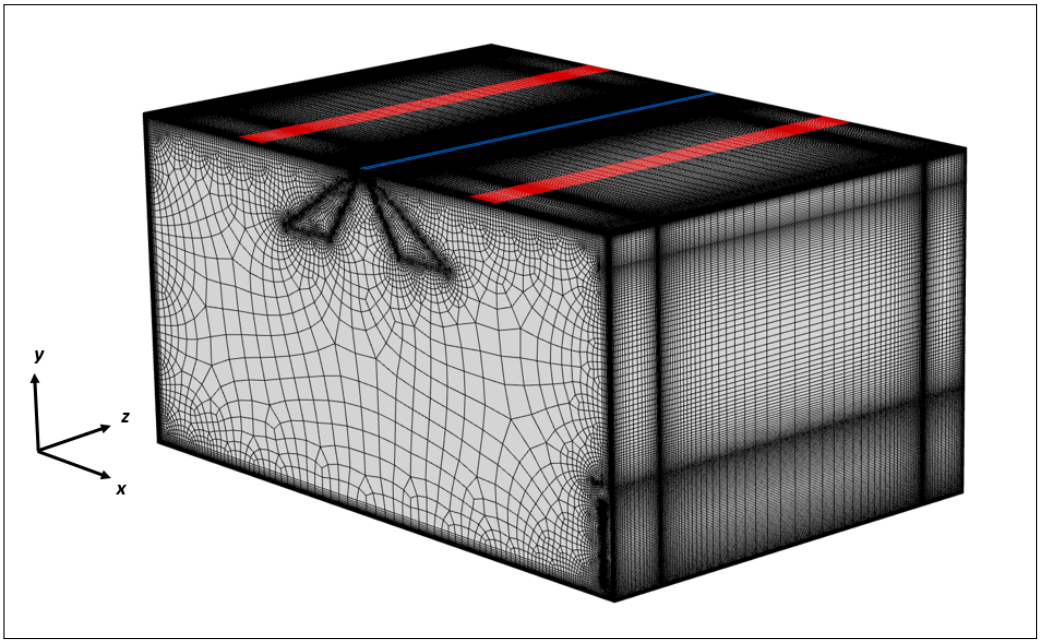

Figure 5.2: 3D computational grid (= 2,686,970 cells)

The structured boundary layer grid was formed to resolve the viscous sublayer, i.e. to ensure y^* values were below the recommended threshold to enable LRNM (see Subsection 4.1.2). The first cell layer height from the domain walls was 0.0005 m to ensure multiple cells were located within the viscous sublayer [40]. However, the first cell layer height from the radiator walls was increased to 0.002 m by examining the y^* values extensively through trial-and-error. Increasing the first cell layer height decreased the number of cells within the computational grid and y^* values remained sufficient to enable LRNM. Furthermore, the maximum stretching ratio in the boundary layer was 1.2 and 10 cells were using along the width of the inlet and outlet.

To ensure a high-quality computational grid, the transition between the structured and unstructured section was carefully examined in terms of aspect ratio, skewness, and maximum stretching ratio (see Fig. 5.3 a-c).

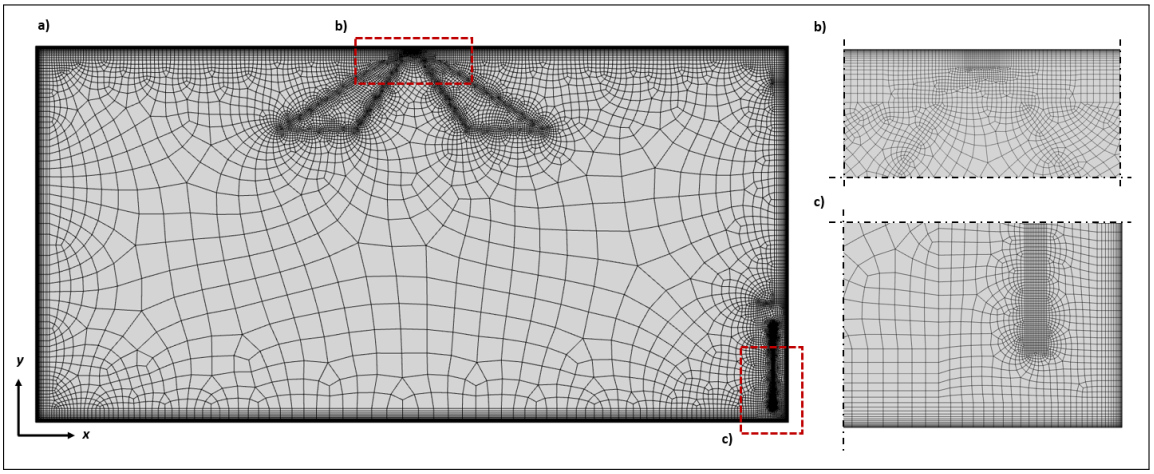

Figure 5.3: (a) Cross-section of computational grid. (b-c) Close-up view of grid: (b) inlet region; (c) radiator

The y^* values were examined on the surfaces at which the highest velocity was expected, namely the radiator (thermal plume), ceiling (inlet region), and external wall (downdraught). The maximum and average y^* values were examined for all individual scenarios and summarized in Table 5.1. The recommended value of $y^* < 5$ was locally exceeded along the ceiling and radiator for all four scenarios. However, the average y^* values were well below the recommended value and therefore it is concluded that the computational grids have a sufficient near-wall grid resolution for LRNM.

Table 5.1: Maximum and average y^* values for the individual scenarios

	Radiator		**Ceiling**		**External wall**	
	Max	**Avg**	**Max**	**Avg**	**Max**	**Avg**
Scenario 1	9.05	3.87	7.21	0.35	1.00	0.44
Scenario 2	-	-	7.20	0.22	0.86	0.48
Scenario 3	6.63	2.82	7.20	0.29	0.90	0.48
Scenario 4	7.89	2.35	7.21	0.28	0.88	0.46

5.1.3 Boundary conditions

The boundary conditions applied to the reference scenario of the generic office (i.e. Scenario 1) are summarized below. The transition scenarios that deviate from the initial boundary conditions are briefly summarized alongside to provide an extensive overview.

The computational domain was divided into two separate zones, namely a fluid-type zone for the air inside the enclosure and a solid-type zone for the radiator. The individual zones were thermally coupled using a wall boundary condition on the interface between the fluid and solid zone. For Scenario 2, the two separate zones were merged into one fluid-type zone as the radiator was removed.

Inside the enclosure, the density of air (ρ) was calculated as a function of temperature by applying the incompressible gas law. Furthermore, solid materials were defined according to reference materials used within the generic office (see Table 5.2).

Table 5.2: Solid material properties [46]

Material type	ρ [**kg/m^3**]	λ [**W/m·K**]	c [**J/kg·K**]	**Surface**
Aluminium	2719	202.4	871	Radiator, climate ceiling
Concrete	2400	1.7	840	Floor, external wall
Glass (plain)	2500	0.8	840	Window
Sand-lime	2000	1.0	840	Internal walls
Gypsum board	1400	0.46	840	Ceiling

Inflow conditions

A uniform velocity (U_0) was imposed at the centralized linear slot diffuser under an angle of 45°. The inlet velocity was determined at a value of 0.48 m/s by using Eq. (4.8) where Q is the flow rate (= 0.03 m^3/s) and A_i the effective inlet surface area (= 0.063 m^2) as mentioned in Subsection 3.2.

. The inflow conditions for turbulence were characterized by the turbulence intensity (I) of 10% and a turbulent viscosity ratio of 10 (see Subsection 4.2.3).

Outflow conditions

Zero static gauge pressure was applied at the outlet and the backflow temperature (T_0) was 21 °C. The outflow conditions for the turbulence were similar to the inflow conditions.

Wall conditions

An adiabatic relation was assumed between the enclosure and adjacent volumes. Therefore, the internal construction elements (i.e. walls, floor, and ceiling) had a fixed heat flux of zero. Transmission losses through the facade were addressed by applying a fixed temperature to the transparent and opaque facade elements.

The fixed surface temperature for the transparent and opaque elements was calculated at a value of 7.15 and 19.44 °C, respectively by using Eq. (5.1):

$$\Delta T_n = \frac{R_n}{R_l} \cdot \Delta T \tag{5.1}$$

where ΔT_n is the temperature jump across layer n (°C), R_n the heat resistance of layer n (m^2·K/W), R_l the heat resistance of air on air of the total construction (m^2·K/W) and ΔT the difference in temperature between the air on both sides of the construction (°C). R_l was calculated using Eq. (5.2):

$$R_l = R_{si} + R_c + R_{se} \tag{5.2}$$

where R_{si} and R_{se} are the internal and external heat transfer resistances for a construction bordering the outdoor environment (m^2·K/W) and R_c the heat resistance of the element (m^2·K/W) [23]. The detailed calculation of the surface temperatures was summarized in Appendix B.

Furthermore, no-slip conditions were applied to the walls of the enclosure.

Heating conditions

The energy released from the radiator was initially imposed by a fixed heat flux on the walls estimated according to the required energy input from the energy balance (i.e. 629.94 W). To satisfy the energy balance for the different temperature trajectories used by the radiator, the selection power output Φ_s was determined using the ISSO-publication 66 [47]. The heat flux q was eventually calculated using Eq. 4.7 in which the volume of the radiator is multiplied with the required energy input (see Appendix C).

The calculated heat flux should provide surface temperatures in between the supply T_s and return T_r temperatures of the specific trajectory (i.e. HTH = 70 °C, MTH = 50 °C, and LTH 32.5 °C) (see Section 3.3). However, it was noted through trial-and-error that the surface temperatures achieved with an imposed fixed heat flux resulted in average temperatures much lower than expected (i.e. HTH = 52.2 °C, MTH = 25.0 °C, and LTH 22.3 °C). To address the difference in simulated and expected surface temperatures it was decided to impose a fixed temperature on the walls of the radiator. The fixed temperatures for the walls of the HTH, MTH, and LTH radiators were 70, 45, and 32.5 °C, respectively. The fixed temperature boundary condition increased the energy input compared to the calculated energy balance, however, the air temperatures were carefully monitored such that similar indoor conditions were simulated between the scenarios.

In the transition scenarios in which the capacity of the radiator was lowered or removed, a combination was made with the climate ceiling to provide comparable indoor conditions. Scenario 2 was used to estimate the energy released from the climate ceiling through trial-and-error. Matching the energy input of the climate ceiling to the initial HTH radiator resulted in too high indoor temperatures. The energy release of the climate ceiling was therefore lowered to a fixed heat flux of 60.13 W/m^2 which resulted in similar indoor conditions. The fixed heat flux resulted in a surface temperature between 31 and 33 °C which matched the temperature trajectory of LTH (i.e. T_s = 35 °C and T_r = 30 °C). The surface temperature on the climate ceiling fluctuates under the influence of the convective heat transfer coefficient (h) compared to a fixed temperature. The coefficient depends strongly on the physical properties of the fluid and the physical situation which causes the fluctuation [32]. Further loss in heating capacity in Scenario 3 (i.e. MTH) and Scenario 4 (i.e. LTH) was compensated by adjusting the surface area of the climate ceiling instead of adjusting the heat flux. This resulted in an equal situation for all three scenarios in which the energy released per square meter remained similar. The required surface area of the climate ceiling needed to compensate for the loss in heating capacity in Scenario 2, 3, and 4 were 16.74, 10.81, and 14.81 m^2, respectively.

The climate ceiling used in Scenario 2 covers approximately 85% of the entire ceiling surface (i.e. 19.44 m^2). The surface of the climate ceiling was estimated by subtracting the inlet and outlet surface of the ventilation from the total ceiling surface. However, the maximum percentage of an active climate ceiling compared to the floor surface is 80% which was slightly exceeded [48]. The exceedance was caused due to simplifications in the computational geometry to facilitate the generation of a high-quality computational grid. The percentage of ceiling covered by the climate ceiling for Scenario 3 and 4 were 55% and 76%, respectively.

Although the total heat transfer of each scenario differs, similar indoor conditions were observed which could be compared and evaluated more accurately. The total heat transfer of each scenario is summarized in Table 5.3. It is observed that the heat transfer in all scenarios is larger than the required energy calculated in the energy balance (i.e. 629.94 W).

Table 5.3: Total heat transfer for each individual scenario

	Heat transfer radiator [W]	Heat transfer climate ceiling [W]	Total
Scenario 1	1883.94	-	1883.94
Scenario 2	-	1000.80	1000.80
Scenario 3	519.98	776.82	1296.8
Scenario 4	392.84	890.27	1283.11

5.1.4 Solver settings

The solver settings were largely similar to the settings summarized for the validation study in Subsection 4.2.4. 3D steady RANS equations were solved using the RNG k-ϵ model combined with the two-layer EWT zonal model. The SIMPLEC algorithm was used for pressure-velocity coupling, PRESTO! scheme for pressure interpolation and the second-order discretization scheme was used for momentum, k, ϵ, and energy. The numerical simulations were performed using ANSYS Fluent 19.2 (2018).

In addition to the validation study, the radiation model Surface-to-Surface (S2S) was implemented to account for radiation exchange in the enclosure. The model calculates so-called view factors which determine the energy exchange between the surfaces of the enclosure. The energy exchanged between the individual surfaces depends strongly on size, distance and orientation [32]. The S2S radiation model was enabled using default values from ANSYS Fluent.

The scaled residuals showed strong oscillating behavior and convergence was examined through the average solution in three measurement points. The XYZ-coordinates for each point were (4.6, 0.1, 1.8), (4.6, 1.1, 1.8) and (4.6, 1.8, 1.8), respectively. The average solution was obtained by enabling data sampling for steady statistics using a sampling interval of 1 once a stable oscillation was observed. The variables of interest for monitoring convergence were the mean velocity magnitude (U) and mean static air temperature (T). The solution was considered converged once the difference in average values at each individual point over an interval of 5,000 - 10,000 iterations becomes less than 1% [33] [43].

6 — Results

6.1 Evaluation parameters

As mentioned in Section 2.1, thermal comfort can be evaluated on the entire body of the occupants or on individual parts of the body (i.e. local discomfort). The parameters of local discomfort provide a more global evaluation of thermal comfort compared to the entire body. It is therefore decided to evaluate thermal comfort based on the local discomfort parameters: draught rate (DR), the vertical temperature gradient between the head of a seated person and its ankle ($\Delta T_{a,v}$), and the floor surface temperature range (T_f) according to the NEN-EN-ISO 7730 [11]. Furthermore, the mean air temperature (T), mean velocity magnitude (U), and turbulence intensity (I) were examined due to their contribution in the calculation of DR. In addition to the local discomfort parameters, the research also focusses on the whole-body parameter PMV and the operative temperature (T_{op}) to provide a more extensive evaluation.

The NEN-EN-ISO 7730 classifies the thermal environment into three different categories based on the above-mentioned parameters. The categories range from C (i.e. acceptable) to A (i.e. very good) [11]. The research aims to investigate whether an improved or similar indoor environment can be achieved compared to the initial Scenario 1 in the transition from high-temperature to low-temperature heating. To evaluate the thermal comfort between the different transition scenarios, it was decided to focus on the NEN-EN-ISO 7730 category B classification (see Table 6.1). In practice, the category B classification is often used for a new or improved situation compared to the category C classification which is more typical for existing buildings.

Table 6.1: Reference values for the discomfort parameters according to NEN-EN-ISO 7730 [11]

Parameter	**Category A**	**Category B**	**Category C**
DR [%]	< 10	< 20	< 30
$\Delta T_{a,v}$ [°C]	< 2	< 3	< 4
T_f [°C]	19 to 29	19 to 29	17 to 31
T_{op} [°C]	22.0 ± 1.0	22.0 ± 2.0	22.0 ± 3.0
PMV	$-0.2 <$ PMV $< +0.2$	$-0.5 <$ PMV $< +0.5$	$-0.7 <$ PMV $< +0.7$

The results are observed on two reference planes within the enclosure to provide contour plots of the parameters U, T, I, and DR. One vertical plane (i.e. z = 1.8 m) and one horizontal plane (i.e. y = 0.1 m) were used to show the results. The horizontal plane resembles the average height of a human ankle from which often local discomfort is evaluated.

The individual discomfort parameters are examined within the occupied zone defined as the zone 0.5 m from the facade, 0.3 m from internal walls, and up to 1.8 m above the floor. The discomfort parameter $\Delta T_{a,v}$ is examined in 20 points along two reference lines representing the ankle (i.e. y = 0.1 m) and the head of a seated person (i.e. y = 1.1 m) (see Fig. 6.1a). The discomfort parameter T_f is examined using the surface integral option under reports in ANSYS Fluent to obtain the area-weighted average values of the floor surface. Furthermore, the index PMV and parameter T_{op} are examined using a fictive point representing a seated person behind an office desk in a standardized layout on XYZ coordinates (4.25, 1.10, 0.82) (see Fig. 6.1b).

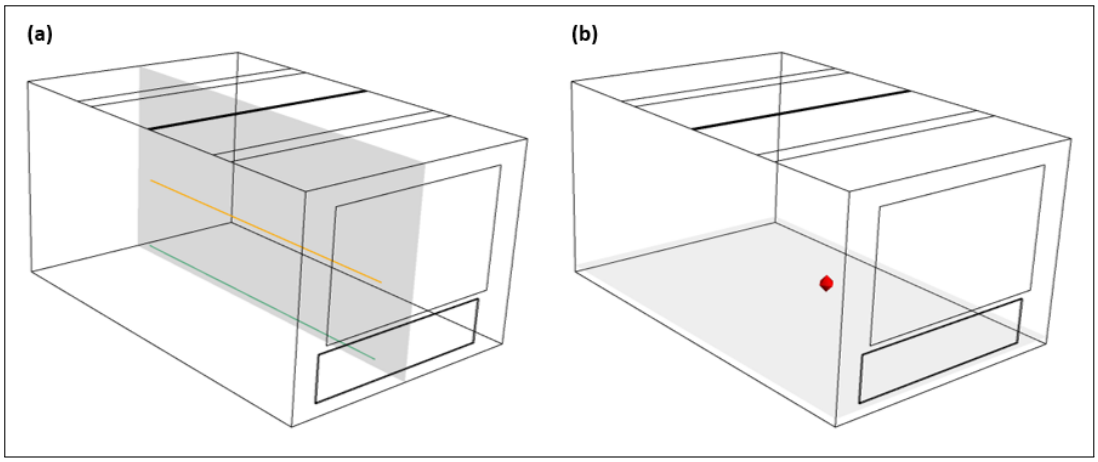

Figure 6.1: (a) Vertical center plane (i.e. z = 1.8 m). (b) Horizontal center plane (i.e. y = 0.1 m)

6.1.1 Mean velocity magnitude

The results of U for each scenario on the center and horizontal plane are presented in Figures 6.2 and 6.3. In general, it is observed that the expected inflow pattern from the linear slot diffuser (i.e. under an angle of 45°) was altered in all scenarios due to the thermal plume originating from the radiator and/or the downdraught generated on the facade causing a recirculation flow. The inflow pattern from the linear slot diffuser is checked on reliability through a small sensitivity analysis using a 2D representation of the computational geometry (see Appendix D). Furthermore, the velocity vectors and streamlines for each scenario are presented in Appendix E.

In Scenario 1, the fluid layer adjacent to the radiator is heated and under the influence of buoyancy forces creates an upward jet-like flow (i.e. thermal plume). The maximum velocity in the thermal plume is achieved just above the radiator as the diameter of the plume is the narrowest at that particular position . The thermal plume attaches to the facade under the influence of the Coanda-effect and of entrainment. The diameter of the plume increases over the height of the facade (see Fig. 6.2a). The acceleration of the thermal plume propagates on the ceiling and redirects the inflow pattern from the centralized linear slot diffuser. The inflow is redirected towards the back wall resulting in a recirculation flow throughout the enclosure. The recirculation reconnects with the thermal plume under the radiator which creates a co-flow in the same direction as the plume boosting the velocity and volume flow rate .

In Scenario 2, the immediate effect of the removal of the radiator is observed. The thermal plume is replaced by a cold downdraught generated under the influence of negative buoyancy forces. In Figure 6.2b the growth of the boundary layer thickness is visualized due to entrainment (see Section 2.3). The vertical flow transitions towards a horizontal gravity current in which small density differences are experienced and under the influence of its acceleration penetrates the occupied zone [49]. The maximum velocity observed at the facade and floor was 0.37 and 0.30 m/s, respectively, and occurred at a certain distance from the facade following the velocity distribution in the boundary layer 2.3).

In Scenario 3, the buoyancy forces in the thermal plume decreased as the surface temperature of the radiator was reduced (i.e. MTH = 50 °C). The plume does not attach to the facade (i.e. no Coanda-effect) and its influence on the inflow pattern also decreased. Instead of redirecting the inflow pattern towards the back wall, it was redirected perpendicular to the ceiling in the occupied zone. As a result of the redirected inflow pattern, increased velocities were observed at the floor region creating two recirculating flows in the enclosure.

In Scenario 4, the buoyancy forces in the thermal plume decreased even further and the plume is difficult to observe. The counteracting force (i.e. thermal plume) disappeared and cold downdraught can therefore regenerate on the facade. However, due to the presence of the radiator, the downdraught was limited in its acceleration and penetration in the occupied zone. The maximum velocity observed at the facade and floor was 0.24 and 0.21 m/s, respectively.

Compared to the initial Scenario 1, U increased in both transition scenarios in which LTH was used (i.e. Scenario 2 and 4). The influence of the counteracting force (i.e. thermal plume) has an important role in the velocity distribution in the occupied zone. Once the thermal plume decreases (i.e. Scenario 2) or is removed (i.e. Scenario 4), downdraught has a free pathway towards the occupied zone. To decrease the impact of downdraught in these scenarios, it is required to lower the temperature difference between the transparent facade element and the surrounding air to decrease the impact of the buoyancy forces in the flow..

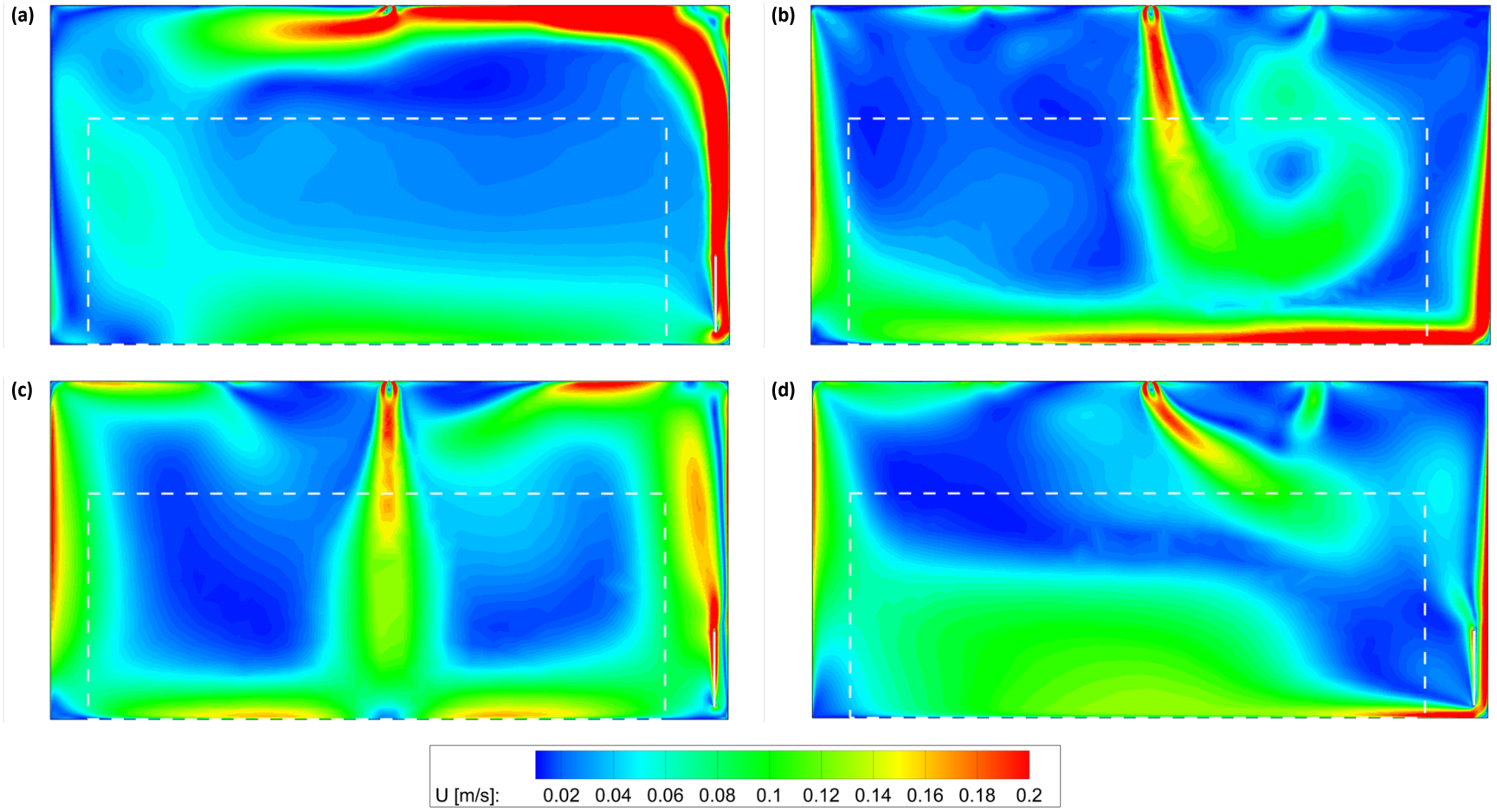

Figure 6.2: Mean velocity magnitude U (m/s) on the center plane (i.e. z = 1.8 m): (a) Scenario 1. (b) Scenario 2. (c) Scenario 3. (d) Scenario 4. The dashed box indicates the occupied zone

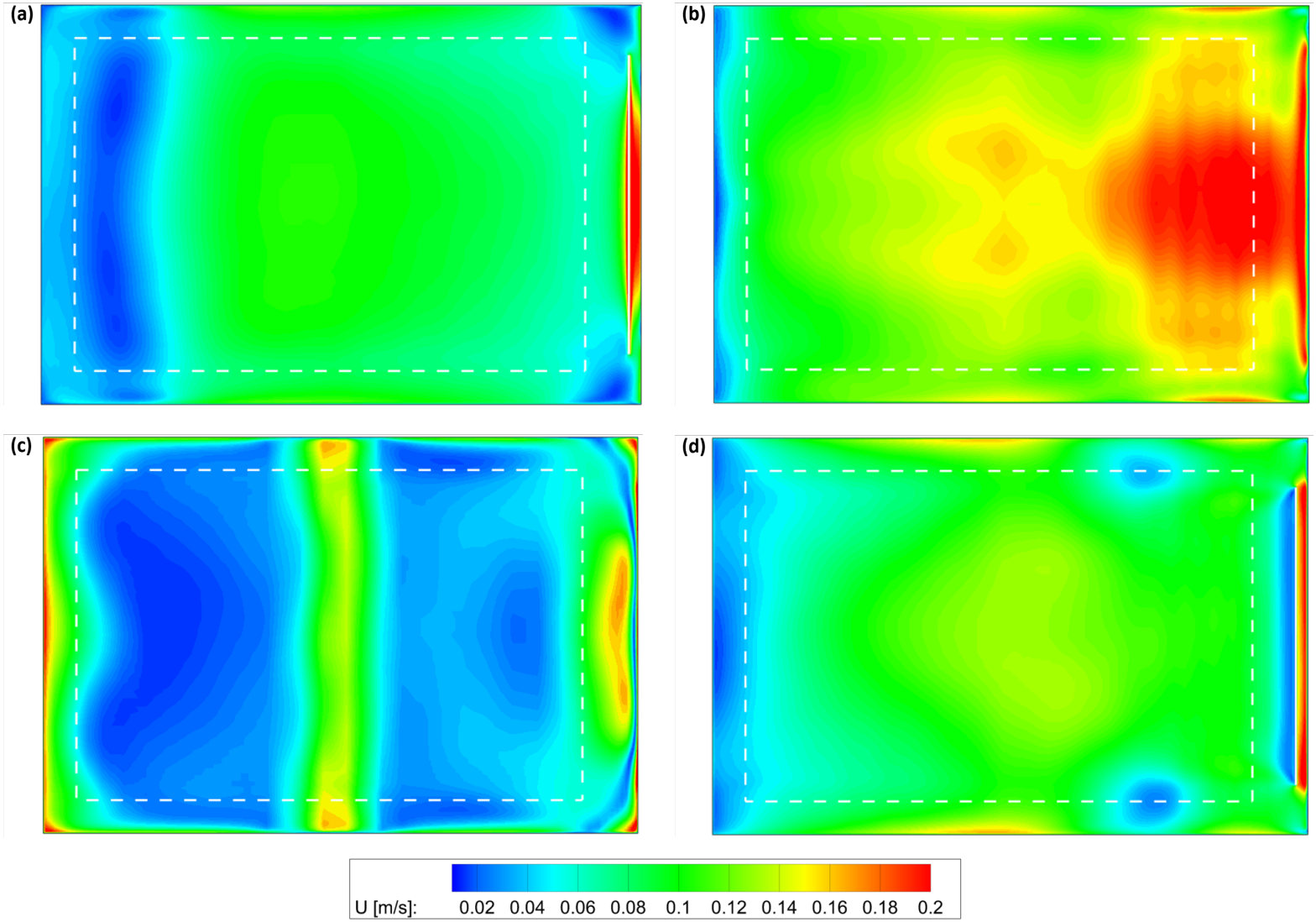

Figure 6.3: Mean velocity magnitude U (m/s) on the horizontal plane (i.e. y = 0.1 m): (a) Scenario 1. (b) Scenario 2. (c) Scenario 3. (d) Scenario 4. The dashed box indicates the occupied zone

6.1.2 Mean air temperature

Similar as described for U, T was obtained for the individual scenarios and the results on the center and horizontal plane are presented in Figures 6.4 and 6.5.

In Scenario 1, the convective heat transfer from the radiator is caused by both conduction and advection (i.e. transport by bulk motion of a fluid) [14]. The generated upward motion results in the accumulation of heat below the ceiling and under the influence of the inflow pattern subsequently spreads further in the enclosure. The recirculation flow observed in Figure 6.4a causes the heat to be well-mixed in the enclosure resulting in a homogeneous temperature gradient (see Figs. 6.4a and 6.5a).

In Scenario 2, the radiator is replaced with a climate ceiling from which immediately can be observed that the heat released accumulates underneath the ceiling. The climate ceiling primarily transfers heat through radiation and less by convection. On the facade, a cold downdraught is generated which penetrates colder air into the occupied zone. However, due to the lack of recirculation and the accumulation of heat underneath the ceiling a larger temperature gradient was observed in the enclosure compared to Scenario 1 (see Figs. 6.4b and 6.5b).

In Scenario 3, the convective heat transfer from the radiator has decreased due to a lower surface temperature (i.e. MTH = 50 °C). The temperature on the inner surface of the facade decreased as can be seen in Figure 6.4c. However, due to the redirected inflow pattern which created two recirculation flows in the enclosure, the temperature gradient is similar to Scenario 1 (see Figs. 6.4c and 6.5c). The recirculation flow moves the accumulated heat underneath the ceiling more into the enclosure and occupied zone.

In Scenario 4, the convective heat transfer decreased even further and cold downdraught is dominant on the facade resulting in a flow of cold air that penetrates the occupied zone. Similar to Scenario 2 no recirculation flow is present and the heat accumulated underneath the ceiling does not move. Therefore, a larger temperature gradient can be observed compared to Scenario 1 and 3 (6.4d and 6.5d).

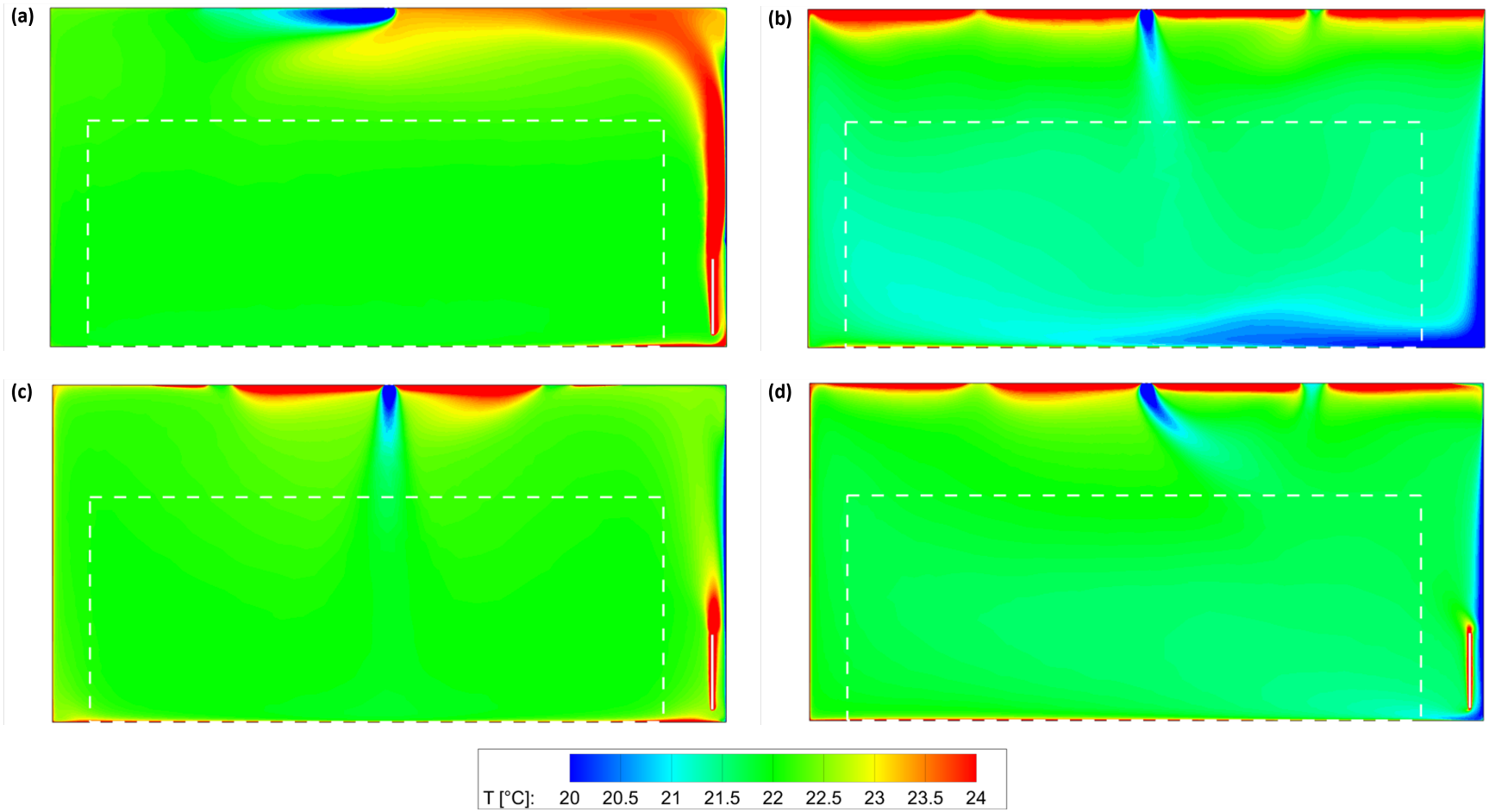

Figure 6.4: Mean air temperature T (°C) on the center plane (i.e. z = 1.8 m): (a) Scenario 1. (b) Scenario 2. (c) Scenario 3. (d) Scenario 4. The dashed box indicates the occupied zone.

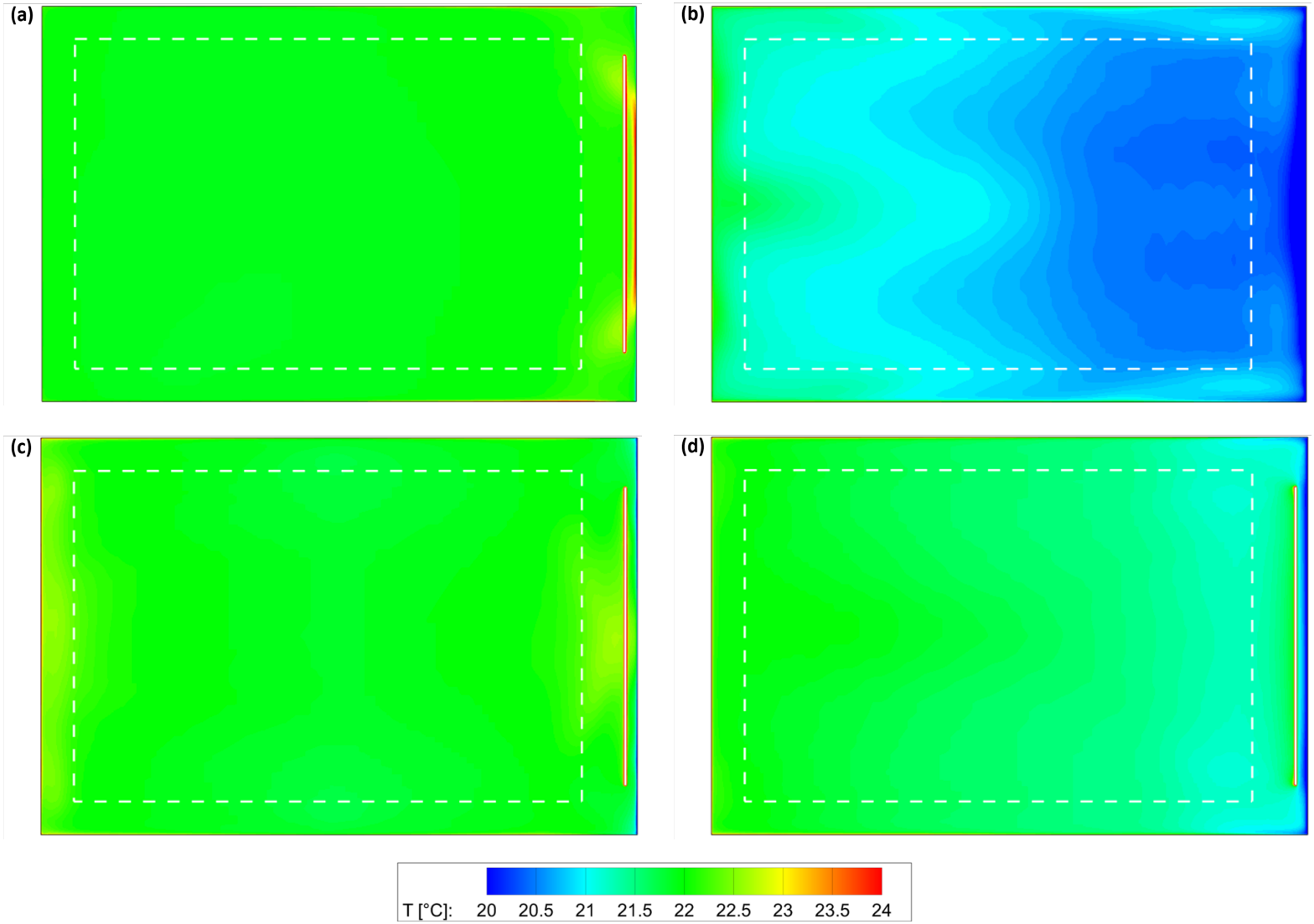

Figure 6.5: Mean air temperature T (°C) on the horizontal plane (i.e. y = 0.1 m): (a) Scenario 1. (b) Scenario 2. (c) Scenario 3. (d) Scenario 4. The dashed box indicates the occupied zone

6.1.3 Turbulence intensity

The turbulence intensity I was calculated as the ratio between the root-mean-square velocity fluctuations and the velocity magnitude using Eq. (6.1) [32]:

$$I = \frac{\sqrt{\frac{2}{3}k}}{U} \tag{6.1}$$

where k is the turbulence kinetic energy (m^2/s^2) and U the mean velocity magnitude (m/s) on the same position in the computational grid. The results of I for each scenario on the center and horizontal plane are presented in Figures 6.6 and 6.7.

From the results, it is observed that the values for I are relatively low within all transition scenarios. Local regions of increased I are formed throughout the generic model which follows in a small manner the velocity profile (i.e. inflow pattern, downdraught, and thermal plume) (see Fig. 6.6a and 6.6c-d). The numerical results of I deviate from the standard I of 40% suggested in the NEN-EN-ISO 7730. The value of 40% is used to examine thermal comfort assuming that air is supplied through a mixed ventilation system [11].

6.1.4 Draught rate

The draught rate DR was calculated using Eq. (6.2) [11]:

$$DR = (34 - T)(U - 0.05)^{0.62} \cdot (0.37 \cdot U \cdot I + 3.14) \tag{6.2}$$

where T is the mean static air temperature (°C), U the mean velocity magnitude (m/s), and I the turbulence intensity (%). The results of DR for each scenario on the center and horizontal plane are presented in Figures 6.8 and 6.9. The DR depends strongly on the variable U as it is placed twice within the equation and therefore the contour plots show similarities with the velocity profiles (see Figs. 6.2 and 6.3).

In Scenario 1 the DR values are considered to be low (i.e. $\leq 7\%$) and cause no discomfort within the occupied zone. The highest values are observed below the ceiling and near the inlet region. In Scenario 2 the DR values are increased on the facade and within the occupied zone compared to Scenario 1. The downdraught generated under the influence of buoyancy forces increases the velocity on the facade which penetrates the occupied zone. In combination with the decreased air temperature, DR increases above the threshold of 20% and causes discomfort in the first 0.5 m of the occupied zone (see Fig. 6.8b). In Scenario 3 regions of relatively high DR values in the middle of the enclosure and on the floor surface are formed as the inlet flow was redirected under the influence of the thermal plume from the MTH radiator. Nevertheless, the values remain below the threshold value of 20% (see Fig. 6.8c). Furthermore, in Scenario 4 the DR values are once again increased on the facade under the influence of downdraught. However, the influence of downdraught does not cause DR to penetrate the occupied zone with values higher than 20% (see Fig. 6.8d).

Overall, the DR values are considered to be good within the occupied zones of Scenario 1, 3, and 4 (see Figs. 6.8 and 6.9). In the case of Scenario 2, the exceedance of DR occurs below ankle level as can be seen in Figure 6.8b. Therefore, it can be assumed that the exceedance of DR has little influence on the comfort perception of the occupants.

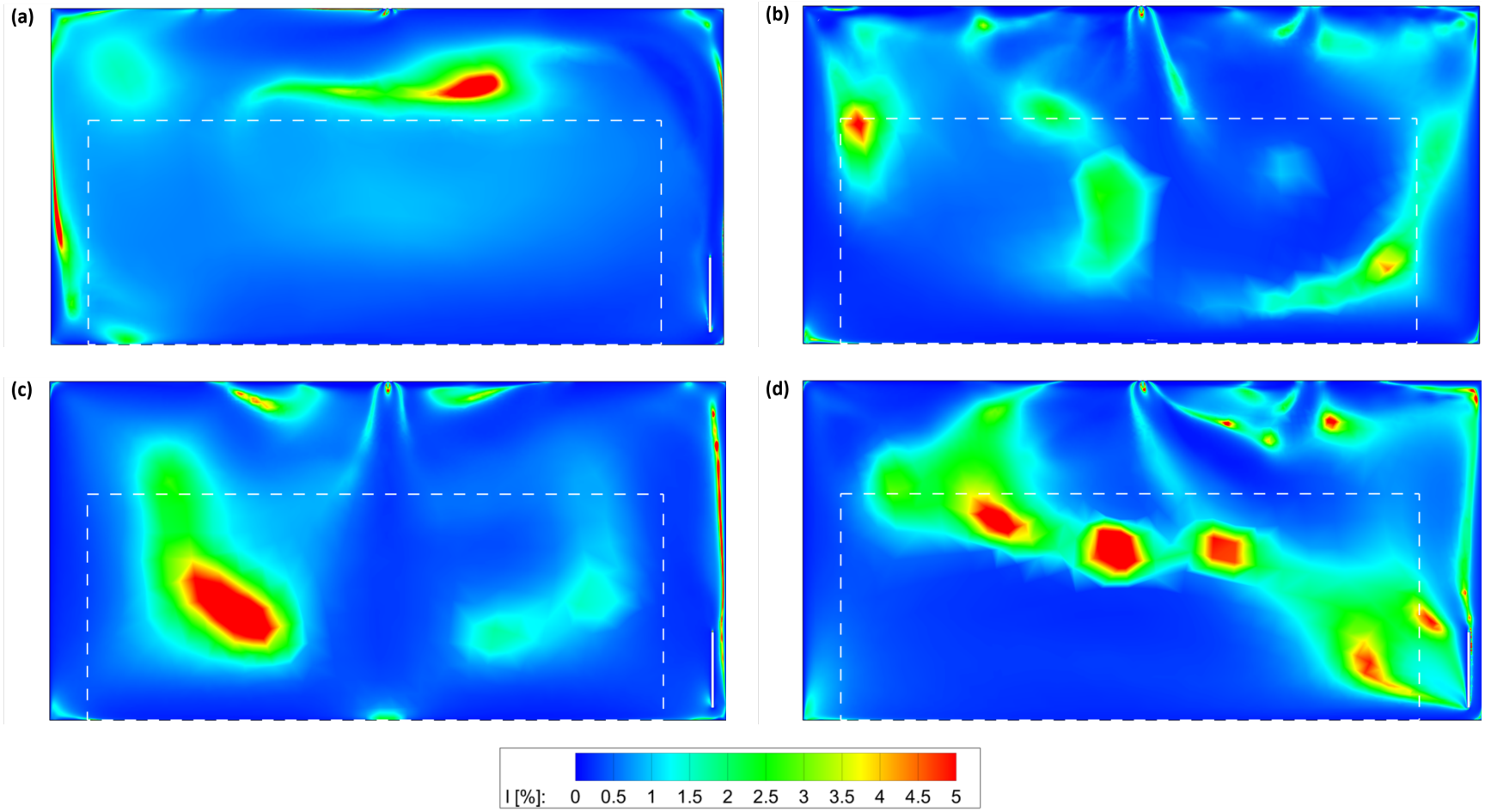

Figure 6.6: Turbulence intensity I (%) on the center plane (i.e. z = 1.8 m): (a) Scenario 1. (b) Scenario 2. (c) Scenario 3. (d) Scenario 4. The dashed box indicates the occupied zone.

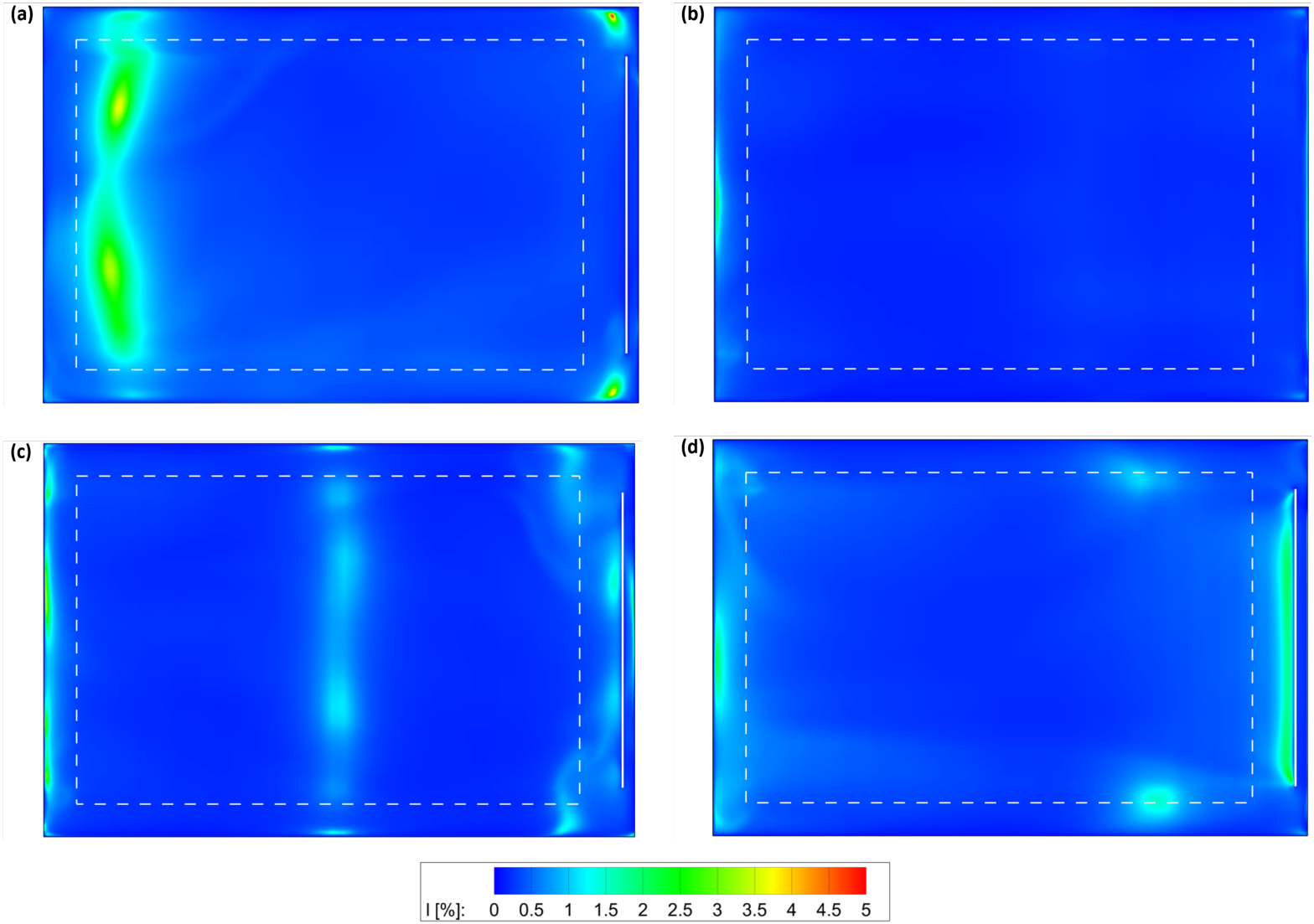

Figure 6.7: Turbulence intensity I (%) on the horizontal plane (i.e. y = 0.1 m): (a) Scenario 1. (b) Scenario 2. (c) Scenario 3. (d) Scenario 4. The dashed box indicates the occupied zone

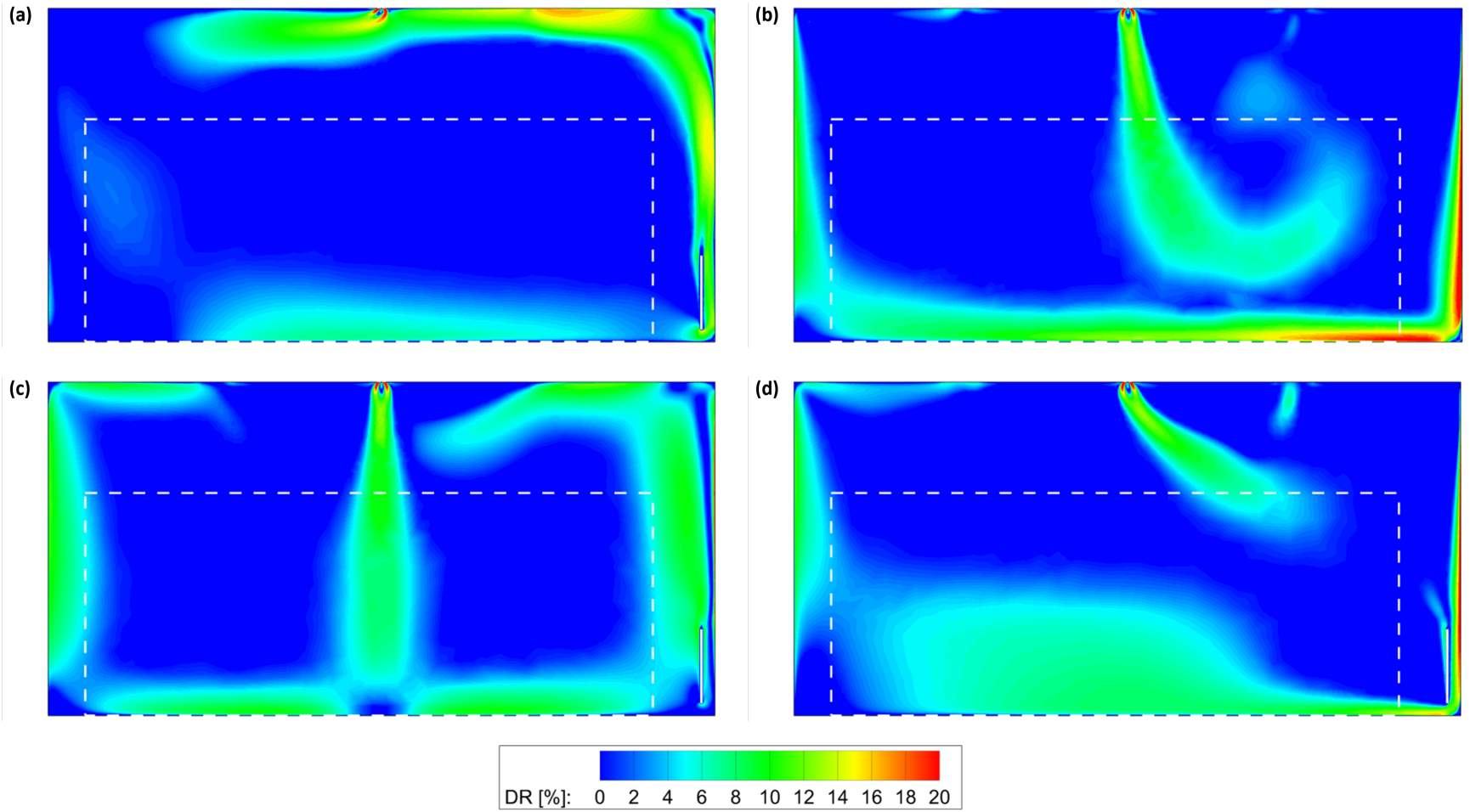

Figure 6.8: Draught rate DR (%) on the center plane (i.e. z = 1.8 m): (a) Scenario 1. (b) Scenario 2. (c) Scenario 3. (d) Scenario 4. The dashed box indicates the occupied zone.

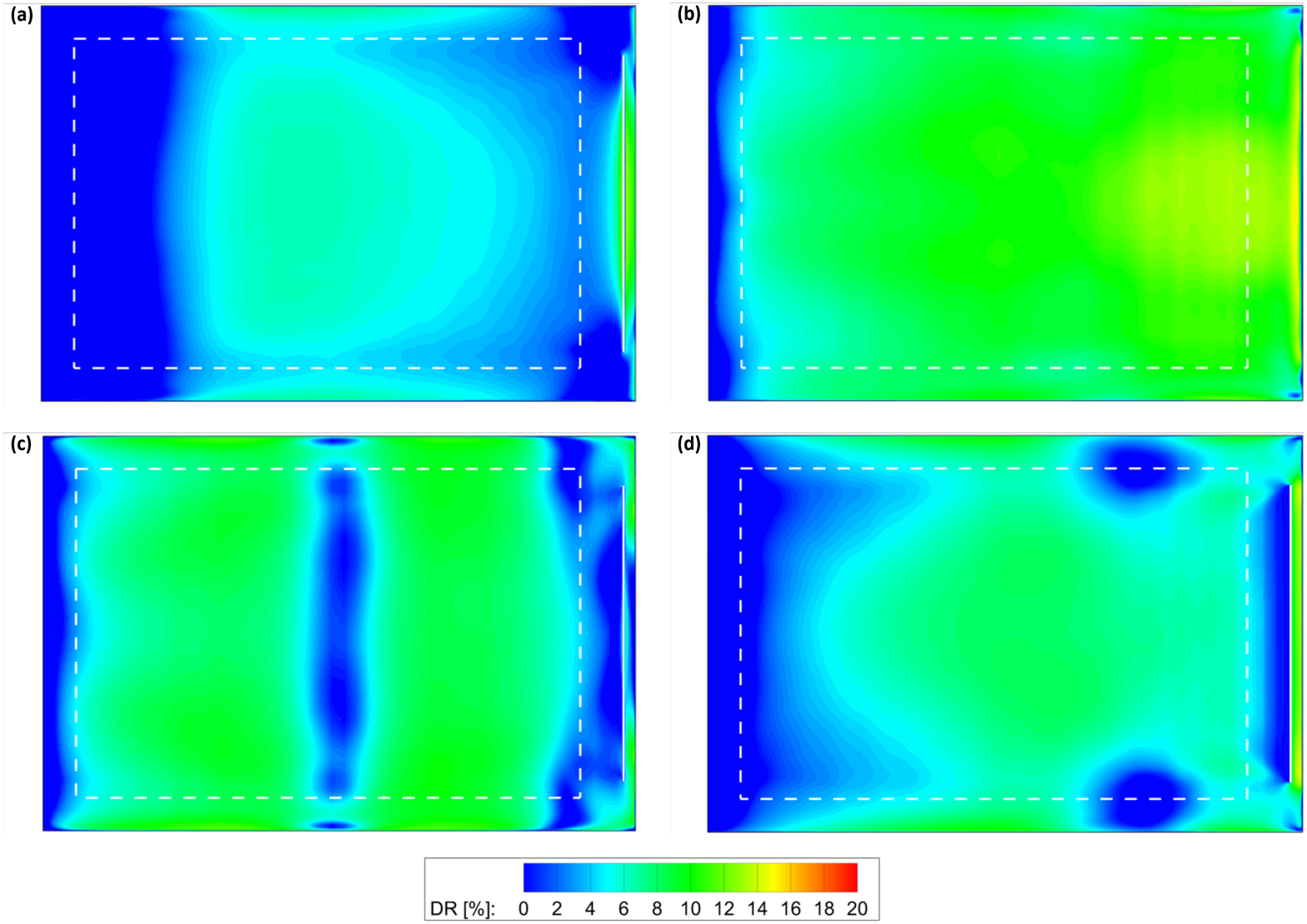

Figure 6.9: Draught rate DR (%) on the horizontal plane (i.e. y = 0.1 m): (a) Scenario 1. (b) Scenario 2. (c) Scenario 3. (d) Scenario 4. The dashed box indicates the occupied zone

6.1.5 Vertical temperature gradient

The temperatures for the ankle and head (seated person) level are examined in 20 points projected along two reference lines in the occupied zone (see Fig. 6.1). The largest gradient observed between two vertical points at the same position is summarized in Table 6.2. The temperature gradients $\Delta T_{a,v}$ are well below the requirements of a category B classification (i.e. < 3 °C) for all scenarios. The largest temperature gradient is found in Scenario 2 in which the downdraught on the facade generated a cold gravity current on the floor (see Fig. 6.2b).

Table 6.2: Vertical temperature gradient $\Delta T_{a,v}$ between ankle and head (seated person)

	Scenario 1	Scenario 2	Scenario 3	Scenario 4
T_a [°C]	21.89	20.44	22.39	21.28
T_v [°C]	22.04	21.57	22.06	21.71
$\Delta T_{a,v}$ [°C]	0.15	1.13	0.33	0.42

6.1.6 Floor temperature range

The area-weighted average floor temperature is summarized for each scenario in Table 6.3. Convective and radiative heat transfer within the enclosure were responsible for the floor temperature as the influence of adjacent enclosures was neglected due to an adiabatic assumption. The floor temperatures T_f are well in between the requirements of a category B classification (i.e. 19 to 29 °C).

Table 6.3: Area-weighted floor surface temperature T_f

	Scenario 1	Scenario 2	Scenario 3	Scenario 4
T_f [°C]	23.71	23.58	24.59	24.41

6.1.7 Operative temperature

The operative temperatures T_{op} are calculated as the average between the mean air temperature (T) and mean radiant temperature (MRT). ANSYS Fluent does not calculate the MRT as an output variable for the numerical simulations. A fictive point was therefore chosen to represent a seated person behind an office desk in a standardized layout to calculate MRT using Eq. (6.3):

$$MRT = T_1 F_{p-1} + T_2 F_{p-2} + ... + T_n F_{p-n} \tag{6.3}$$

where T_n is the temperature of surface n [°C] and F_{p-n} the angle factor between the fictive point and surface n [-]. The MRT calculated represented a single-point estimation within the enclosure based on a realistic situation. However, to conclude in a more precise way on the values of MRT multiple points need to be estimated. The values for T, MRT, and T_{op} for each scenario are summarized in Table 6.4.

Table 6.4: Overview of mean air temperature T, mean radiant temperature MRT, and operative temperature T_{op} in a fictive point

	Scenario 1	Scenario 2	Scenario 3	Scenario 4
T [°C]	22.00	21.42	21.98	21.59
MRT [°C]	22.63	20.49	22.58	22.12
T_{op} [°C]	22.32	20.96	22.28	21.86

The values of T for Scenario 2 and 4 are lower compared to other scenarios due to the influence of the generated downdraught on the facade as the counteracting thermal plume of the radiator is removed (i.e. Scenario 2) or less strong (i.e. Scenario 4). Also, the energy released by the climate ceiling accumulated near the ceiling and prevented a more mixed room air temperature. The MRT for Scenario 2 is much lower (i.e. ± 2 °C) compared to other scenarios due to the removal of the radiator. The calculation of Scenario 1, 3, and 4 assumes that a part of the opaque facade below the window has a surface temperature equal to that of the radiator (i.e. HTH = 70 °C, MTH = 45 °C, and LTH = 32.5 °C). However, in Scenario 2 the radiator is removed, and therefore the calculation assumes that the opaque facade has an interior surface temperature of 19.44 °C which causes the difference. Although the area-weighted average temperature of the ceiling in Scenario 2 is higher due to an increased climate ceiling surface, it does not compensate for the difference. The above-mentioned observations have resulted in similar differences in the T_{op} between the scenarios. Scenario 2 has the lowest T_{op} (i.e. 20.96 °C) which deviates from the other scenarios. Nevertheless, all scenarios have values of T_{op} well in between the requirement of a category B classification (i.e. 22 ± 2°C).

The difference in the values of T_{op} between the scenarios are considered to be acceptable for this research. The research is conducted to investigate the sole effect of different heating systems and their capacity on thermal comfort in a generic office model (i.e. similar model characteristics). Therefore, differences in T_{op} indicate whether the thermal comfort has decreased or increased compared to the initial Scenario 1 and if additional measures are required.

6.1.8 Predict mean vote

The whole-body thermal comfort index PMV is calculated in the specified fictive point (i.e. XYZ-coordinates (4.25, 1.10, 0.82). PMV is calculated according to the NEN-EN-ISO 7730 using Eq. (6.4):

$$PMV = \left[0.303 \cdot exp(-0.036 \cdot M) + 0.028\right] \cdot \left\{ \begin{array}{l} (M-W) - 3.05 \cdot 10^{-3} \cdot \left[5733 - 6.99 \cdot (M-W) - p_a\right] - 0.42 \cdot \left[M-W\right] - 58.15 \\ -1.7 \cdot 10^{-5} \cdot M \cdot (5867 - p_a) - 0.0014 \cdot M \cdot (34 - T) \\ -3.96 \cdot 10^{-8} \cdot f_{cl} \cdot \left[t_{cl} + 273)^4 - (MRT + 273)^4\right] - f_{cl} \cdot h_c \cdot (t_{cl} - T) \end{array} \right\} \tag{6.4}$$

where M is the metabolic rate (W/m^2), W the effective mechanical power (W/m^2, I_{cl} the clothing insulation (m^2· K/W), f_{cl} the clothing surface area factor (-), T the air temperature (°C), MRT the mean radiant temperature (°C), U the relative velocity (m/s), p_a the water vapour partial pressure (Pa), h_c the convective heat transfer coefficient (W/(m^2·K), and t_{cl} the clothing surface temperature (°C). The parameters t_{cl}, h_c, and f_{cl} are calculated using additional formulae according to the NEN-EN-ISO 7730 [23].

In the calculation of PMV, it is assumed that M has a value of 70 W/m^2 which represents a sedentary activity (i.e. office, school, etc.) and I_{cl} has a value of 0.11 (i.e. clo value of 0.7) which represents the typical combination of garments used within an office environment. The results of the parameters T, MRT, and U in the fictive point are summarized in Table 6.5

From Table 6.5, it is concluded that the perception of thermal comfort through the index PMV exceeds the threshold value of -0.5 < PMV < +0.5 for a category B classification in all scenarios. Scenario 1, 3, and 4 are considered to be perceived as *slightly cool* while Scenario 2 is perceived as *cool* according to the seven-point thermal sensation scale. Although the findings on behalf of PMV are presented in only one fictive point, it can be concluded that due to a decrease in T and MRT values accompanied with an increase in U for Scenario 2 has resulted in the decrease in thermal comfort.

Table 6.5: Overview of the PMV index and related variables T, MRT, and U

Parameter	Scenario 1	Scenario 2	Scenario 3	Scenario 4
T [°C]	22.00	21.42	21.98	21.59
MRT [°C]	22.63	20.49	22.58	22.12
U [m/s]	0.02	0.09	0.03	0.05
PMV	-0.9	-1.3	-0.9	-1.0

6.1.9 Intermediate conclusion

Thermal comfort is evaluated for all scenarios and the results of the individual parameters are summarized in Table 6.6. The values of the evaluation parameters which do not agree with the requirements of the category B classification are colored red. To obtain the category B classification , it is required to satisfy all individual parameters simultaneously [11].

From Table 6.6, it is concluded that Scenario 2 resulted in the largest decrease in thermal comfort compared to the initial Scenario 1. The velocity magnitude U increased due to the downdraught on the facade and resulted in a further penetration in the occupied zone (see Figs. 6.2a and 6.3a). The penetrating flow into the occupied zone increases the DR values up to a maximum value of 20.32 resulting from the combination of an increased U and decreased T. However, the maximum DR is only experienced in the first 0.5 m of the occupied zone underneath ankle level (i.e. 0.1 m). Also, the whole-body index PMV in the fictive point decreased significantly to the value of -1.3 (i.e. *cool* perception). The decrease in PMV is caused due to an increase in U and a decrease in T and MRT values compared to the initial Scenario 1.. Furthermore, the local discomfort parameters are well in between the requirements for a category B classification.

In Scenario 3, a similar thermal comfort with negligible differences was found compared to the initial Scenario 1. The DR increased slightly due to the thermal plume of the MTH radiator which altered the inlet flow (see Fig. 6.2c). However, the value for DR (i.e. 10.29) is well below the requirement for a category B classification. Furthermore, an increase floor temperature is measured compared to the initial Scenario 1. The value of T_f is increased due to the radiative heat transfer of the climate ceiling in combination with the heat transfer of the MTH radiator (i.e. convective and radiative) and the inflow pattern which causes a well-mixed room temperature. The local discomfort parameters are well in between the requirements for a category B classification.

In Scenario 4, the reduced capacity of the radiator causes the counteracting force to decrease further and provides conditions for downdraught to generate along the facade (see Fig. 6.2d). In combination with the decreased T of the downdraught, the DR values in the occupied zone increased to a maximum of 13.04. The increase in DR occurs in the first 0.2 m of the occupied zone near ankle level (i.e. 0.1 m) (see Fig. 6.8d). The above-mentioned differences in terms of U and T compared to the initial Scenario 1 caused the PMV to decrease slightly to a value of -1.0 (i.e. *slightly cool* perception). However, this decrease is quite small and provides a similar thermal sensation on the seven-point sensation scale as initial Scenario 1.

Table 6.6: Overview of the local thermal discomfort parameters [11]

Parameter	Category B	Scenario 1	Scenario 2	Scenario 3	Scenario 4
DR [%]	< 20	7.0	20.3	10.3	13.0
$T_{a,v}$ [°C]	< 3	0.2	1.1	0.3	0.4
T_f [°C]	19 - 29	23.7	23.6	24.6	24.4
T_{op} [°C]	22.0 ± 2.0	22.3	21.0	22.3	21.9
PMV	$-0.5 < \text{PMV} < +0.5$	-0.9	-1.3	-0.9	-1.0

Overall, it can be concluded that Scenario 3 and 4 provide similar comfort conditions compared to the initial Scenario 1. The increase in DR remains within the category B classification and the decrease in PMV for Scenario 4 is considered to be negligible. Therefore, these transition scenarios provide direct solutions for the generic office model to succeed in the implementation of LTH systems under the current model assumptions. In Scenario 2 the largest decrease in thermal comfort compared to the initial Scenario 1 is found and additional measures are required to provide similar comfort conditions. Also, Scenario 2 is a scenario that is desired in most retrofitting situations as the removal of the existing radiator provides additional space in the enclosure. Therefore, Scenario 2 will be subjected to an optimization study to provide an alternative for Scenario 1 in successfully transitioning towards an LTH system using a climate ceiling.

Two phenomena occur within Scenario 2 which create the uncomfortable conditions within the generic office model, namely the accumulation of heat under the ceiling which prevents a well-mixed room temperature, and the downdraught which penetrates the occupied zone. The accumulation of heat is experienced because of the inflow pattern which does not create a recirculation flow within the enclosure. The downdraught is generated because of the large temperature difference between the transparent facade element and the surrounding air. It is therefore decided to perform an optimization study in which first improvements to the installation concept (i.e. increased inflow velocity U_o or heat flux q of the climate ceiling) and its effects are simulated. Secondly, the thermal performance of the transparent facade element is increased to achieve smaller temperature gradients and monitor its effect on the downdraught.

7 — Optimization study

7.1 Optimization of installation concept

The optimization of the installation concept was examined through two modifications, namely increasing the inflow velocity (U_o) and increasing the heat flux (q) of the climate ceiling. In this way the effects of the individual modifications can be evaluated and provides insight into alternative solutions to improve the thermal comfort within the enclosure based on the installation concept. It also evaluates whether the results mentioned in Chapter 6 are the outcome of the specific installation assumptions defined in the generic office model for Scenario 2. The analysis was performed using similar computational settings and conditions mentioned in Chapter 5, except for the changes done in the optimization study.

The increase inflow velocity was chosen to investigate whether it would regenerate the Coanda-effect near the ceiling as seen in Appendix D. The Coanda-effect ensures that the accumulated heat underneath the ceiling is transferred more towards the occupied zone which increases the temperature distribution. The increase in inflow velocity was simulated in the generic office model in two ways:

- Decreasing the inlet surface area (A) from 0.063 to 0.037 m^2 by changing its length to keep the same flow rate (Q). The inlet was placed more towards the center of the enclosure, instead over the full width of the enclosure (Scenario V1);
- Increase the flow rate Q from 35 to 60 m^3/h per person, supplied through the inlet surface area (A) of 0.063 m^2 (Scenario V2).

Furthermore, increasing the heat flux from the climate ceiling was chosen to investigate whether the accumulated heat underneath the ceiling changed to a more well-mixed room temperature, and could affect the temperature gradient between the transparent facade element and the surrounding air. The heat flux from the climate ceiling was increased by 20% from 60.13 to 72.16 W/m^2 in the optimization scenario in which the sole effect of an increased flux was examined. This resulted in a slight increase of the surface temperature (i.e. 36.67 °C) compared to the average temperature of an LTH system (i.e. LTH = 32.5 °C).

7.1.1 Results

The optimization Scenario V1 (i.e. Velocity 1), V2 (i.e. Velocity 2), and F1 (i.e. Flux 1) are evaluated using the parameters U, T, I, and DR to evaluated trends between the results of the case study (see Chapter 6). The local discomfort parameters $\Delta T_{a,v}$, T_f and the parameters PMV and T_{op} were not considered within this part of the optimization study as the trends are considered to be sufficient in indicating whether the modifications in the installation concept would increase the thermal comfort of Scenario 2.

Mean velocity magnitude

In Scenario V1, the decreased inlet area resulted in a perpendicular jet-type flow penetrating the occupied zone under the influence of an increased inflow velocity (see Fig. 7.1b). The downdraught on the facade, however, was partially counteracted in the region by the jet-type flow as seen in Figure 7.2b). Despite the increase in velocity, the downdraught still contributes to discomfort within the occupied zone.

In Scenario V2, the increased inflow velocity resulted in the regeneration of the Coanda-effect on the ceiling which creates an inflow pattern towards both sides of the enclosure (see Fig. 7.1c). The momentum of the downdraught on the facade causes the flow to penetrate the occupied zone and move upward on the back wall of the enclosure. The recirculation generated by the downdraught is eventually altered by the left inflow jet and redirected from underneath the ceiling towards the occupied zone. Furthermore, the right inflow jet contributes to the downdraught as the flow assists the downdraught (see Fig. 7.1c).

In Scenario F1, the thickness of the downdraught on the facade has decreased (see Fig. 7.1d). However, the penetration in the occupied zone occurred further into the occupied zone as was seen in Figure 7.2d. Indicating that despite the increased energy output, the temperature gradient near the facade holds.

Mean air temperature

In Scenario V1, under the influence of the jet-type flow, the conditioned air (i.e. 18 °C) affects the temperature gradient in the enclosure very strongly. The effect of the climate ceiling was largely removed and in combination with the cold downdraught resulted in much colder conditions than in the initial Scenario 2 (see Figs. 7.3b and 7.4b).

In Scenario V2, a similar phenomenon was experienced as in Scenario V1. The increased velocity causes the conditioned air to spread further into the enclosure under the influence of the Coanda-effect and becomes dominant over the climate ceiling in conditioning the air temperature (see Figs. 7.3c and 7.4c). The condition air is redirected towards the occupied zone at some distance from the inlet region. Therefore, it prevents the climate ceiling to release its energy and causes the low uniform air temperature in the enclosure. The perceived conditions could be changed by increasing the temperature of the conditioned air (i.e. > 18 °C).

In Scenario F1, the increase in the energy output of the climate ceiling caused a significant increase in air temperature throughout the enclosure. In the other scenarios, the energy released from the climate ceiling accumulated near the ceiling instead of creating a more uniform distribution. However, the temperature gradient near the facade still holds and causes downdraught which penetrates the occupied zone.

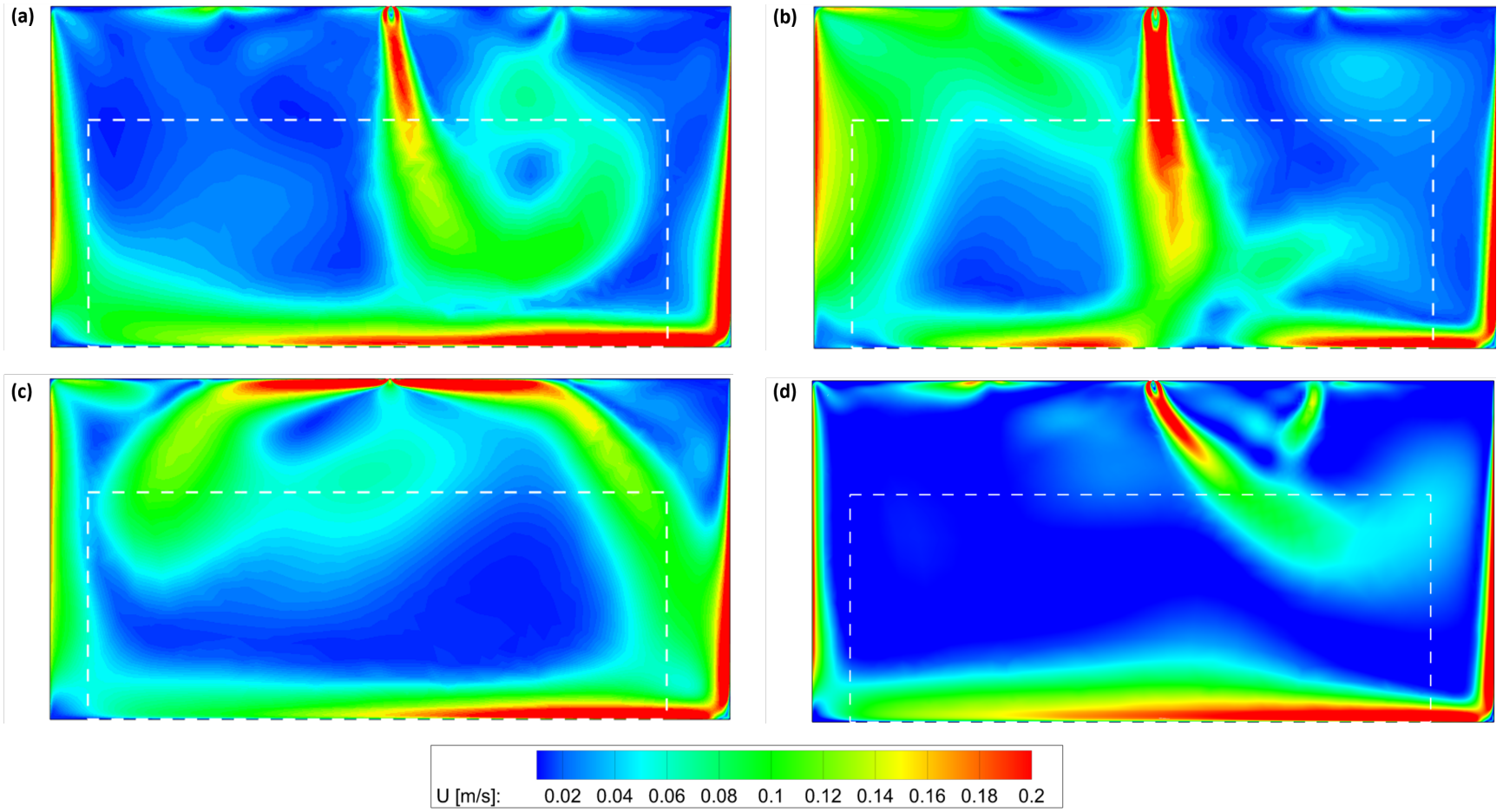

Figure 7.1: Mean velocity magnitude U (m/s) on the center plane (i.e. z = 1.8 m): (a) Scenario 2. (b) Scenario V1. (c) Scenario V2. (d) Scenario F1. The dashed box indicates the occupied zone

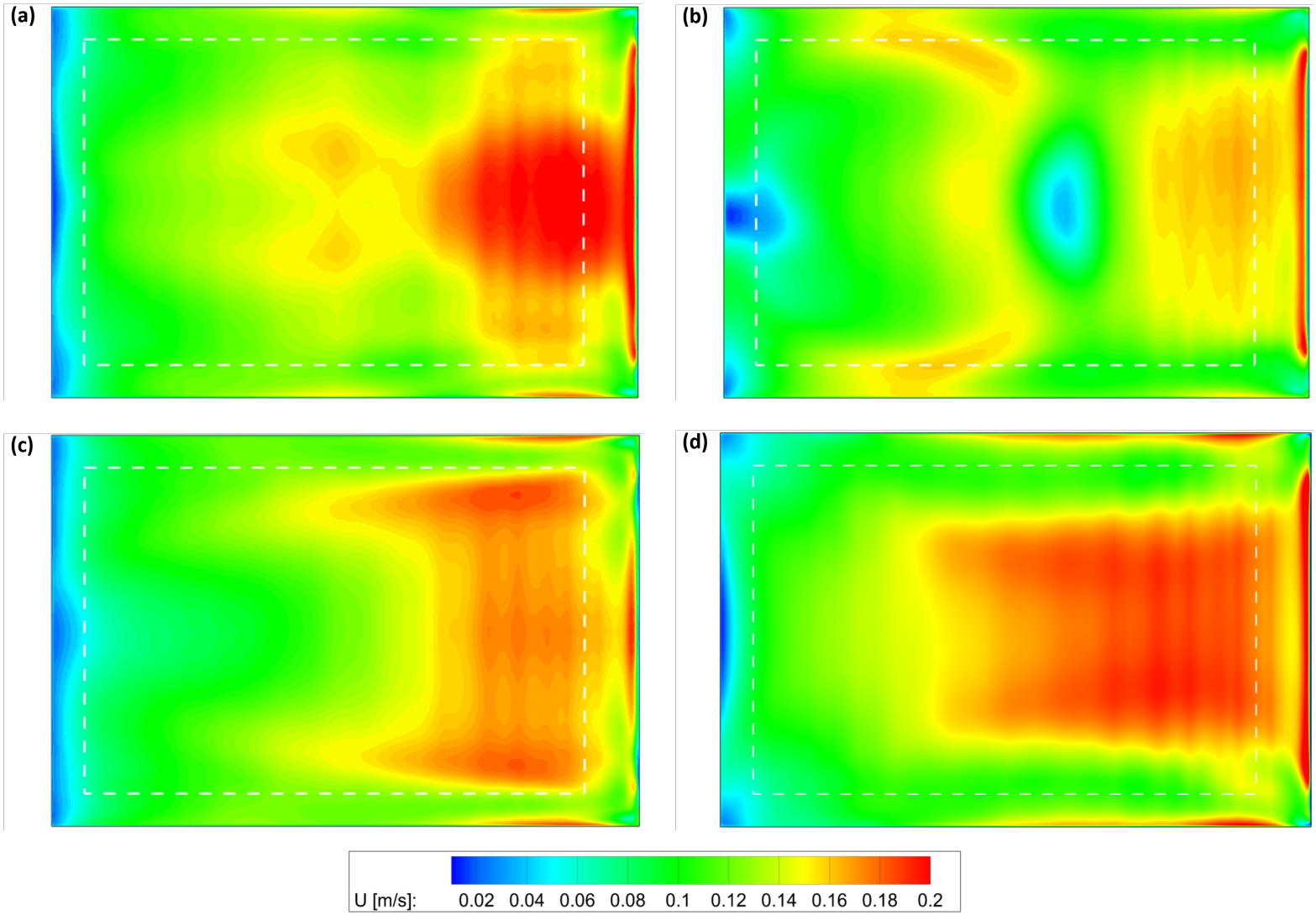

Figure 7.2: Mean velocity magnitude U (m/s) on the horizontal plane (i.e. y = 0.1 m): (a) Scenario 2. (b) Scenario V1 (c) Scenario V2. (d) Scenario F1. The dashed box indicates the occupied zone

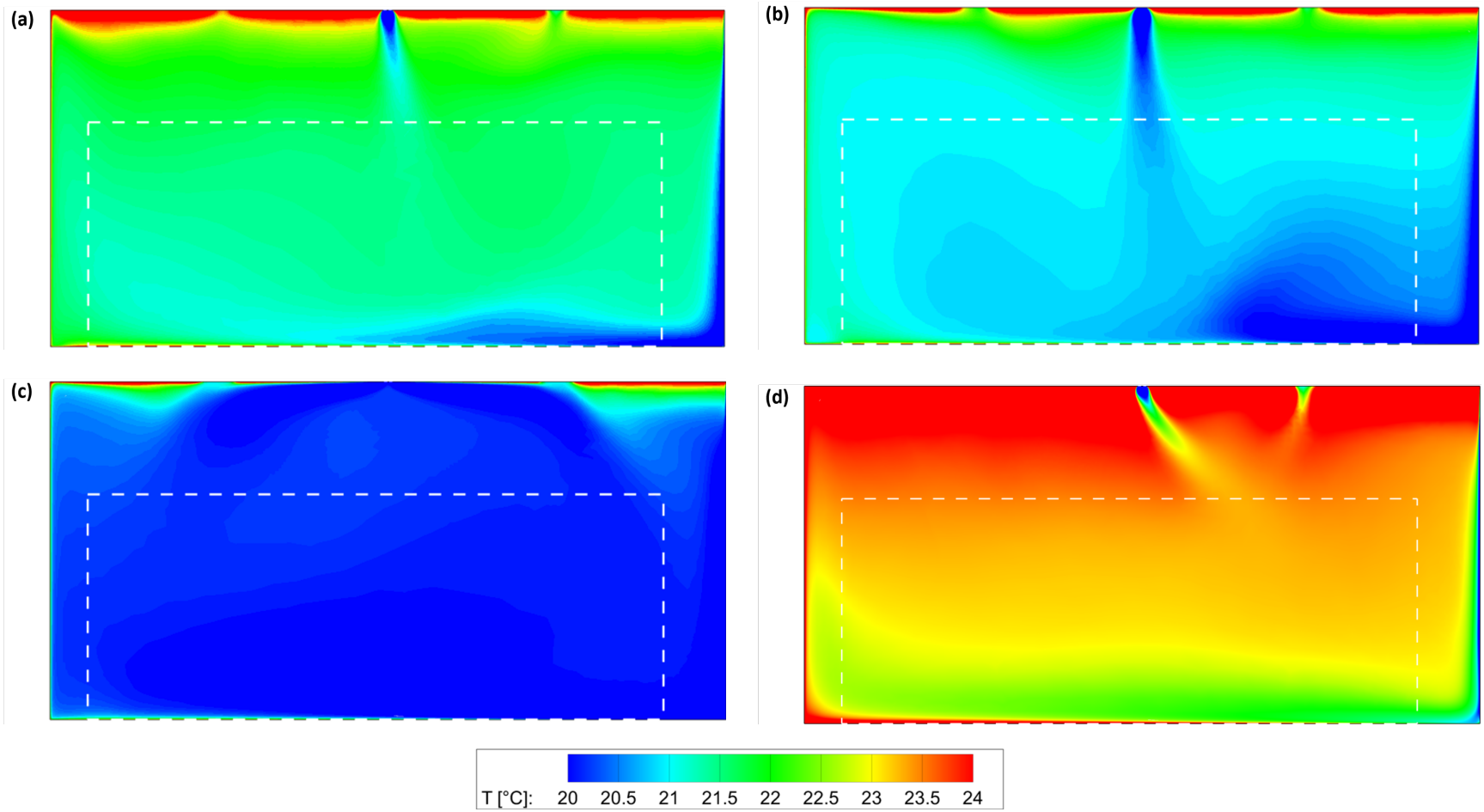

Figure 7.3: Mean air temperature T (°C) on the center plane (i.e. z = 1.8 m): (a) Scenario 2. (b) Scenario V1. (c) Scenario V2. (d) Scenario F1. The dashed box indicates the occupied zone

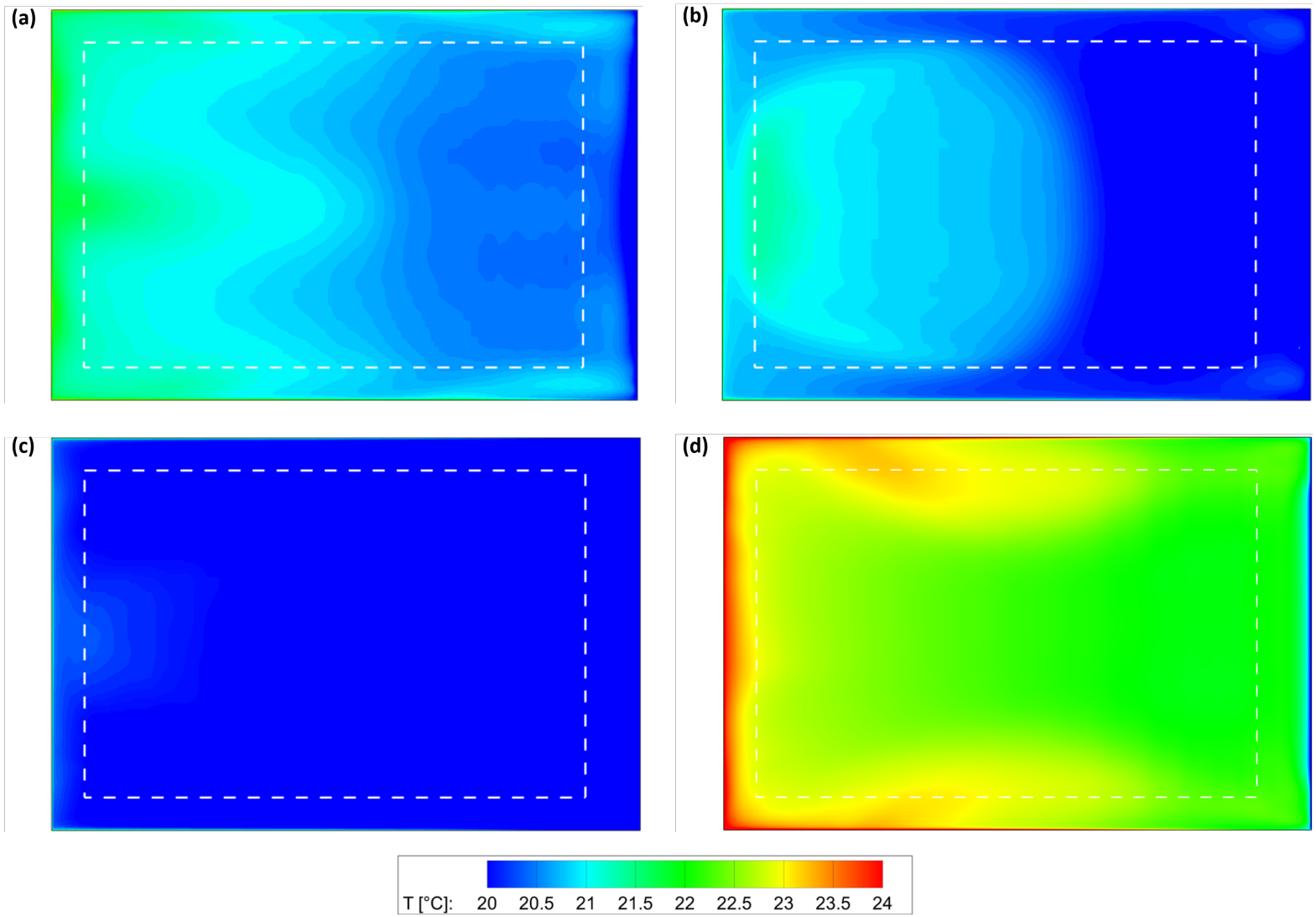

Figure 7.4: Mean air temperature T (°C) on the horizontal plane (i.e. y = 0.1 m): (a) Scenario 2. (b) Scenario V1. (c) Scenario V2. (d) Scenario F1. The dashed box indicates the occupied zone

Turbulence intensity

The results of I are displayed in Figures 7.5 and 7.6. The values for I were mainly below 5 % within the occupied zone and displayed some small regions of higher values.

Draught rate

In Scenario V1, the jet-type flow penetrating the occupied zone counteracted the downdraught slightly and resulted in lower DR values on the facade and at the beginning of the occupied zone (see Figs. 7.7b and 7.8b).

In Scenario V2, the regenerated Coanda effect from the linear slot diffuser decreased U on the facade and near the floor region. However, due to the dominant conditioned air supply, a low value of T caused the high values of DR on the facade and in the occupied zone (see Figs. 7.7c and 7.8c).

In Scenario F1, the decreased temperature gradient in the enclosure caused significantly lower DR values on the facade and at the beginning of the occupied zone compared to the other optimization scenarios.

7.1.2 Intermediate conclusion

It can be concluded that under the influence of an increased inflow velocity or an increased heat flux of the climate ceiling the conditions within the generic office model changed significantly. In Scenario V1, the increased inflow velocity resulted in cooler air temperatures within the occupied zone and decreased the effect of downdraught due to the altered inflow pattern (i.e. perpendicular to the ceiling). In Scenario V2, the Coanda effect on the ceiling did not result in the desired effect as the heat flux from the climate ceiling is suppressed due to the inflow conditions instead of mixed resulting in a more comfortable room temperature. In Scenario F1, the increased heat flux from the climate ceiling results in a comfortable temperature gradient in the occupied zone. However, the downdraught on the facade which penetrates the occupied zone is observed and affects the thermal comfort. Additional research is needed to provide comfortable indoor conditions within the optimization Scenario V1, V2, and F1 as it can be concluded that improving the installation concept requires more specification (i.e. inflow conditions, positioning of inflow, etc.).

In addition to the performed optimization study, it was evaluated whether retrofitting the transparent facade element can improve the indoor conditions compared to adjusting the installation concept. The thermal performance of the transparent facade element in the generic office model is considered to be intermediate (U-factor = 4.1 (W/m^2·K)). Scenario 2 will therefore be subjected to an optimization study in which the combination of the climate ceiling concept and improved transparent facade element is evaluated.

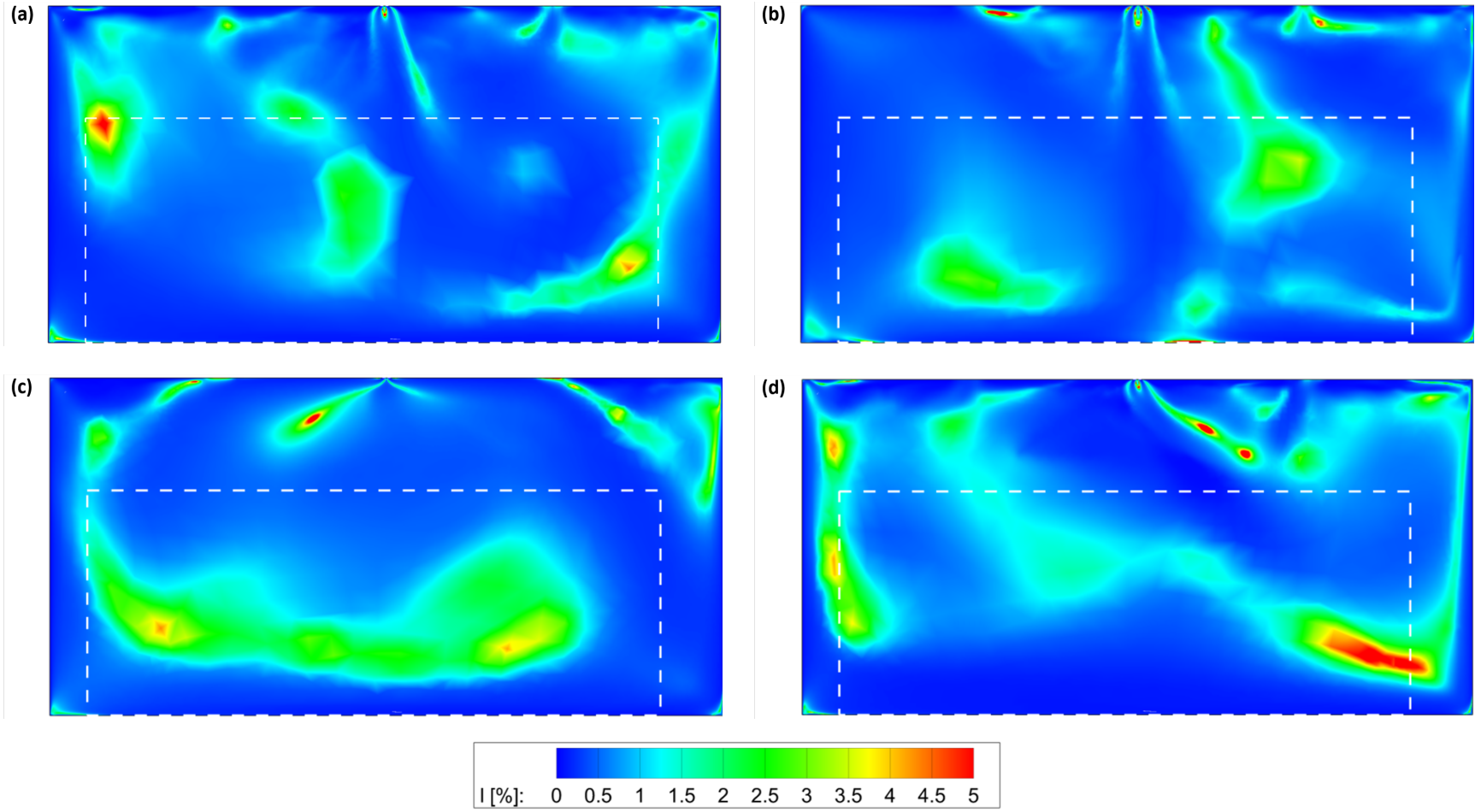

Figure 7.5: Turbulence intensity I (%) on the center plane (i.e. z = 1.8 m): (a) Scenario 2. (b) Scenario V1. (c) Scenario V2. (d) Scenario F1. The dashed box indicates the occupied zone

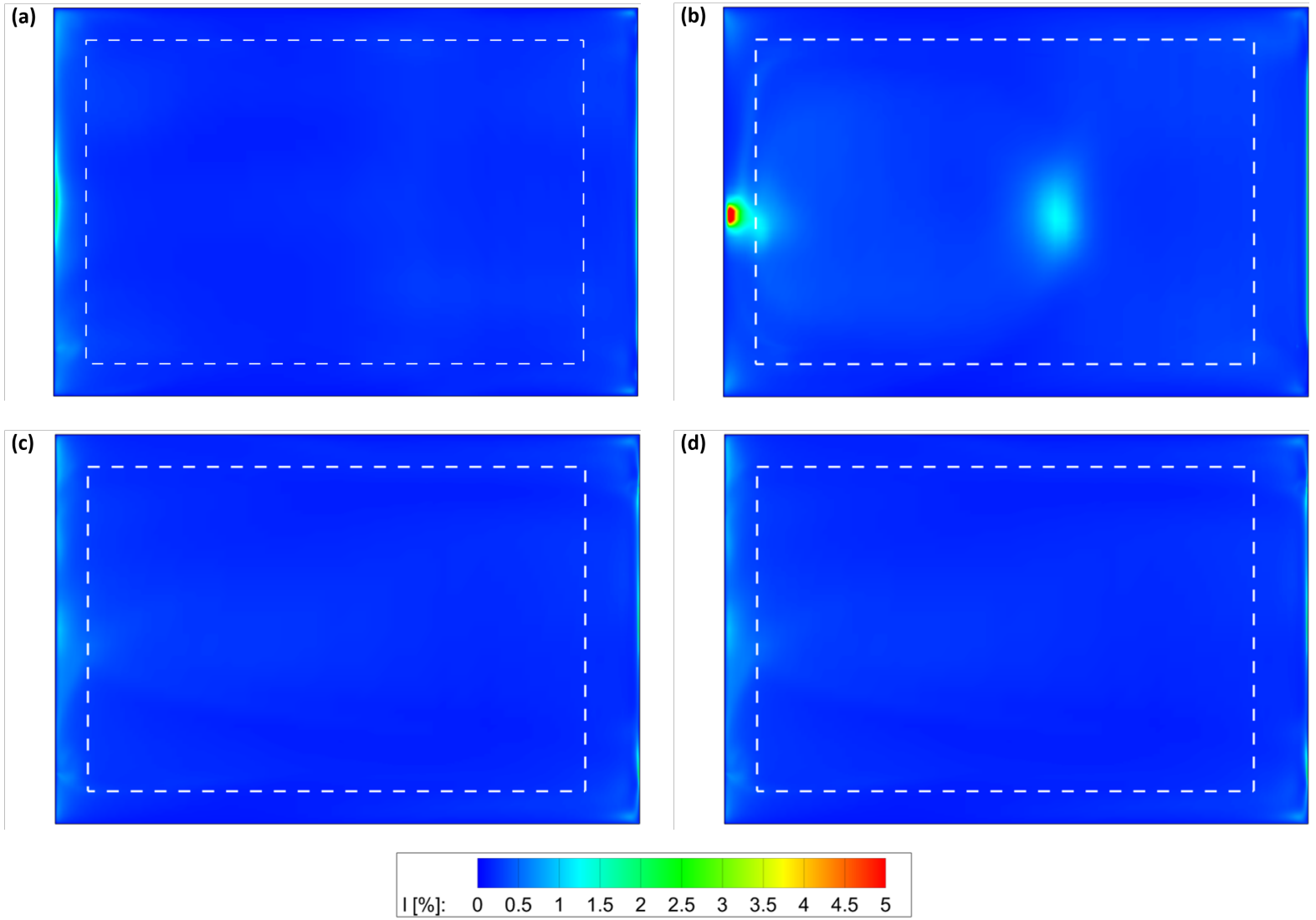

Figure 7.6: Turbulence intensity I (%) on the horizontal plane (i.e. y = 0.1 m): (a) Scenario 2. (b) Scenario V1. (c) Scenario V2. (d) Scenario F1. The dashed box indicates the occupied zone

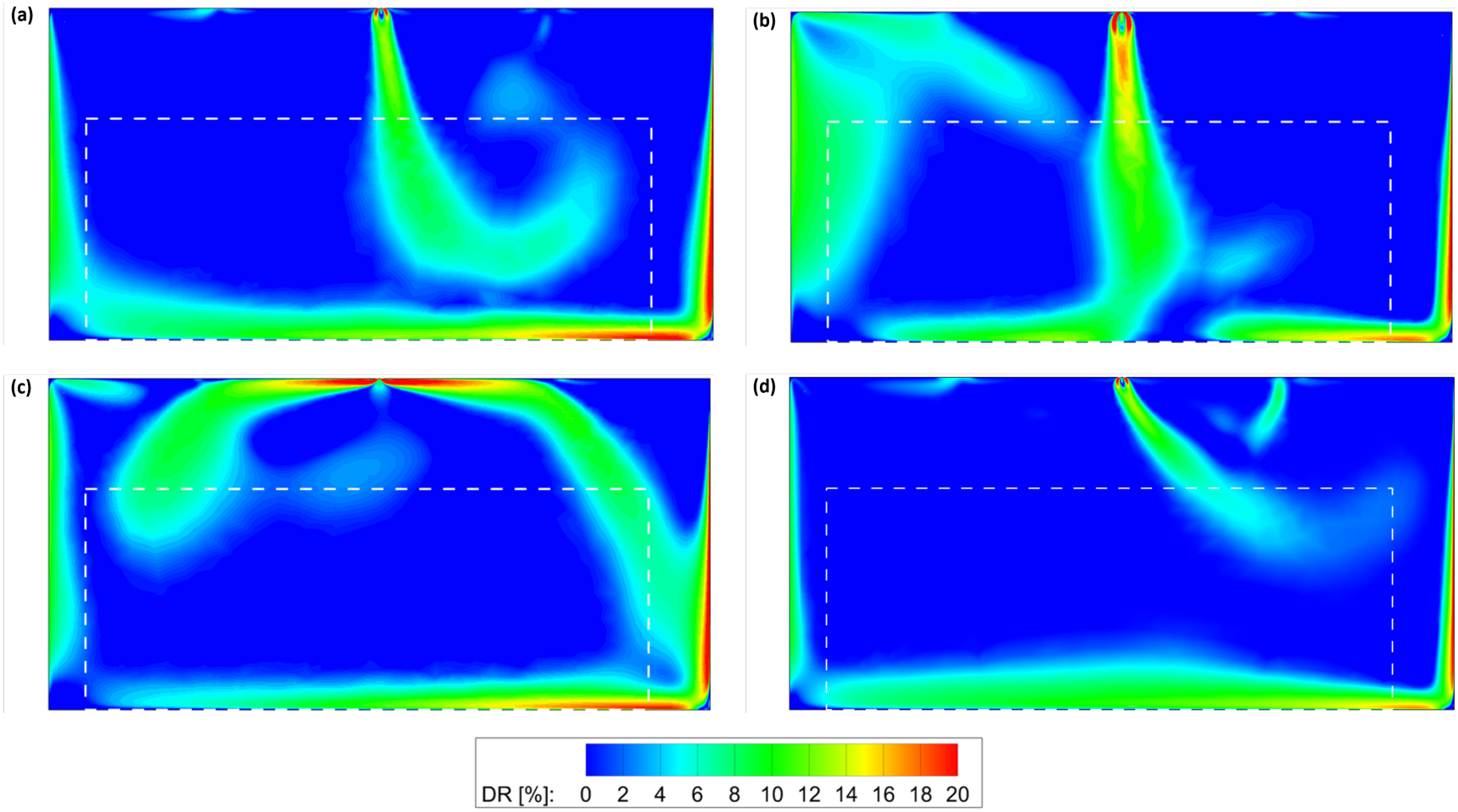

Figure 7.7: Draught rate DR (%) on the center plane (i.e. z = 1.8 m): (a) Scenario 2. (b) Scenario V1. (c) Scenario V2. (d) Scenario F1. The dashed box indicates the occupied zone

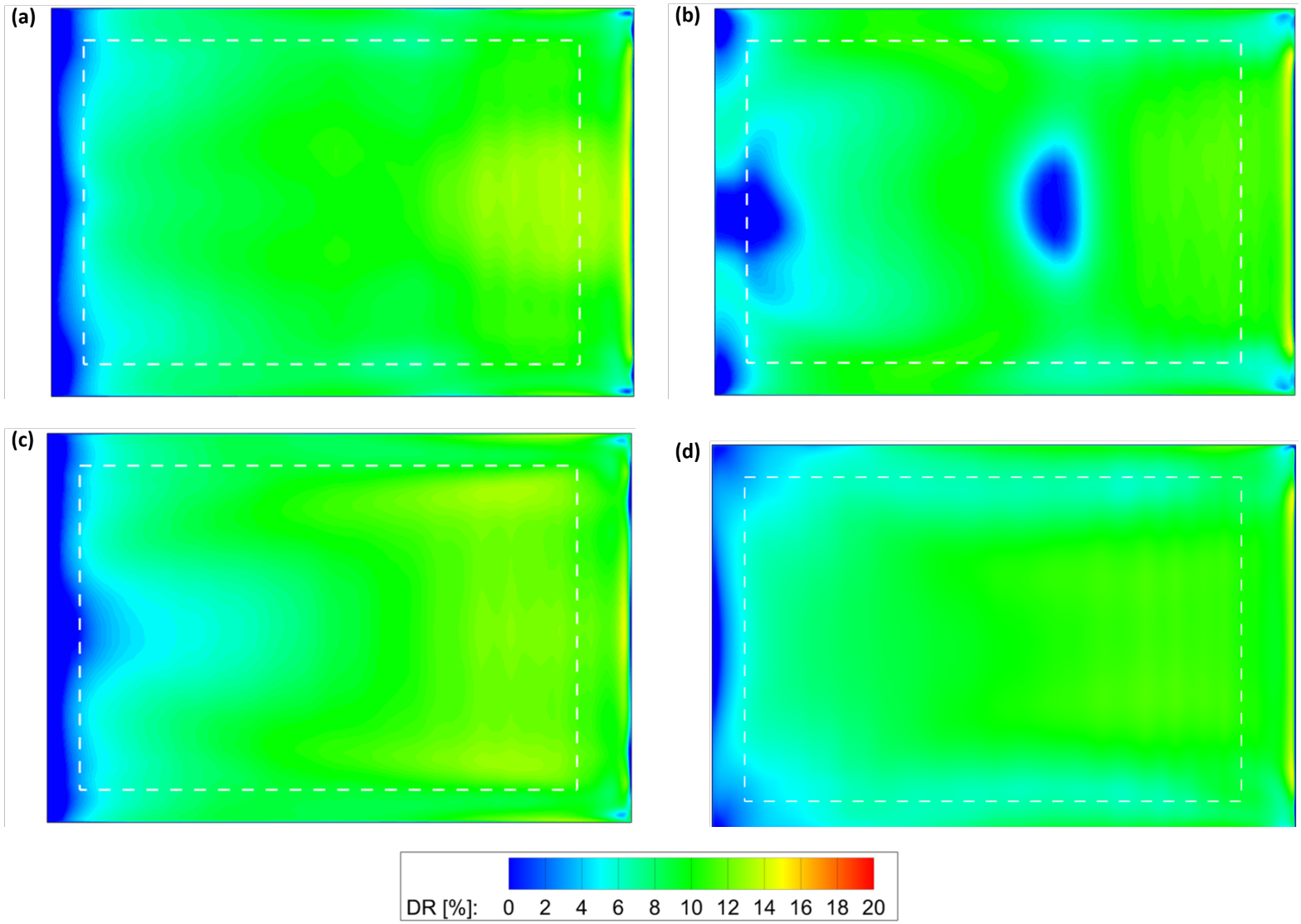

Figure 7.8: Draught rate DR (%) on the horizontal plane (i.e. y = 0.1 m): (a) Scenario 2. (b) Scenario V1. (c) Scenario V2. (d) Scenario F1. The dashed box indicates the occupied zone

7.2 Optimization of transparent facade element

The improvement of the thermal performance of the facade element was achieved by replacing the existing construction (i.e. double glass in a metal frame that is not thermally interrupted: U-factor = 4.1 W/m^2·K) for an improved construction. Two improved constructions are simulated: combined window constructions of (i) HR++ glass in a wooden frame (U-factor = 1.64 W/m^2·K) (i.e. Scenario 2a) and (ii) triple glazing in a wooden frame (U-factor = 1.07 W/m^2·K) (i.e. Scenario 2b). The improvement of HR++ glass in a wooden frame was chosen as it meets the regulations formulated in the Building Decree for newly built buildings (i.e. U-factor = 1.65 W/m^2·K) [50]. The fixed surface temperature on the interior of the transparent facade element was calculated with the use of Eq. (5.1) and resulted in surface temperatures of 15.45 and 17.36 °C for the combined window construction of HR++ and triple glass, respectively (see Appendix B). Furthermore, similar boundary conditions and solver settings were applied as mentioned in Sections 5.1.3 and 5.1.4 for Scenario 2.

7.2.1 Results

The optimization Scenario 2a and 2b are evaluated using the same parameters as mentioned in Section 6.1, namely parameters U, T, I, and DR, the local discomfort parameters $\Delta T_{a,v}$, T_f, and the additional parameters T_{op} and PMV.

Mean velocity magnitude

The results of U for the optimized Scenario 2a and 2b are compared and visualized with the results of Scenario 2 in Figures 7.9 and 7.10. Furthermore, the velocity vectors and streamlines for both scenarios are presented in Appendix E. The interior surface temperature of the transparent facade element increased from 7.15 to 15.45 °C (i.e. Scenario 2a) and 17.36 °C (i.e. Scenario 2b) and resulted in a smaller temperature gradient between the facade and parallel fluid layer. The smaller temperature gradient decreases the counteracting forces compared to Scenario 2 and therefore lower velocities (U) are observed along the facade and in the occupied zone (see Figs. 7.9 and 7.10). Also, the observed gravity current in Scenario 2 which causes the extensive penetration of the downdraught in the occupied zone is reduced as the density differences between the optimized Scenario 2a and 2b and the surrounding air are lowered. The largest decrease of U is observed for Scenario 2b as the smallest temperature gradient was observed.

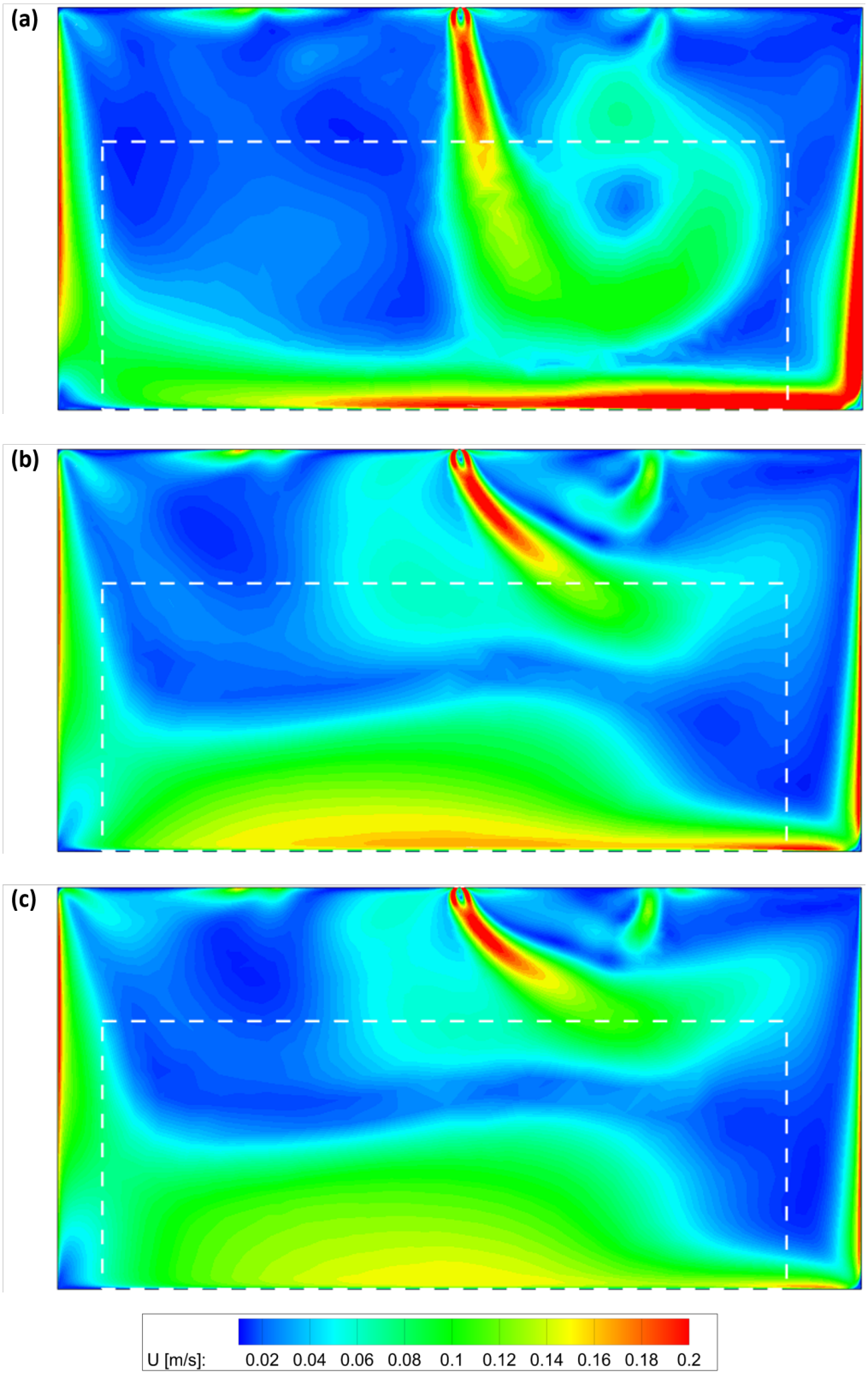

Figure 7.9: Mean velocity magnitude U (m/s) on the center plane (i.e. z = 1.8 m): (a) Scenario 2 (U-factor = 4.1 W/m^2·K). (b) Scenario 2a (U-factor = 1.64 W/m^2·K). (c) Scenario 2b (U-factor = 1.07 W/m^2·K). The dashed box indicates the occupied zone

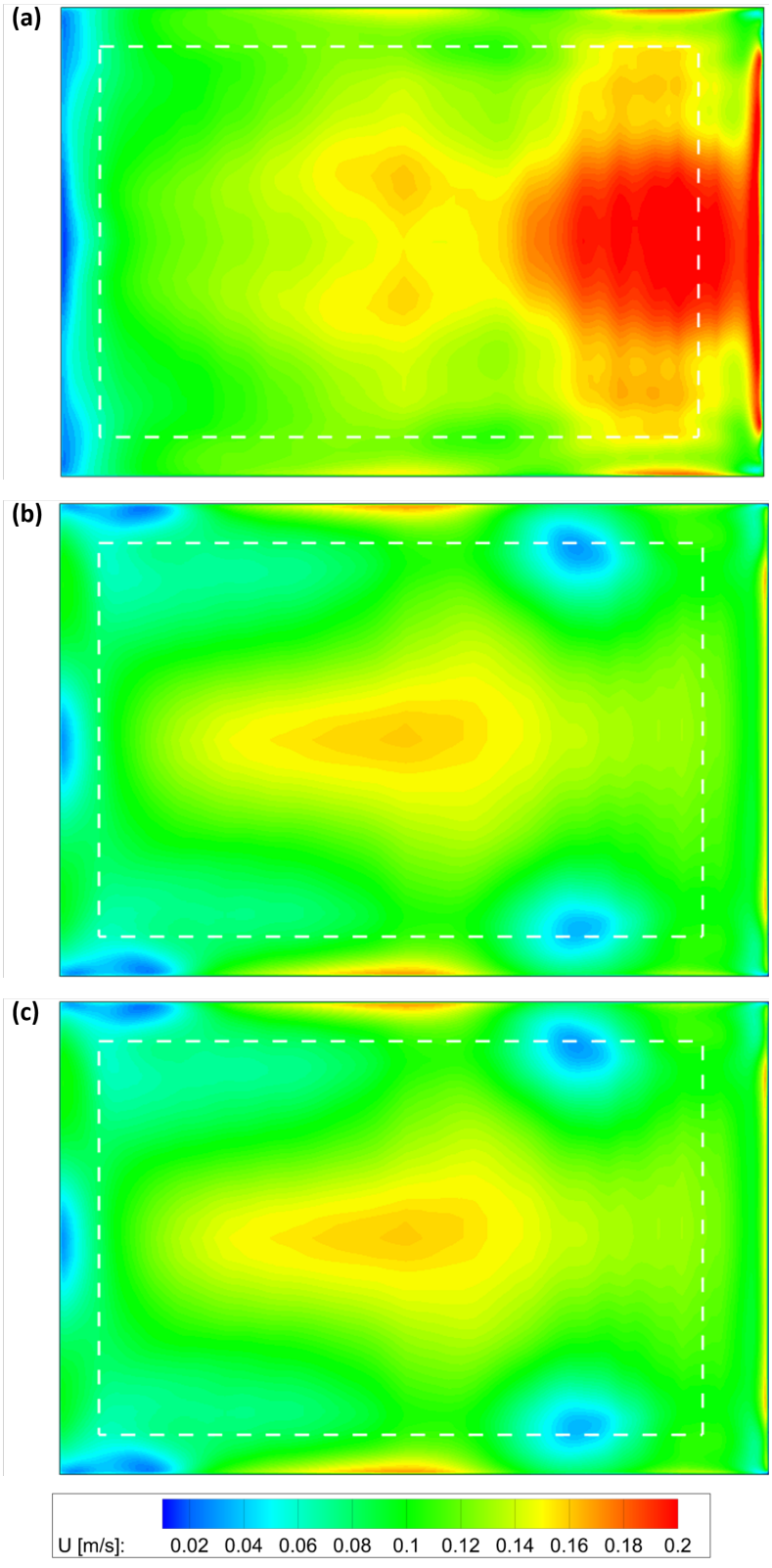

Figure 7.10: Mean velocity magnitude U (m/s) on the horizontal plane (i.e. y = 0.1 m): (a) Scenario 2 (U-factor = 4.1 W/m^2·K). (b) Scenario 2a (U-factor = 1.64 W/m^2·K). (c) Scenario 2b (U-factor = 1.07 W/m^2·K). The dashed box indicates the occupied zone

Mean air temperature

The results of T for the optimized Scenario 2a and 2b are compared and visualized with the results of Scenario 2 in Figures 7.11 and 7.12. The air temperature of the downdraught along the facade decreased significantly due to the decreased temperature gradient between the transparent facade element and the surrounding air. Therefore, the airflow penetrating the occupied zone has a higher T and provides a well-mixed room temperature (see Figs. 7.11 and 7.12. It is also noticed that the accumulated region of heat from the climate ceiling has grown compared to Scenario 2 because the small circulation flow originating from the downdraught towards the back wall decreased. Therefore, the interaction between the region underneath the climate ceiling and the circulation flow decreased, prevents mixing, and results in the accumulation.

Overall, the differences in T between Scenario 2a and 2b were small and displayed similar patterns. Therefore, in terms of T a further increase of thermal performance of the transparent facade elements is not required.

Turbulence intensity

The results of I for the optimized Scenario 2a and 2b are compared and visualized with the results of Scenario 2 in Figures 7.13 and 7.14. Although the values for I are mainly below 5% within the occupied zone, the optimized Scenario 2a and 2b show a local increase following a similar pattern.

Draught rate

The results of DR for the optimized Scenario 2a and 2b are compared and visualized with the results of Scenario 2 in Figures 7.15 and 7.16. The optimized Scenario 2a and 2b display significantly lower DR values as a result of the decreased velocity U and increased T on the facade and within the occupied zone. An improvement is achieved compared to Scenario 2 by increasing the thermal performance of the transparent facade element.

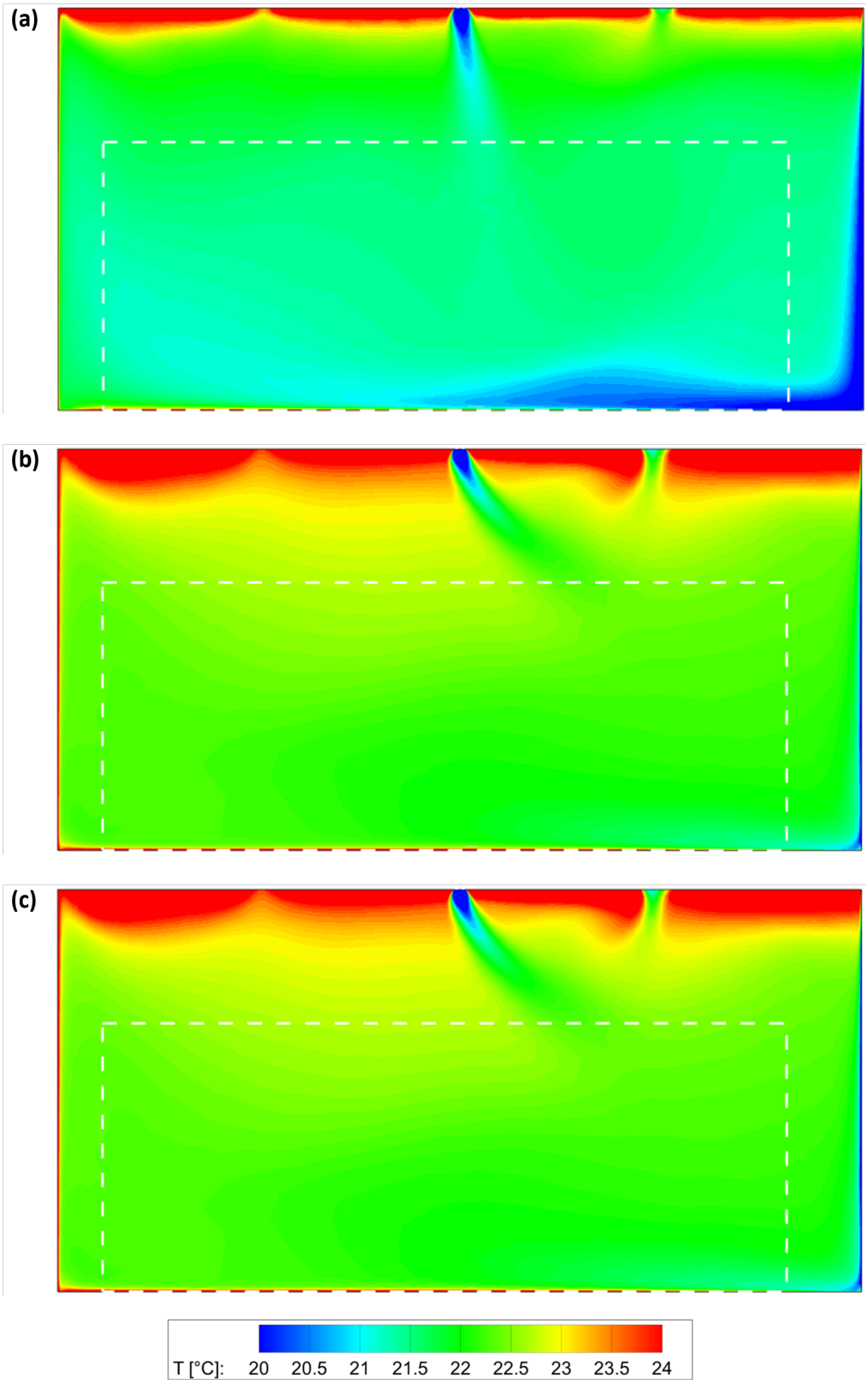

Figure 7.11: Mean air temperature T (°C) on the center plane (i.e. z = 1.8 m): (a) Scenario 2 (U-factor = 4.1 W/m^2·K). (b) Scenario 2a (U-factor = 1.64 W/m^2·K). (c) Scenario 2b (U-factor = 1.07 W/m^2·K). The dashed box indicates the occupied zone

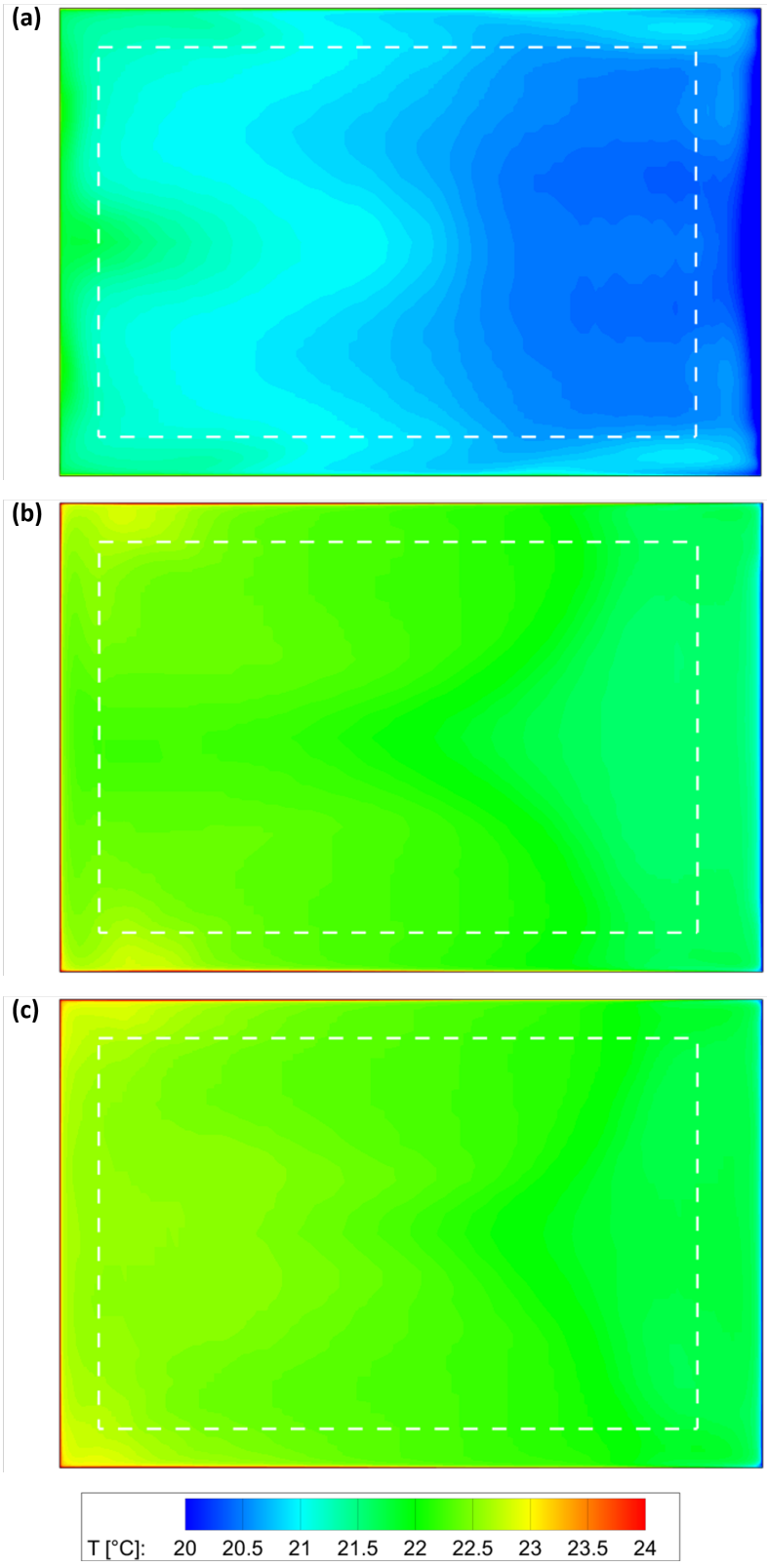

Figure 7.12: Mean air temperature T (°C) on the horizontal plane (i.e. y = 0.1 m): (a) Scenario 2 (U-factor = 4.1 W/m^2·K). (b) Scenario 2a (U-factor = 1.64 W/m^2·K). (c) Scenario 2b (U-factor = 1.07 W/m^2·K). The dashed box indicates the occupied zone

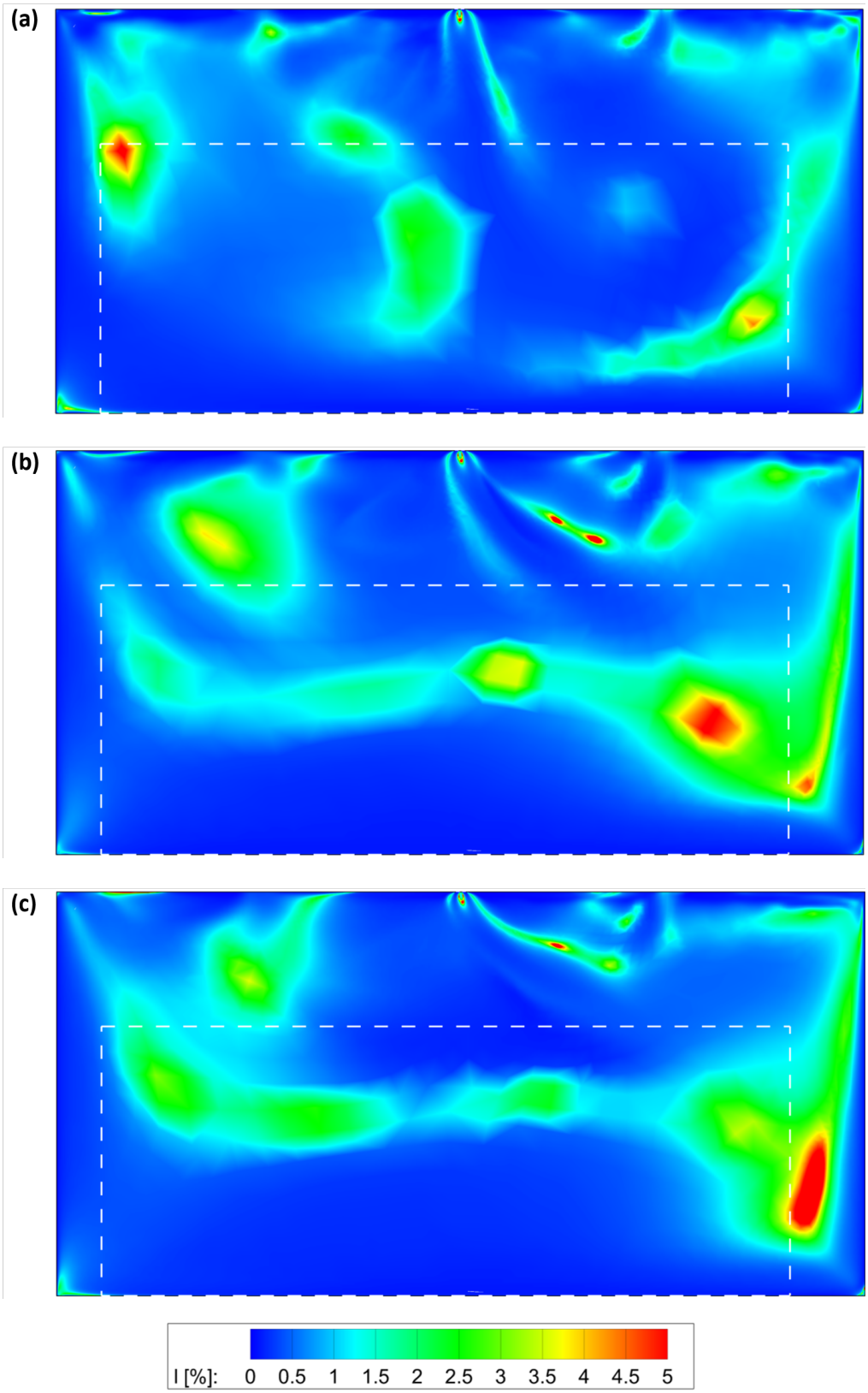

Figure 7.13: Turbulence intensity I (%) on the center plane (i.e. z = 1.8 m): (a) Scenario 2 (U-factor = 4.1 W/m^2·K). (b) Scenario 2a (U-factor = 1.64 W/m^2·K). (c) Scenario 2b (U-factor = 1.07 W/m^2·K). The dashed box indicates the occupied zone

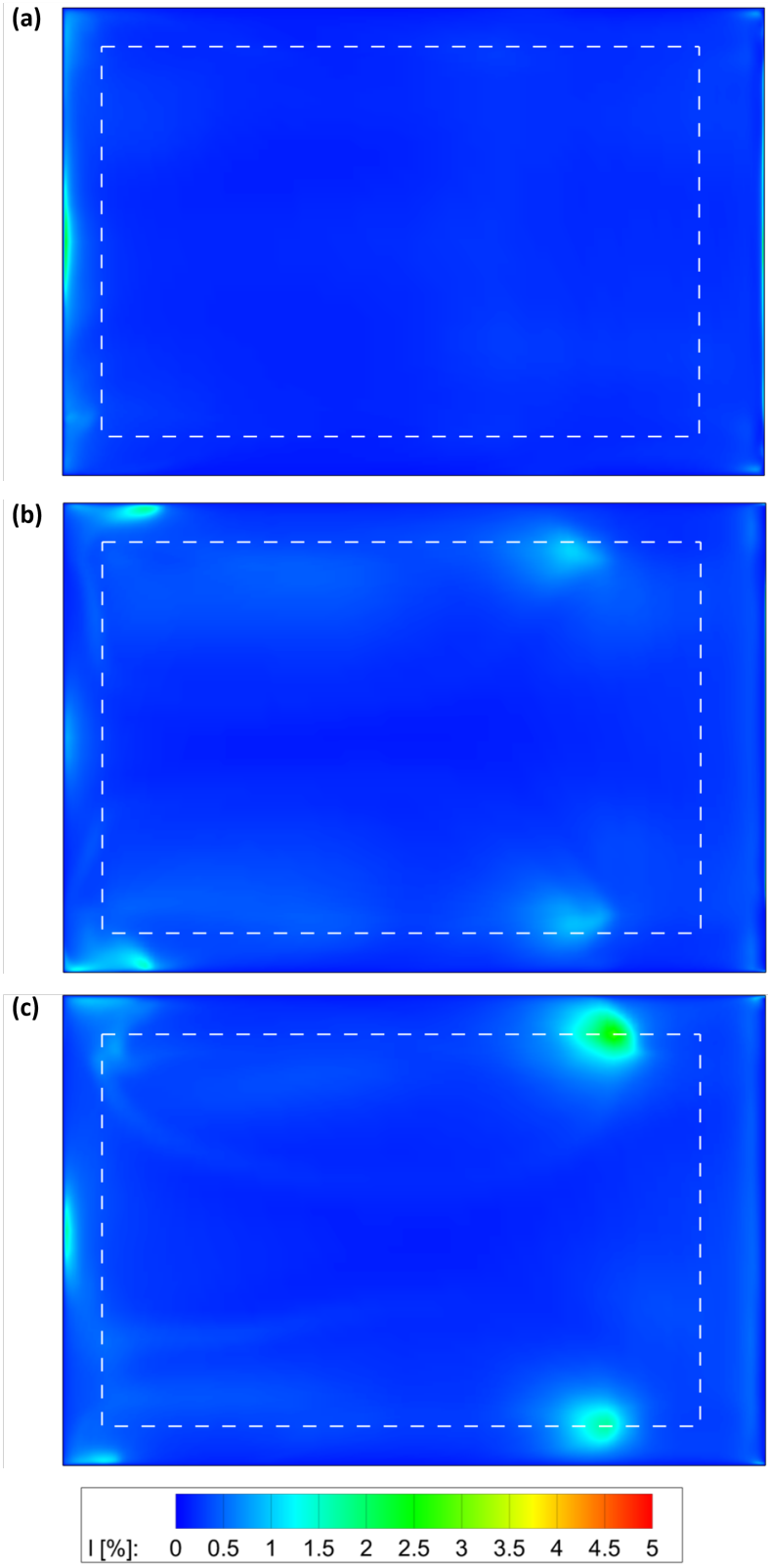

Figure 7.14: Turbulence intensity I (%) on the horizontal plane (i.e. y = 0.1 m): (a) Scenario 2 (U-factor = 4.1 W/m^2·K). (b) Scenario 2a (U-factor = 1.64 W/m^2·K). (c) Scenario 2b (U-factor = 1.07 W/m^2·K). The dashed box indicates the occupied zone

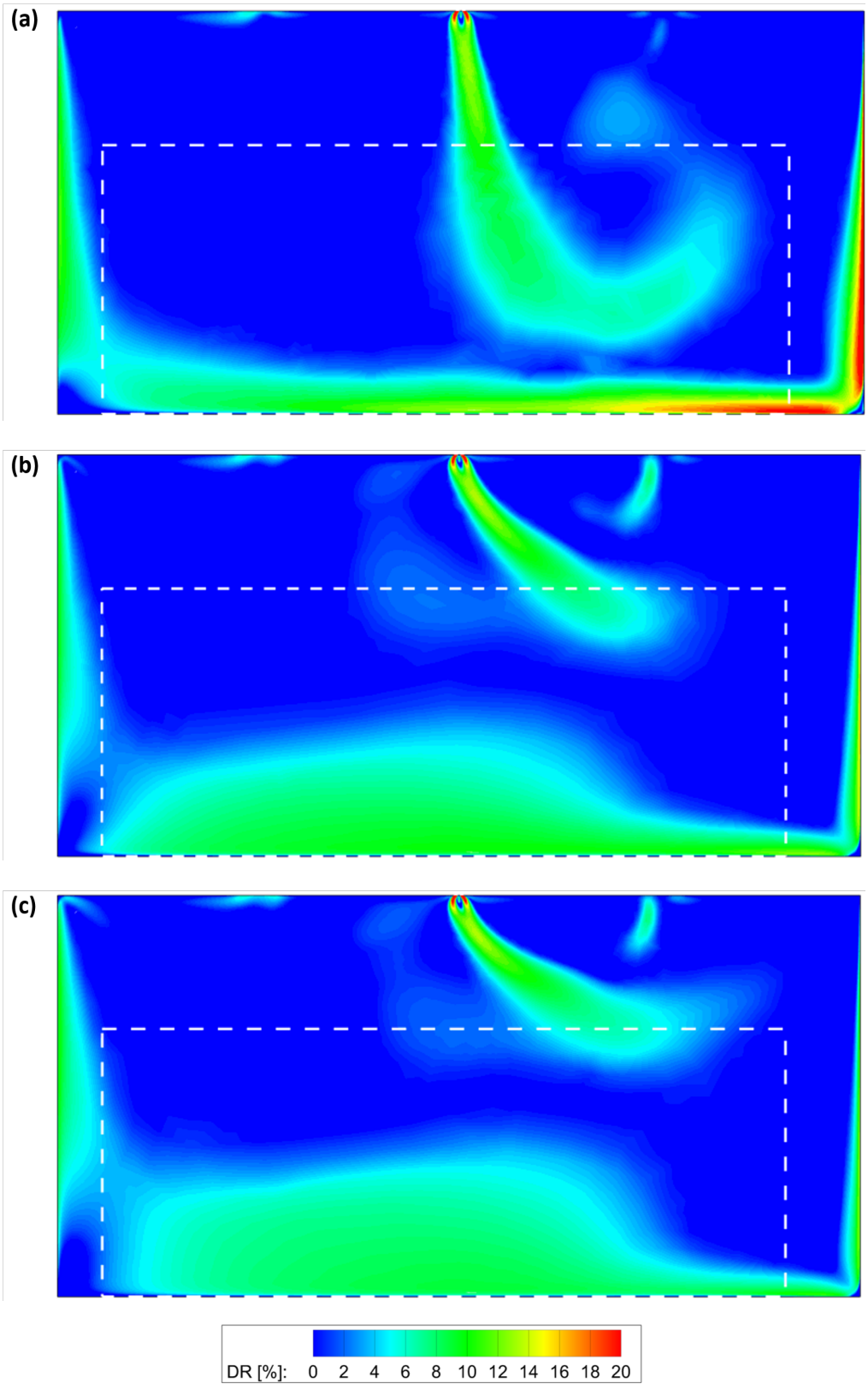

Figure 7.15: Draught rate DR (%) on the center plane (i.e. z = 1.8 m): (a) Scenario 2 (U-factor = 4.1 W/m^2·K). (b) Scenario 2a (U-factor = 1.64 W/m^2·K). (c) Scenario 2b (U-factor = 1.07 W/m^2·K). The dashed box indicates the occupied zone

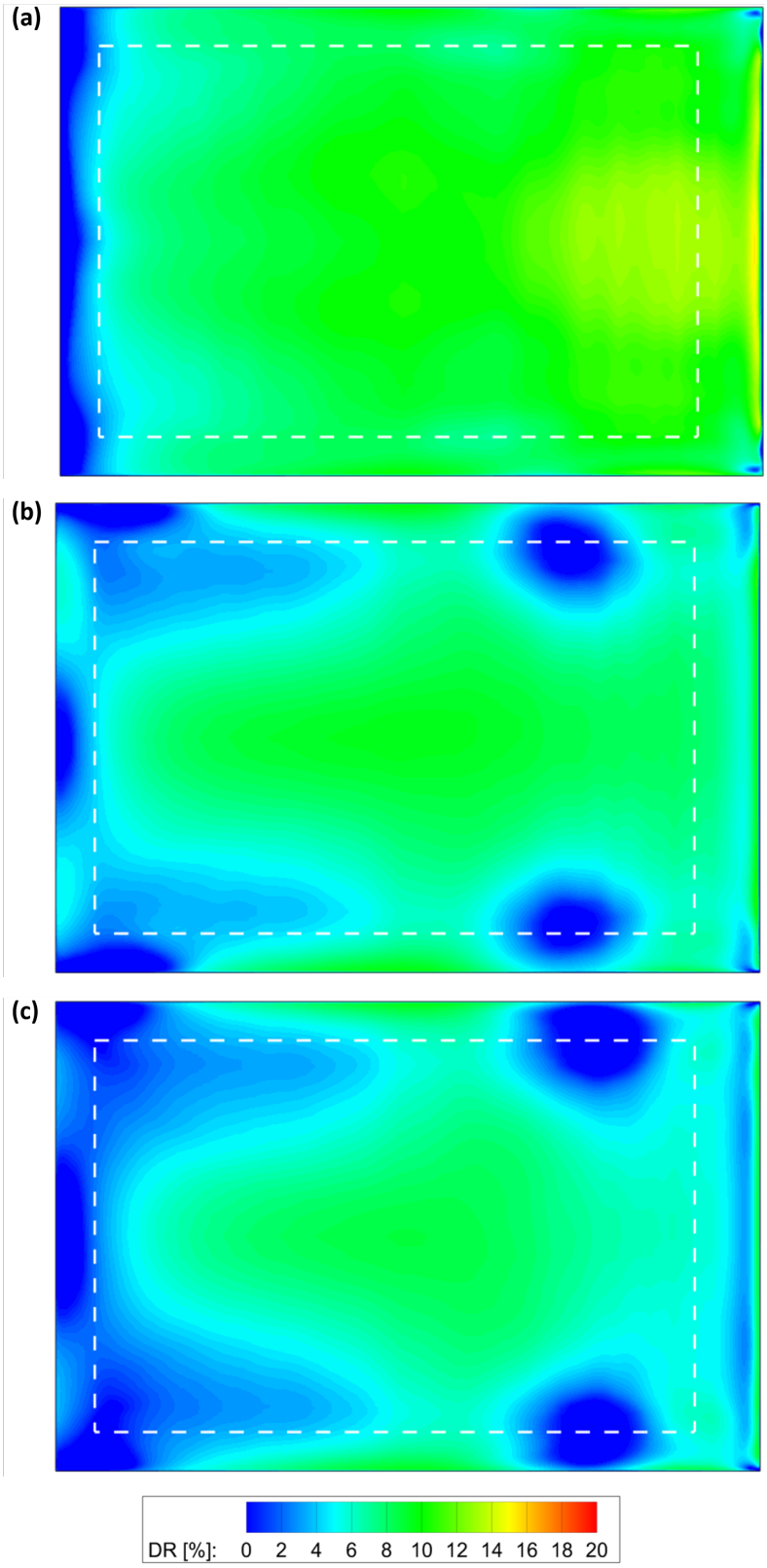

Figure 7.16: Draught rate DR (%) on the horizontal plane (i.e. y = 0.1 m): (a) Scenario 2 (U-factor = 4.1 W/m^2·K). (b) Scenario 2a (U-factor = 1.64 W/m^2·K). (c) Scenario 2b (U-factor = 1.07 W/m^2·K). The dashed box indicates the occupied zone

The results from the optimization study for Scenario 2 (i.e. Scenario 2a and 2b) are compared to the initial Scenario 1 and Scenario 2 to examine whether similar indoor conditions could be realized in the transition from an HTH radiator system to an LTH climate ceiling. Similar to the previous Section 6.1, the results are summarized in two tables to provide an overview of the thermal comfort parameters (see Tables 7.1 and 7.2).

From Table 7.1 it is concluded that the values of T and MRT for 2a and 2b increased . The reduced cold downdraught created a warmer airflow on the facade which penetrated the occupied zone. Also, the surface temperatures of the internal structures (i.e. walls, floor, and ceiling) and the transparent facade element increased due to a decrease in transmission losses which resulted in higher MRT values for both optimization scenarios.

Table 7.1: Overview of mean air temperature T, mean radiant temperature MRT, and operative temperature T_{op} in a fictive point

	Scenario 1	Scenario 2	Scenario 2a	Scenario 2b
T [°C]	22.00	21.42	22.23	22.27
MRT [°C]	22.63	20.49	21.55	21.96
T_{op} [°C]	22.32	20.96	21.89	22.16

From Table 6.2 it is concluded, that optimizing the thermal performance of the transparent facade element improves the thermal comfort and achieved similar conditions as the initial Scenario 1. The maximum values of the velocities (U) in the occupied zone decreased approximately 36.7 and 50% compared to Scenario 2 due to the decrease in temperature gradient between the transparent facade element and the surrounding air. These differences correlate with the percentages observed through multiple experimental studies mentioned in the literature [3, 21]. It is also found that the room temperature is more well-mixed and in combination with the decreased velocity (U) values result in significant lower maximum DR values. The reduction in the occupied zone for Scenario 2a and 2b was 41.2 and 51.82 %, respectively. The obtained values for Scenario 2a and 2b are both below the required threshold of 20% which results in a category B classification. Furthermore, the local discomfort parameters are well below the requirements for the comfort category B classification.

The category B classification for the whole-body index PMV is not achieved, however, this was already the case in the initial Scenario 1. It can be concluded that the improvement in thermal performance (i.e. U-factor) of the transparent facade element has a positive effect on the PMV in Scenario 2a and 2b which leads to similar thermal conditions as Scenario 1.

Table 7.2: Overview of the thermal comfort parameters for the optimization scenarios

Parameter	Category B	Scenario 1	Scenario 2	Scenario 2a	Scenario 2b
DR [%]	< 20	6.98	20.32	11.95	9.79
$T_{a,v}$ [°C]	< 3	0.20	1.1	0.34	0.11
T_f [°C]	19 - 29	23.71	23.58	25.24	25.91
T_{op} [°C]	22.0 ± 2.0	22.32	20.96	21.89	22.16
PMV	$-0.5 <$ PMV $< +0.5$	-0.9	-1.3	-1.0	-0.9

7.3 Conclusion

As mentioned in Subsection 7.1, optimizing the installation concept by increasing the inflow velocity (U_o) and heat flux (q) of the climate ceiling requires additional measures to provide comfortable conditions similar to the initial Scenario 1. However, the optimized Scenario 2a and 2b provide actual alternative for Scenario 3 and 4 to successfully transition towards LTH systems, under the specific model characteristics defined in the research. Therefore, the research provides multiple alternatives to succeed in the energy transition without decreasing the thermal comfort compared to the initial Scenario 1.

8 — Comparative analysis

As mentioned in Section 2.4, empirical formulae derived in literature are primarily used to assess downdraught in a preliminary phase and for existing building configurations. In the preliminary phase, the characteristics of the building are often not known and the empirical formulae provide guidance in assessing downdraught. However, the use of the empirical formulae remains questionable as the experiments performed to derive them were simplified (i.e. no human objects, limited window height between 2 and 3 m, and no counteracting solutions such as heating and ventilation systems) [6]. A comparative analysis is therefore performed to evaluate the usefulness of the empirical formulae related to the numerical results, which is the more extensive method, in assessing downdraught related to thermal comfort. The results of the empirical formulae were compared to the initial Scenario 1, the transition Scenario 2, 3, and 4, and the optimization Scenario 2a and 2b.

The empirical formulae assumes an ideal 2D situation in which the maximum velocity (U_{max}) is provided without spatial distribution in a 3D enclosure [49]. In the 3D situation of the generic office model, U_{max} is found on the center plane above the floor (see Figs. 6.3a-d). However, the exact height above the floor in which U_{max} is observed according to the formulae was not indicated by Heiselberg as the experiment was conducted between 0.01 and 0.5 m above the floor [49]. In addition, Manz and Frank reported that the local maximum velocity was found below 0.1 m above the floor [7]. The numerical results were therefore observed on three different heights (i.e. y = 0.01 m, y = 0.05 m, and y = 0.1 m) from which it was concluded that U_{max} is observed at a height of 0.05 m above the floor. The observed values at that specific height were compared to the empirical results for each scenario.

The LTC tool uses the empirical formulae of Heiselberg (i.e. 2.3a-2.3c) to assess downdraught depending on the distance from the facade. In addition, the corrected formulae of Manz and Frank (i.e. 2.4a-2.4c) were also included in the comparative analysis to evaluate whether it provides a better correlation to the numerical results in terms of downdraught. The formulae of Manz and Frank include internal heat sources which are typically present within an office environment in their estimation [7]. Furthermore, the LTC tool also uses the empirical formula of Heiselberg to estimate the minimum air temperature above the floor region (see Eq. (8.1)). It was decided to implement that specific formula in the comparative analysis as well due to the influence it has on the evaluation of thermal comfort.

$$T_{fr} = T_r - (0.3 - 0.034x) \cdot \Delta T \tag{8.1}$$

where T_r is the indoor air temperature (°C), x is the distance from the facade (m), and ΔT is the temperature difference between the interior surface of the transparent facade element and the indoor air (°C).

Results

The results of the comparative analysis are plotted in the occupied zone at a height of 0.05 m along a reference line located 0.5 m from the facade to 0.3 m from the back wall.

It is observed that the presence of the radiator in Scenario 1 and 3 (i.e. HTH and MTH) counteracts the downdraught experienced on the facade which leads to lower velocity levels in the occupied zone. The empirical results do not account for the counteracting solutions and therefore overestimate the velocity in the occupied zone quite strongly. However, once the radiator is removed or further lowered in capacity (i.e. Scenario 2 and 4) a similar trend can be observed up to 2 m from the facade between the numerical and empirical results (see Figs. 8.1b and 8.1d). The downdraught is regenerated on the facade and penetrates the occupied zone with higher velocity levels. In Scenario 2 the formulae of Heiselberg underestimates the velocity and the use of the formulae by Manz and Frank is considered to be more reliable. In Scenario 4 the downdraught is not fully developed and both empirical formulae overestimate the velocity levels in the occupied zone. Furthermore, the gravity current observed in the experiments by Heiselberg is also not seen in the velocity profiles. The velocity tends to further decrease towards the back of the enclosure for all scenarios.

Overall, it can be concluded that for Scenario 1, 3, and 4 the empirical formulae of Heiselberg is pessimistic as it overpredicts the velocity levels in the occupied zone. However, the use of the formulae in practice indicates that three out of the four scenarios are within limits. Therefore, in Scenarios 1, 3, and 4 the empirical formulae are considered to be useful in assessing downdraught. In Scenario 2, the empirical formulae of Heiselberg underestimate the velocity level in the occupied zone which can be seen especially in the first 1.0 m of the occupied zone. To assess downdraught in that specific scenario, it is recommended to use the corrected formulae of Manz and Frank as the numerical results are within limits.

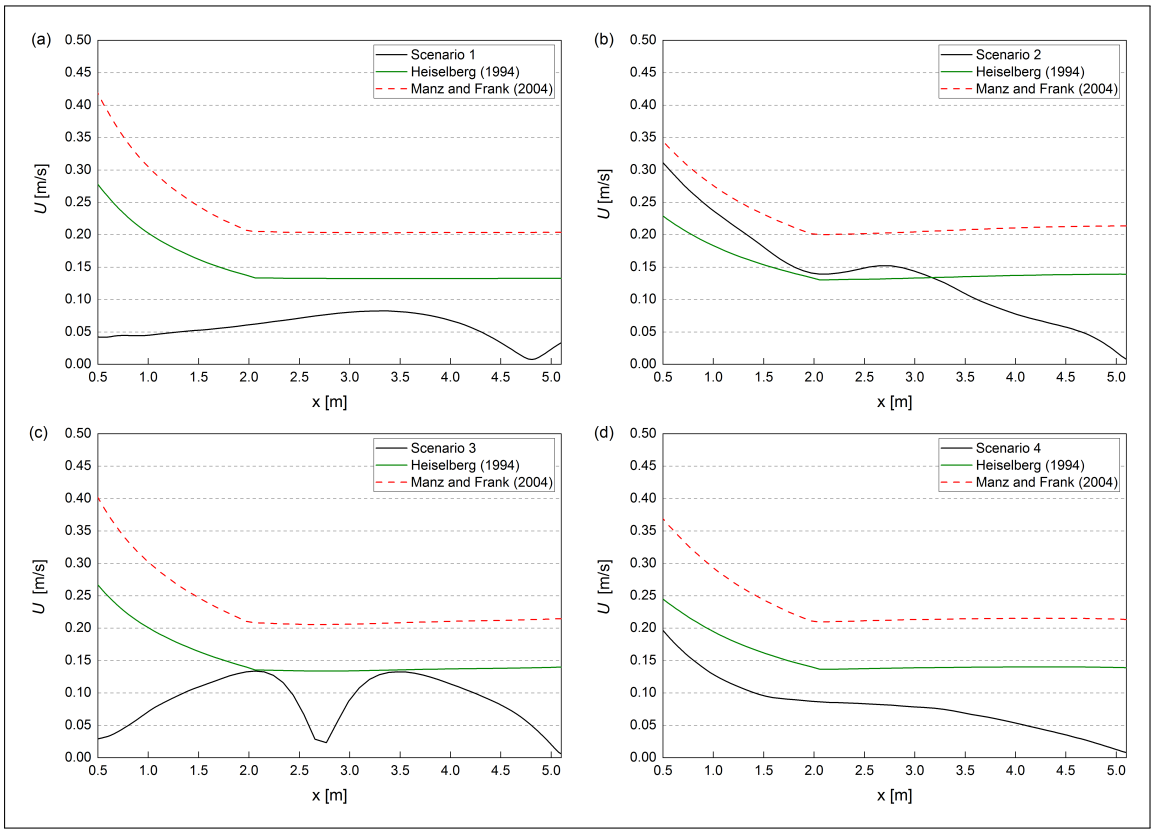

Figure 8.1: Comparison between numerical and empirical results of U in the occupied zone and 0.05 m above the floor

In Figure 8.2 the numerical and empirical results of the air temperature (T) are compared. The results show a similar trend in the occupied zone for all scenarios as an underestimation is observed of approximately 4 to 6 °C in the region of the occupied zone close to the facade which decreases to 2 °C more to the back of the zone. The initial purpose of the formulae derived by Heiselberg is to calculate minimum air temperatures above the floor in the occupied zone. In that sense, the formula is correct as indeed it provides minimum air temperatures compared to the maximum air temperature observed in the numerical results with a difference of approximately 20 to 10 %. Furthermore, it can be concluded that the use of the minimum air temperature obtained through the empirical formula to calculate DR in the LTC tool provide a safe approximation as lower air temperatures results in higher DR values compared to the numerical results.

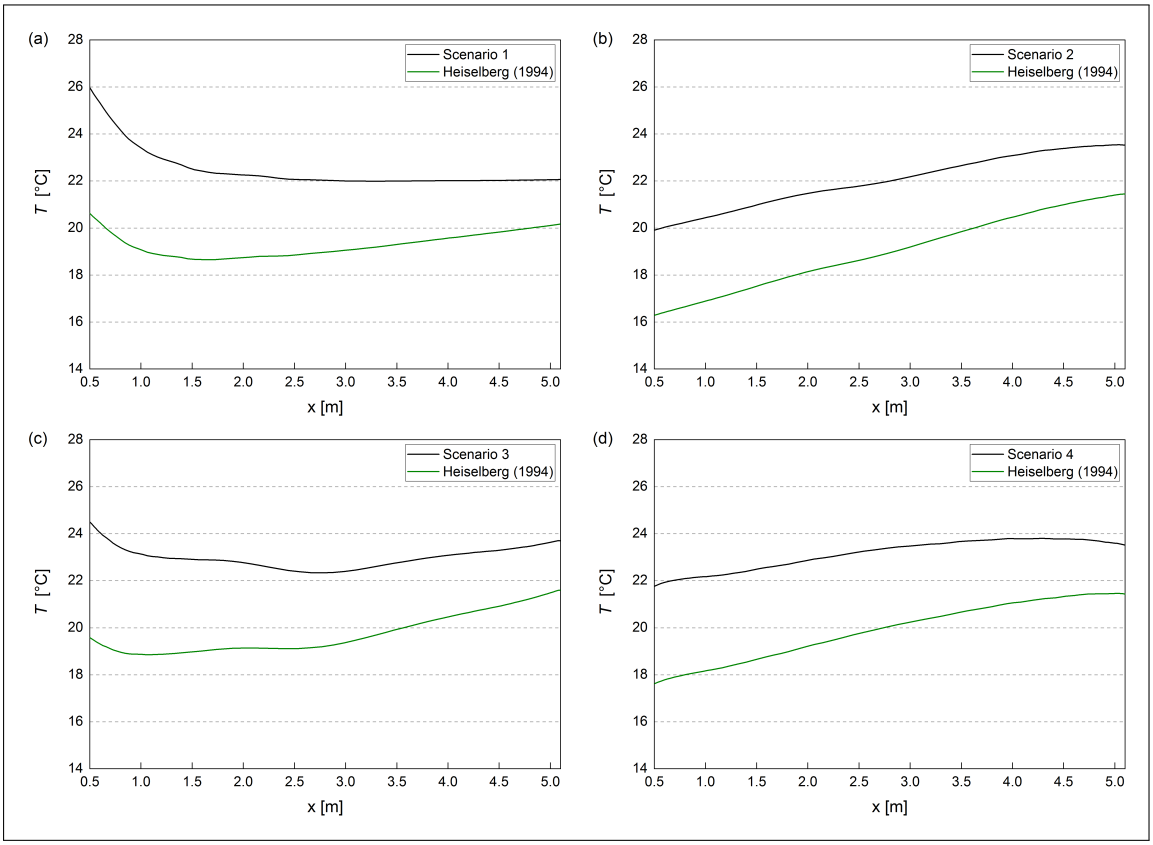

Figure 8.2: Comparison between numerical and empirical results of T in the occupied zone and 0.05 m above the floor

To provide a comprehensive analysis, the results of the scenarios defined in the optimization study in which the thermal performance of the transparent facade element was improved were also compared to the numerical results. Therefore, the analysis evaluates the performance of the formulae under multiple conditions. In the previous Figure 8.1b, the formulae of Manz and Frank provide an upper band estimate of U which is considered to be more suitable than the one derived by Heiselberg. However, it was decided to evaluate the performance of both formulae under improved conditions in Scenario 2a and 2b.

The numerical results of the optimized Scenario 2a and 2b correlate much better with the empirical formulae of Heiselberg compared to the results of the transition scenarios (see Fig. 8.3). The correlation between the empirical formulae of Manz and Frank the numerical results of Scenario 2a and 2b decreased, however, it still provides an upper band estimate of U. Therefore, the use of both formulae will result in an estimation of downdraught in practice within limits. It can be concluded that the use of the empirical formulae provides a good approximation of downdraught in the optimized scenarios.

With respect to T, the comparison also shows small differences in the numerical results of the optimized Scenario 2a and 2b and the empirical results (see Fig. 8.3d and 8.3f). The minimum air temperature calculated with the formula underestimates the numerical results as they provide maximum air temperatures. However, the difference decreased to 1 – 2 °C compared to 2 – 4 °C in the initial Scenario 2 due to the increased temperature in the downdraught.

Although the results show smaller differences in the optimized Scenario 2a and 2b, it is too early to conclude that the formulae perform better under the influence of the improved thermal performance of the transparent facade element assuming only one scenario. Therefore, more simulations need to be compared to define a trend between the results.

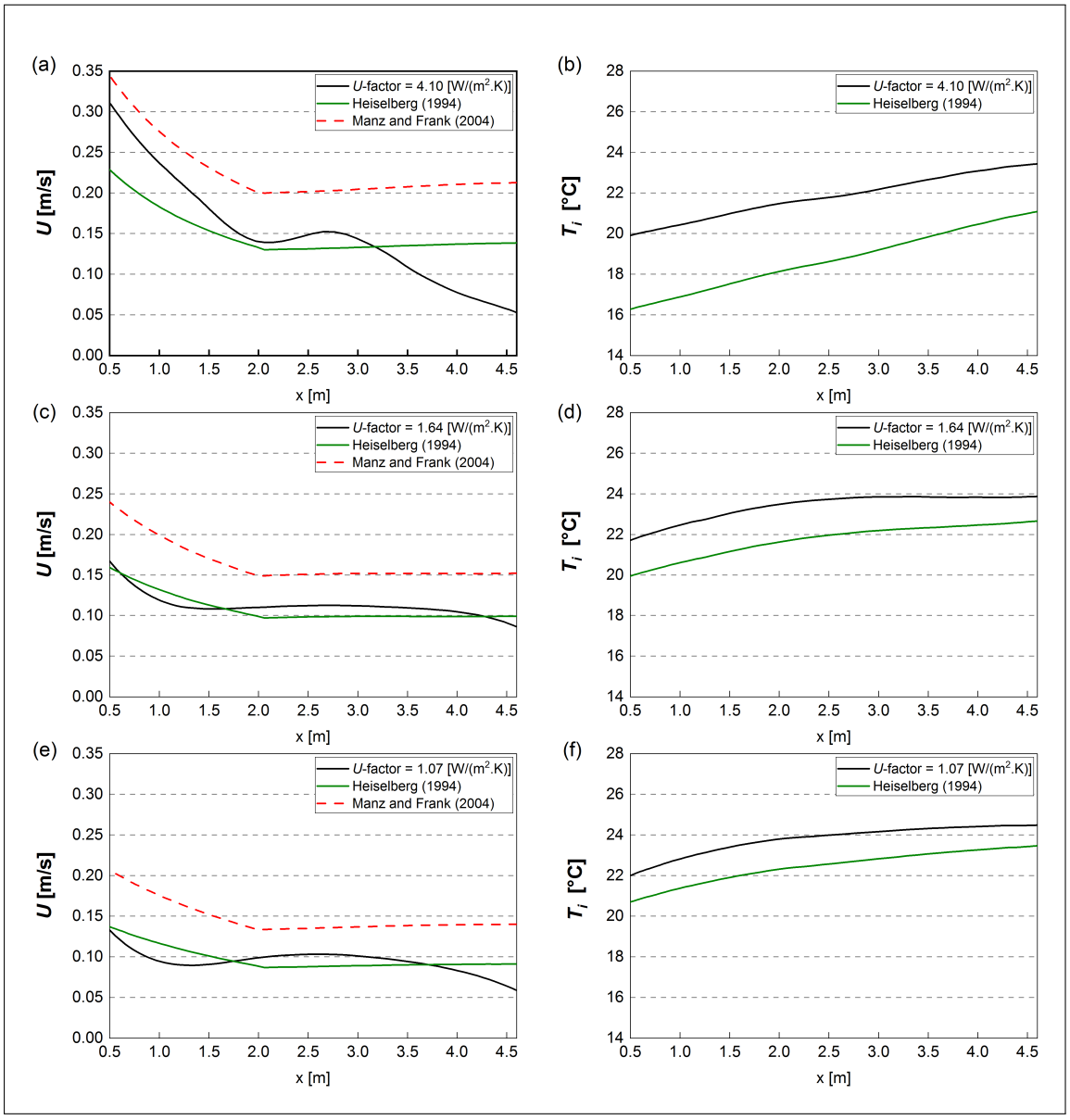

Figure 8.3: Comparison between numerical and empirical results of U and T in the occupied zone and 0.05 m above the floor for the optimization scenarios. Analysis of U: (a) Scenario 2. (c) Scenario 2a. (e) Scenario 2b. Analysis of T: (b) Scenario 2. (d) Scenario 2a. (f) Scenario 2b.

9 — Discussion

The conducted research showed that transitioning from high-temperature to low-temperature heating systems in the defined generic office model decreases the thermal comfort under winter conditions compared to the initial Scenario 1. However, the decrease in thermal comfort of transition Scenario 3 and 4 is considered to be small and therefore provide useful alternatives to succeed in the required energy transition for office buildings. Furthermore, the decrease in thermal comfort of Scenario 2 compared to the initial Scenario 1 can be reduced if the thermal performance of the transparent facade element is increased (i.e. U-factor ≤ 1.64 (W/m^2·K). The combination of implementing a climate ceiling system and an improved performance of the facade will result in an useful alternative to succeed in the energy transition without decreasing the thermal comfort.

The research, however, is subjected to several limitations due to the generic nature of the model and simplifications in the used geometry:

- In the generic office model, an empty room is considered without obstacles (i.e. furniture) and internal heat sources (i.e. humans, lighting, and other electrical devices). Therefore, the downdraught generated on the facade and which penetrates the occupied zone can be underestimated or overestimated in the numerical simulation. Once the penetrating flow collides with an obstacle in the occupied zone it will be redirected around that particular obstacle. In the process of redirection, the penetrating flow can lose momentum due to blockage, however, its momentum could also increase as it moves through a more confined passage. These effects are not observed in the research due to the generic nature of the model (i.e. an empty room). Furthermore, as concluded by Manz and Frank [7] internal heat sources (i.e. humans, computers, etc.) affect the maximum velocity above the floor region. Internal heat sources produce thermal plumes which rise towards the ceiling and will be redirected towards the internal walls and facade. On the vertical structures, the flow tends to move downward and combines with initial flow structures which increases the momentum. Therefore, U above the floor region is underestimated in the research compared to more realistic situations.
- The computational geometry was simplified related to the window bay at the foot of the transparent facade element. In the computational geometry, no distinction was made for the window bay as the transparent and opaque facade elements were defined as a combined planar surface. However, as summarized in Section 2.5 the window bay and other structural elements on the facade influence the downdraught as it decreases the momentum and causes recirculation and separation of the flow.
- One building configuration was chosen to be used within the conducted research. Therefore, the influence of the window height on the downdraught was not examined extensively. The window height has an important role in the empirical formulae together with the U-factor. However, due to time restrictions the influence of the window height on the numerical results, and the comparison with empirical results from the LTC tool were not considered

- One specific ventilation concept was used in the research (i.e. linear slot diffuser). However, it is noticed that the inflow pattern altered in all scenarios and influenced the indoor conditions severely. The influence of the inflow pattern is therefore considered to be important, however, it was not extensive evaluated within the research.

To eliminate the limitations mentioned above, further research is needed to emphasize on the effects of obstacles and internal heat sources, the presence of structural obstacles and bays on the facade, and different window heights. Once the above-mentioned components are considered one will achieve a more comprehensive analysis of the actual effect of switching from an HTH to an LTH system on thermal comfort and the influence of downdraught in the considered generic office model. However, the conducted research provides an overview of flow phenomena and indoor conditions occurring in the transition from HTH to LTH for a generic office model which can be applied over a broader range of office configurations.

10 — Conclusion

The research aimed to evaluate whether the transition from a high-temperature to a low-temperature heating system would decrease the thermal comfort perceived in a generic office environment. The conclusions of the research were drawn with the use of numerical simulations in a generic office model with characteristics from the building period 1988 to 1992. The generic nature of the model was chosen to interpret the results of the research over a wide range of office buildings. The overall results are summarized once more to conclude on the defined research questions (see Subsection 1.3).

The transition from high-temperature heating to a low-temperature heating system was defined twofold: (i) replacing the entire radiator with a climate ceiling and (ii) gradually decreasing the capacity of the radiator and complement the required energy with a partial climate ceiling (i.e. MTH and LTH) (see Section 3.3). It is concluded from the numerical simulations that in all defined scenarios the thermal comfort perception in the generic office model decreased compared to the initial Scenario 1 (i.e. HTH radiator). However, it is found that the decrease in thermal comfort for Scenario 3 and 4 in which the radiator reduced in capacity was negligible. Therefore, the transition scenarios provide useful alternatives to contribute to the required energy transition in the generic office model with the specific characteristics. In Scenario 2 (i.e. removal of the radiator) the momentum in the downdraught caused by buoyancy forces increases on the facade as no counteracting flow was present. The downdraught transitions from a vertical to horizontal flow at the foot of the facade and penetrates the occupied zone. In the occupied zone it causes thermal discomfort as increased velocity levels are experienced and combined with colder air temperatures caused an increase in the draught rate (DR). Therefore, Scenario 2 was considered to be not suitable as it provides uncomfortable conditions compared to the initial Scenario 1.

However, Scenario 2 is often desired as the removal of the radiator increases the floor space which can be utilized in an office environment. Therefore, a twofold optimization study was performed: (i) optimizing the installation concept (i.e. increasing the inflow velocity and heat flux of the climate ceiling) and (ii) increase the thermal performance of the transparent facade element. It is concluded that optimizing the installation concept influences the perceived conditions within the generic office model. However, the perceived conditions required additional measures and research to provide comfortable conditions which are similar or improved compared to initial Scenario 1. To achieve similar thermal comfort conditions with Scenario 2 it was concluded that the thermal performance of the transparent facade element should be increased to a U-factor of $\leq$ 1.64 W/m^2·K. Improving the thermal performance decreases the buoyancy forces generated on the facade because of a smaller temperature gradient near the surface. Therefore, the downdraught lowered in velocity and penetration depth in the occupied zone with higher air temperatures. It is concluded that in the case of a stand-alone climate ceiling the thermal performance has to be improved to provide conditions that are comparable with the initial Scenario 1.

Furthermore, the accuracy of the LTC tool used by RHDHV was evaluated through a comparative analysis in which the numerical results were compared to the empirical results. It is concluded that for Scenario 1, 3, and 4 the empirical formulae of Heiselberg (i.e. U_{max}) is pessimistic as it overpredicts the velocity levels in the occupied zone. However, the use of formulae in practice indicates that these scenarios are within limits and therefore the empirical formulae can be considered as useful. In Scenario 2, the empirical formulae of Manz and Frank provide a better correlation compared to the case of Heiselberg which underestimates the results. From the optimization study it is concluded that with an improved thermal performance in Scenario 2a and 2b the correlation with the empirical formulae used in the LTC tool improved significantly. However, it requires additional research under different conditions to make a comprehensive statement. A similar trend is observed between the numerical and empirical results of the air temperature T. The empirical formulae underestimates the actual air temperatures and the difference decreases in the case of an improved thermal performance in Scenario 2a and 2b. Overall, it is concluded that the use of the LTC tool provides safe assumptions in terms of U and T which are suitable for the current role of the tool within the assignment of RHDHV.

Bibliography

[1] TNO. Sustainable buildings: Towards an energy producing built environment.

[2] Milieu Centraal. Lage temperatuur verwarming.

[3] U. Larsson and B. Moshfegh. Experimental investigation of downdraught from well-insulated windows. *Building and Environment*, 37(11):1073–1082, 2002.

[4] Neil E. Klepeis, William C. Nelson, Wayne R. Ott, John P. Robinson, Andy M. Tsang, Paul Switzer, Joseph V. Behar, Stephen C. Hern, and William H. Engelmann. The National Human Activity Pattern Survey (NHAPS): A resource for assessing exposure to environmental pollutants. *Journal of Exposure Analysis and Environmental Epidemiology*, 11(3):231–252, 2001.

[5] Joint Research Centre. Indoor air pollution: new EU research reveals higher risks than previously thought, 2003.

[6] L Schellen, S Timmers, M Loomans, E Nelissen, J L M Hensen, and W Van Marken Lichtenbelt. Downdraught assessment during design: Experimental and numerical evaluation of a rule of thumb. *Building and Environment*, 57:290–301, 2012.

[7] Heinrich Manz and T. Frank. Analysis of thermal comfort near cold vertical surfaces by means of computational fluid dynamics. *Indoor and Built Environment*, 13(3):233–242, 2004.

[8] B Blocken. 50 years of Computational Wind Engineering: Past, present and future. *Journal of Wind Engineering and Industrial Aerodynamics*, 129:69–102, 2014.

[9] PV Nielsen. Specification of a two-dimensional test case. Technical report: Air flow pattern within buildings. Annex 20. *International Energy Agency*, 1990.

[10] Y Li, M Sandberg, and L Fuchs. Effects of thermal radiation on airflow with displacement ventilation: an experimental investigation. Technical report, 1993.

[11] ISO. ISO 7730 Ergonomics of the thermal environment - Analytical determination and interpretation of thermal comfort using calculation of the PMV and PPD indices and local thermal discomfort criteria. Technical report, 2005.

[12] J Van Hoof. Forty years of Fanger's model of thermal comfort: Comfort for all? *Indoor Air*, 18(3):182–201, 2008.

[13] P. O. Fanger. Prediction of local discomfort for man. *Studies in Environmental Science*, 10(C):221–227, 1981.

[14] A Bejan and A D Kraus. *Heat Transfer Handbook, Volume 1*. 2003.

[15] R A W M Henkes. *Natural-convection boundary layer*. PhD thesis, 1990.

[16] P Heiselberg. Draught Risk From Cold Vertical Surfaces. *Building and Environment*, 29(3):297–301, 1994.

[17] T L J den Boer and W Zeiler. Transparantie & façade. *TVVL Magazine*, 37(5):10, 2008.

[18] B W Olesen. Vereinfachte methode zur vorausberechnung des thermischen raumklimas. *Heiz. Luftung Klima Haustech*, 46:219–225, 1995.

[19] E R Eckert and T W Jackson. Analysis of turbulent free-convection boundary layer on flate plate. Technical report, NACA, 1950.

[20] P Heiselberg. Aalborg Universitet Energy-Efficient Measures to Avoid Downdraft from Large Glazed Facades Heiselberg, Per Kvols; Overby, H.; Bjørn, Erik. 1996.

[21] H Ge and P Fazio. Experimental investigation of cold draft induced by two different types of glazing panels in metal curtain walls. *Building and Environment*, 39(2):115–125, 2004.

[22] RVO. Energielabel C kantoren, 2021.

[23] NEN. NTA 8800+A1 Energieprestatie van gebouwen - Bepalingsmethod. Technical Report december, 2020.

[24] RCE. Kantoorgebouwen in Nederland 1945-2015 cultuurhistorische en typologische quickscan. pages 1–20, 2013.

[25] ISSO. Sofwaretool verwarmingslichaam selecteren, 2014.

[26] TROX Technik. Lijnrooster voor plafondinbouw - Serie VSD 50. Technical report, 2018.

[27] X Cheng, H Zhang, W Pan, S Liu, M Zhang, Z Long, T Zhang, and Q Chen. Field study of infiltration rate and its influence on indoor air quality in an apartment. *Procedia Engineering*, 205:3954–3961, 2017.

[28] A D Lemaire, Q Chen, M Ewert, J Heikkinen, C Inard, A Moser, P V Nielsen, and G Whittle. Room air and contaminant flow, evaluation of computational methods, subtask-1 Summary Report. *IEA Annex 20: Air Flow Patterns within Buildings*, page 82, 1993.

[29] P V Nielsen. *Flow in air conditioned rooms: Model experiments and numerical solution of the flow equations*. PhD thesis, 1974.

[30] P. V. Nielsen, L. Rong, and I. Olmedo. The IEA Annex 20 Two-Dimensional Benchmark Test for CFD Predictions. *Clima 2010, 10th REHVA World Congress*, 1(June):978–975, 2010.

[31] Z Zhai, Z Zhang, W Zhang, and Q Chen. Evaluation of various turbulence models in predicting airflow and turbulence in enclosed environments by CFD: Part 1 - summary of prevalent turbulence models. *HVAC and R Research*, 13(6):853–870, 2007.

[32] ANSYS. *FLUENT 12.0 User's Guide*. ANSYS, 2009.

[33] T van Hooff and B Blocken. Low-Reynolds number mixing ventilation flows: Impact of physical and numerical diffusion on flow and dispersion. *Building Simulation*, 10(4):589–606, 8 2017.

[34] T van Hooff and B Blocken. Mixing ventilation driven by two oppositely located supply jets with a time-periodic supply velocity: A numerical analysis using computational fluid dynamics. *Indoor and Built Environment*, 29(4):603–620, 4 2020.

[35] PJ Roache. Quantification of uncertainty in Computational Fluid Dynamics. *Annu. Rev. Fluid. Mech*, 29:123–60, 1997.

[36] M. Schatzmann, H. Olesen, and J. Franke. COST 732 model evaluation case studies: approach and results. Technical report, COST, 2010.

[37] B W Olesen, E Mortensen, J Thorshauge, and B Berg-Munch. Thermal Comfort in a Room Heated by Different Methods - Technical paper no. 2256. *ASHRAE Transactions 86*, pages 34–48, 1980.

[38] J Myhren and S Holmberg. Flow patterns and thermal comfort in a room with panel, floor and wall heating. *Energy and Buildings*, 40(4):524–536, 2008.

[39] Y Wang, X Zhang, J Ji, Z Tian, and Y Li. Numerical simulation of thermal performance of indoor airflow in heating room. *Energy Procedia*, 158:3277–3283, 2019.

[40] S Gilani, H Montazeri, and B Blocken. CFD simulation of stratified indoor environment in displacement ventilation: Validation and sensitivity analysis. *Building and Environment*, 95:299–313, 1 2016.

[41] S. Aliu, O. M. Amoo, F. I. Alao, and S. O. Ajadi. *Mechanisms of heat transfer and boundary layers*. Elsevier Ltd, 2020.

[42] F. P. Incropera, D. P. DeWitt, T. L. Bergman, and A.S. Lavine. *Fundamentals of heat and mass transfer*. John Wiley & Sons, sixth edition, 2007.

[43] B Blocken. Computational Fluid Dynamics for urban physics: Importance, scales, possibilities, limitations and ten tips and tricks towards accurate and reliable simulations. *Building and Environment*, 91:219–245, 2015.

[44] W. K. Chow and J. Li. Numerical simulations on thermal plumes with k-ϵ types of turbulence models. *Building and Environment*, 42(8):2819–2828, 2007.

[45] Z Zhang, W Zhang, Z Zhai, and Q Chen. Evaluation of various turbulence models in predicting airflow and turbulence in enclosed environments by CFD: Part 2—comparison with experimental data from literature. *HVAC and R Research*, 13(6):871–886, 2007.

[46] A C van der Linder, P Erdtsieck, L Kuijpers-van Gaalen, and A Zeegers. *Building Physics*. ThiemeMeulenhoff, 1st edition, 2013.

[47] Kennisinstituur voor Installatietechniek. ISSO-publicatie 66 Vermogen van radiatoren en convectoren in praktijksituaties. Technical report, 1986.

[48] Kennisinstituut voor installatietechniek. *ISSO-publicatie 48 Klimaatplafonds / Koelconvectoren*. ISSO, 1998.

[49] P Heiselberg, S Murakami, and CA Roulet. Ventilation of large spaces in buildings. *Final Report IEA Annex*, 1998.

[50] Rijksoverheid. Bouwbesluit 2012, 2021.

[51] ISSO. *Warmteverliesberekening voor utiliteitsgebouwen met vertrekhoogten tot 5 meter (ISSO 53)*. 2012.

A — Energy balance (ISSO 53)

The appendix provides an extensive calculation of the design heat loss (Φ_{HL}) which is equivalent to the required power out of the heating system to guarantee comfortable indoor conditions according to the boundary conditions of the calculation. ISSO-publication 53 is used to calculate Φ_{HL} using the characteristics of the generic office model as mentioned in Section 3.2 [51].

Φ_{HL} consists of multiple components namely transmission losses (direct and indirect), ventilation and infiltration losses, an allowance for business restriction, and heat gains from sources in the building. However, due to a simplification in the characteristics of the model, it is decided to neglect the infiltration losses, business restrictions, and heat gains in the energy balance. Eventually, Φ_{HL} is calculated with Eq. (A.1)

$$\Phi_{HL} = \Phi_T + \Phi_V \tag{A.1}$$

where Φ_T is the transmission heat loss (W) and Φ_V is the ventilation heat loss (W).

Transmission losses

The assumption is made that all internal structures have an adiabatic relation with the adjacent volumes (i.e. no internal transmission losses). Therefore, only the transparent and opaque facade elements are considered in the calculation of Φ_T. The specific transmission heat loss $H_{T,e}$ is calculated for the individual facade elements using Eq. (A.2)

$$H_{T,e} = \sum_k \left(A_k \cdot \left(U_k + \Delta U_{TB}\right) \cdot f_k\right) \tag{A.2}$$

where A is the surface (m^2), U the thermal transmittance ($W/m^2 \cdot K$), ΔU_{TB} allowance for thermal bridging ($W/m^2 \cdot K$), and f_k a correction factor for the temperature gradient of the structure. ΔU_{TB} has a value of 0.10 for situations other than new built buildings and internal insulation, and f_k has a value of 1.0 for external walls [51].The specific transmission heat losses for the individual facade elements are summarized in Table A.1

Table A.1: Overview of the specific transmission losses of the facade elements $H_{T,e}$

Facade element	A [m^2]	U-factor [$W/m^2 \cdot K$]	ΔU_{TB} [$W/m^2 \cdot K$]	f_k [-]	$H_{T,e}$ [W/K]
Transparent	4.05	4.10	0.10	1.00	17.01
Opaque	5.67	0.46	0.10	1.00	3.18

To obtain Φ_T, $H_{T,e}$ is multiplied with the temperature gradient between the indoor and outdoor air (i.e. T_i = 21 °C and T_e = -5 °C). The heat loss through transmission of the transparent and opaque facade element is 442.26 and 82.68 W, respectively (see Eq. (A.3)).

$$\Phi_T = H_{T,e} \cdot (T_i - T_e) \tag{A.3}$$

Ventilation losses

The specific ventilation heat loss H_V is calculated using Eq. (A.5)

$$H_V = z \cdot q_v \cdot \rho \cdot c_p \cdot f_v \tag{A.4}$$

where z is a reduction factor, q_v the volumetric flow rate (m^3/s), ρ the density (kg/m^3), c_p the specific heat of air (J/kg·K), and f_v a correction factor (-). q_v is estimated based on three persons with a flow rate of 35 m^3/h per person. z has a value of 1.0 for an enclosure with only one external wall and f_v has a value of 1.0 as the temperature gradient between the ventilation and indoor air is only 3 °C. The specific ventilation heat loss is summarized in Table A.2.

Table A.2: Specific ventilation heat loss H_V

Ventilation	z [-]	q_v [m^3/s]	ρ [kg/m^3]	c_p [J/kg·K]	f_v [-]	H_V [W/K]
Mechanical supply	1.00	0.029	1.20	1000.00	1.00	35.00

To obtain Φ_V, H_V is eventually multiplied with the temperature gradient between the supply air and indoor air (i.e. T_l = 18 °C and T_i = 21 °C). The heat loss through ventilation is 105 W (see Eq. (A.5)).

$$\Phi_V = H_V \cdot (T_i - T_l) \tag{A.5}$$

Design heat loss

The design heat loss Φ_{HL} is calculated by adding the transmission and ventilation losses (see Eq. (A.6). Φ_{HL} is estimated for the generic office model characterized as mentioned in Section 3.2 with a value of 629.94 W.

$$\begin{aligned} \Phi_{HL} &= \Phi_T + \Phi_V \\ \Phi_{HL} &= (442.26 + 82.68) + 105.00 = 629.94W \end{aligned} \tag{A.6}$$

B — Interior surface temperature

The internal surface temperatures were calculated to account for transmission losses through the transparent and opaque elements of the facade. The surface temperatures were calculated using Eq. (5.1) and was summarized in Tables B.1 and B.2. The internal surface temperatures were used as a fixed temperature condition for the transparent and opaque facade elements and have a value of 7.15 and 19.44 °C, respectively.

For convenience, the heat transmittance U_g for the transparent element was transformed into a total heat resistance R_T (m^2·K/W) of the element including the interior and exterior heat transfer resistances R_{si} and R_{se} using Eq. B.1:

$$R_T = \frac{1}{U_g} \tag{B.1}$$

The heat resistance of the transparent layer R_n was estimated by subtracting the resistances R_{si} and R_{se} which resulted in a value of 0.074 m^2·K/W.

Table B.1: Calculation of the internal surface temperature of the opaque facade element

Construction layer	R_n [m^2·K/W]	ΔT_n [°C]	T_n [°C]
Outdoor air			-5
R_{se}	0.04	0.48	-4.52
Facade	2.0	23.79	19.44
R_{si}	0.13	1.56	
Indoor air			21
Total	2.17		

Table B.2: Calculation of the internal surface temperature of the transparent facade element

Construction layer	R_n [m^2·K/W]	ΔT_n [°C]	T_n [°C]
Outdoor air			-5
R_{se}	0.04	4.26	-0.74
Window	0.074	7.89	7.15
R_{si}	0.13	13.85	
Indoor air			21
Total	0.244		

In addition, the calculation of the interior surface temperatures of the optimized transparent elements in Scenario 2a and 2b is summarized in Tables B.3 and B.4. The interior surface temperatures were estimated at a value of 15.45 and 17.36 °C, respectively.

Table B.3: Calculation of the internal surface temperature of the transparent facade element for optimization Scenario 2a

Construction layer	R_n [m^2·K/W]	ΔT_n [°C]	T_n [°C]
Outdoor air			-5
R_{se}	0.04	1.7	-3.3
Window	0.44	18.75	15.45
R_{si}	0.13	0.54	
Indoor air			21
Total	0.61		

Table B.4: Calculation of the internal surface temperature of the transparent facade element for optimization Scenario 2b

Construction layer	R_n [m^2·K/W]	ΔT_n [°C]	T_n [°C]
Outdoor air			-5
R_{se}	0.04	1.12	-3.88
Window	0.76	21.25	17.36
R_{si}	0.13	3.63	
Indoor air			21
Total	0.93		

C — Sensitivity of radiator temperature

The energy released by the radiator was calculated to satisfy the energy balance of 629.94 W conducted in Appendix A. However, the design heat loss (Φ_{HL}) has to be modified to specify the required radiator power as defined in ISSO-publication 66 [48]. A corrected heat loss ϕ_{wv} was calculated using Eq. (C.1)

$$\Phi_{wv} = \varphi_v \cdot \Phi_{HL} \tag{C.1}$$

where φ_v is the correction factor for extra heat losses through the external wall (-), and Φ_{HL} the design heat loss (W). The value of φ_v was estimated at 1.01 representing a situation in which a normal external wall was placed behind the radiator [48]. Therefore, Φ_{wv} was estimated at a value of 636.24 W.

Furthermore, the corrected heat loss is corrected once more in the situation that it deviates from a normalized radiator setup according to NEN standards [48]. A correction factor of overtemperature φ_o was calculated using Eq. (C.2)

$$\varphi_o = \left(\frac{50}{\frac{T_s+T_r}{2} - T_i} \right)^1 .3 \tag{C.2}$$

where T_s is the supply temperature, T_r the return temperature, and T_i the indoor air temperature within the enclosure. The values of φ_o are summarized in Table C.1.

Table C.1: The correction factor for overtemperature φ_o

T_s [°C]	T_r [°C]	T_i [°C]	φ_o [W]
80	60	21	1.03
50	40	21	2.60
35	30	21	6.76

The selection power output Φ_s to satisfy the energy balance was further calculated by multiplying the corrected heat loss with the correction for overtemperature using Eq. (C.3).

$$\Phi_s = \varphi_o \cdot \Phi_w v \tag{C.3}$$

It was calculated that Φ_s to satisfy the energy balance for the HTH, MTH, and LTH radiator has to be 655.33, 1653.22, and 4300.98 W, respectively. The MTH and LTH radiator needs to be enlarged by a factor of 2.60 and 6.76, respectively to have an equal energy output of the HTH radiator.

The required heat flux q (W/m^2) was calculated based on the radiator dimensions of 0.1 x 0.06 (W x H) using Eq. (4.7). The source energy term defined in ANSYS Fluent for the HTH, MTH, and LTH radiator had a value of 655.33, 252.02, and 96.93 W/m^3, respectively as the volume of the radiator remained similar in all cases.

The surface temperatures of the radiator for the different temperature trajectories are displayed in Figure C.1. It is concluded that the surface temperatures of the radiators in all scenarios are very low compared to realistic conditions which can be expected using the supply T_s and return T_r temperatures (i.e. HTH = 70 °C, MTH = 50 °C, and LTH 32.5 °C)

The underestimated surface temperatures also influence the flow conditions within the enclosure negatively (i.e. thermal plume, recirculation, etc.). Furthermore, an attempt was made to increase the source term by decreasing the volume of the radiator (i.e. higher heat flux). However, similar underestimations of the surface temperature were found. Therefore, it was decided to continue with a fixed temperature boundary condition corresponding to the average of T_f and T_r for each individual trajectory.

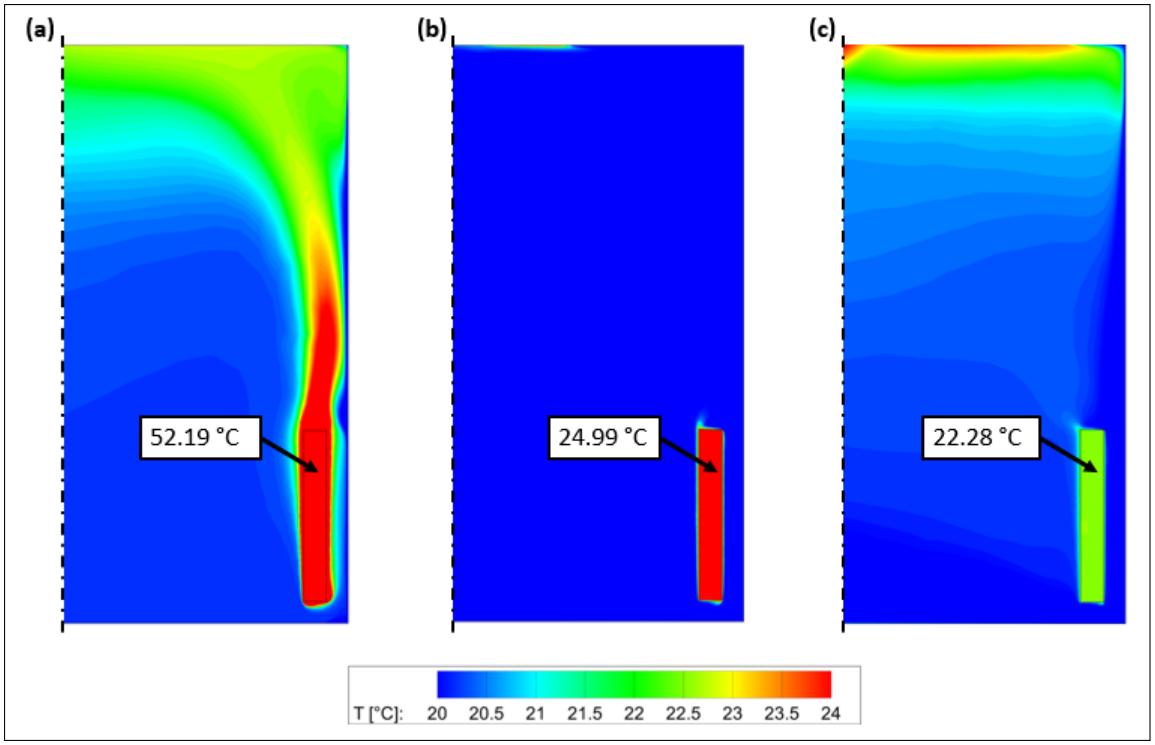

Figure C.1: Simulated surface temperatures of the HTH, MTH, and LTH radiator

D — 2D sensitivity of inflow pattern

A sensitivity analysis was performed to examine the reliability of the inflow pattern from the linear slot diffuser. The analysis included an isothermal and non-isothermal simulation to visualize the general flow development under multiple conditions. The simulations were performed with a 2D representation of the generic office model as described in Section 3.2.

Computational geometry

The 2D representation of the generic office was made on the center plane of the 3D generic office case (see Fig. D.1). The dimensions of the computational geometry were 5.4 x 2.7 m^2 (L x H). Furthermore, the characteristics for the inlet, outlet, and heating system were similar to the 3D generic office as mentioned in Subsection 5.1.1.

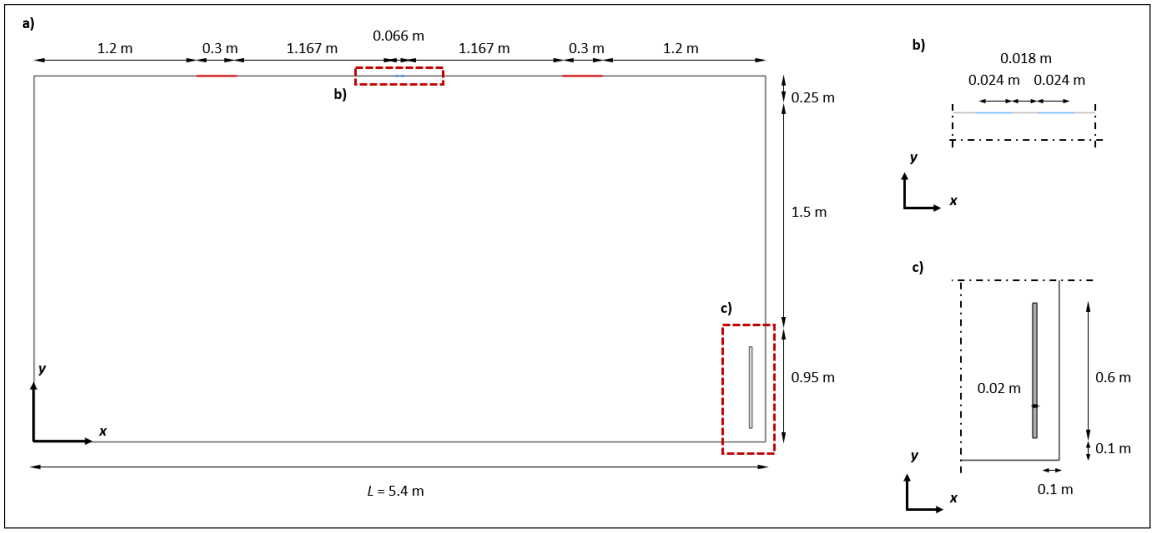

Figure D.1: (a) 2D computational geometry. (b-c) Close-up view of geometry: (b) ventilation inlet; (c) radiator

Computational grid

The computational grid was built according to the described characteristics in Subsection 5.1.2 (see Fig. D.2). A structured boundary layer was formed on the domain and radiators walls using hexahedral cells only. Furthermore, an unstructured inner region was formed using quadrilateral cells built with the quad pave face meshing method. The computational grid consists of 37,686 cells.

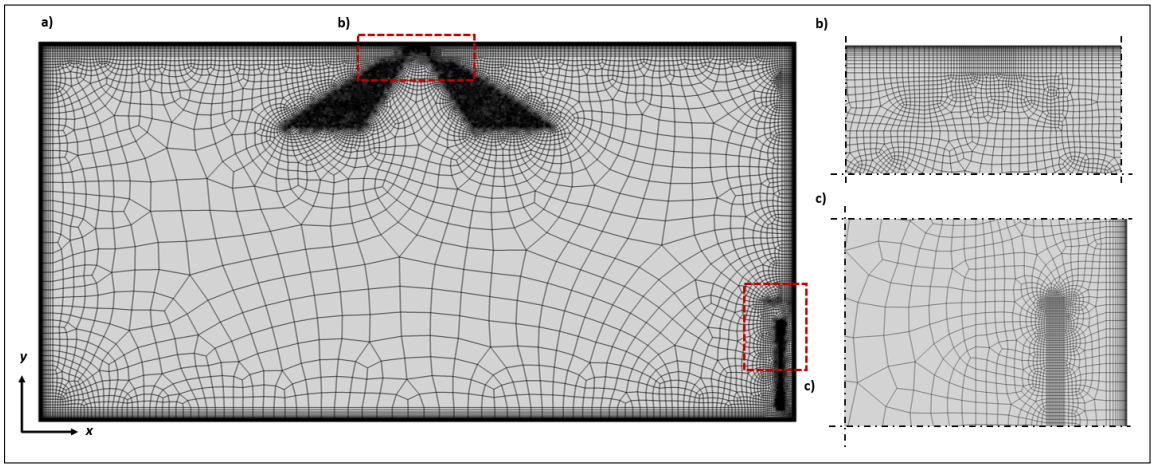

Figure D.2: (a) 2D computational grid. (b-c) Close-up view of grid: (b) inlet region; (c) radiator

Boundary conditions

The boundary conditions used for the sensitivity analysis were similar to the initial conditions of Scenario 1 as mentioned in Subsection 5.1.3. The inflow conditions were $U_0 = 0.48$ m/s, $T_i = 18$ °C, $I = 10\%$, and a turbulent viscosity ratio of 10. The outflow conditions had zero static gauge pressure and $T_o = 21$ °C. The wall conditions assume an adiabatic relation between the internal construction elements (i.e. walls, ceiling, and floor) which had a fixed heat flux of zero. Transmission losses were accounted for by applying a fixed surface temperature of 7.15 and 19.31 °C, respectively for the open and closed facade elements. The energy released by the radiator in the non-isothermal simulation was realized through a fixed temperature of 70 °C (i.e. HTH).

Furthermore, no-slip conditions were applied at the walls of the enclosure

Solver settings

The 2D steady RANS equations were solved using the RNG k-ϵ turbulence model combined with the two-layer EWT zonal model. The SIMPLEC algorithm was used for pressure-velocity coupling, PRESTO! scheme for pressure interpolation and the second-order discretization scheme was used for the momentum, k, ϵ and energy (i.e. non-isothermal simulation). The numerical simulations were performed using ANSYS Fluent 19.2 (2018).

Convergence of the scaled residuals was declared once they did not show any further reduction related to an increase in iterations.

Results

The flow development of the isothermal and non-isothermal simulations was examined through the velocity magnitude U. The results from the individual simulations are displayed in Figures D.3a-d.

It is observed that the initial flow development from the linear slot tends to remain attached along the surface of the ceiling due to pressure differences (i.e. Coanda effect) (see Fig. D.3a). At a certain distance from the inlet, the jet separates from the ceiling and under the influence of gravity forms two recirculation flows within the enclosure. The Coanda effect was also observed in the non-isothermal simulation in which the surface temperature of the facade was enabled (see Fig. D.3b). However, the recirculation flow was interrupted by the downdraught due to the large temperature difference along the facade which resulted in an increased velocity along the floor.

The initial flow development was completely changed by enabling the radiator in the non-isothermal simulation (see Fig. D.3c). The buoyancy-driven flow originating from the radiator created an acceleration in terms of velocity which disrupted the Coanda effect. In Fig. D.3d, the inflow velocity U_0 was increased to 0.83 m/s in an attempt to restore the Coanda effect along the ceiling. However, the buoyancy driven-flow from the radiator was too strong.

Overall, it is concluded that the linear slot diffuser showed a reliable flow development which was strongly influenced by external factors within the enclosure (i.e. downdraught and buoyancy).

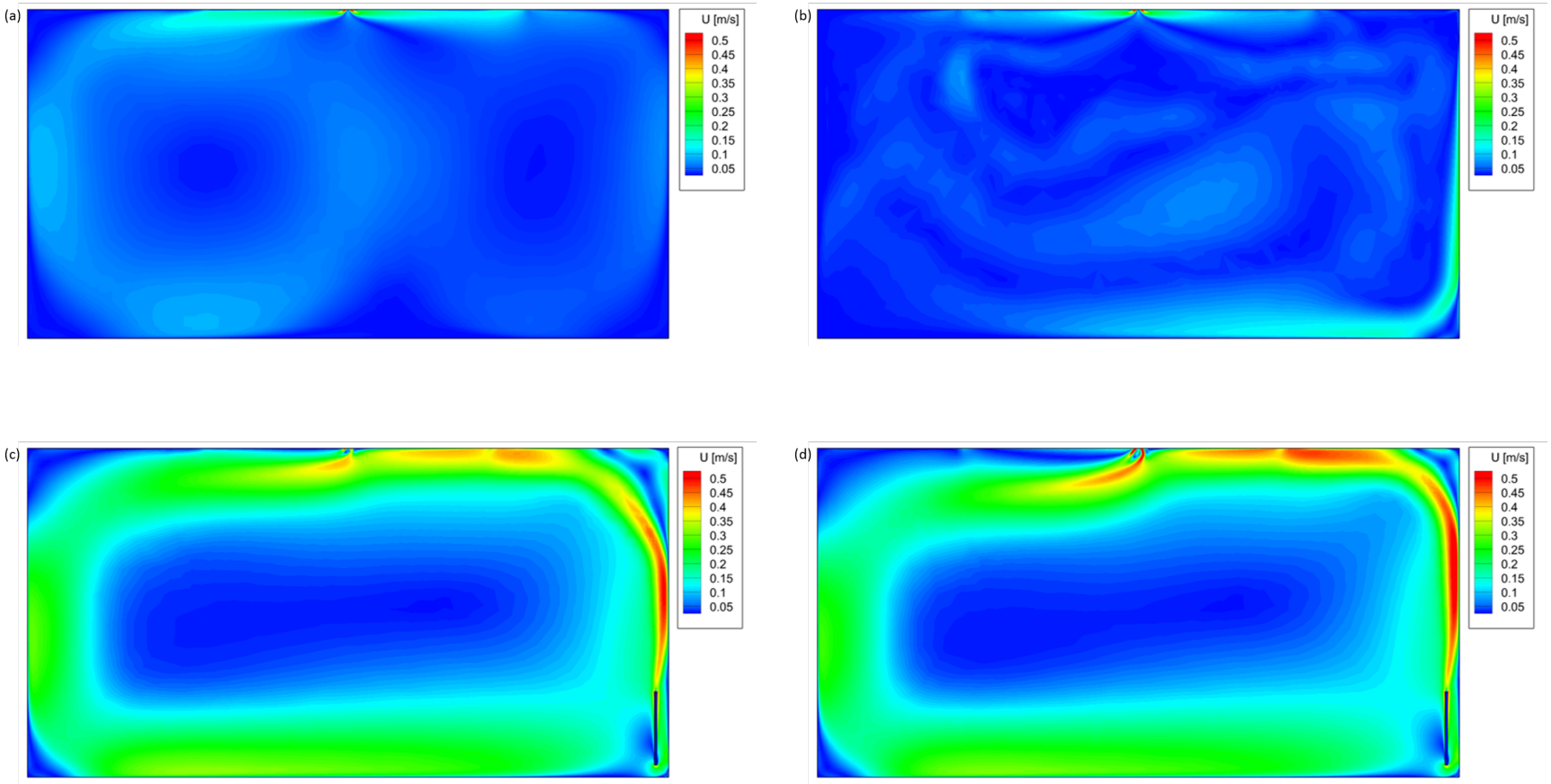

Figure D.3: Contour plot of the velocity magnitude U: (a) isothermal. (b) temperature facade. (c) including radiator. (d) increased inflow velocity

E — Velocity vectors and streamlines

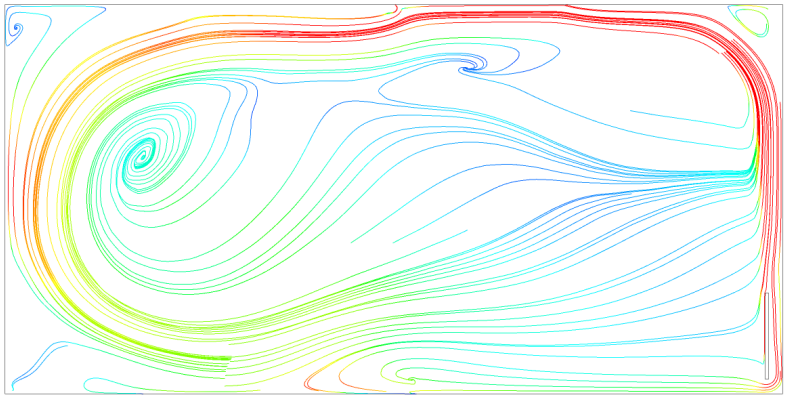

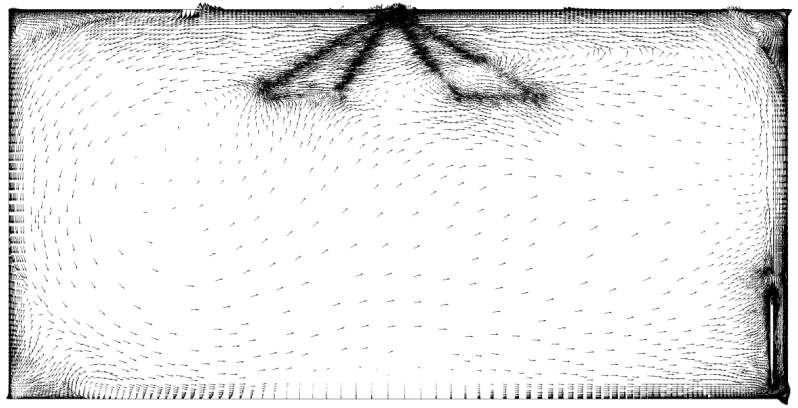

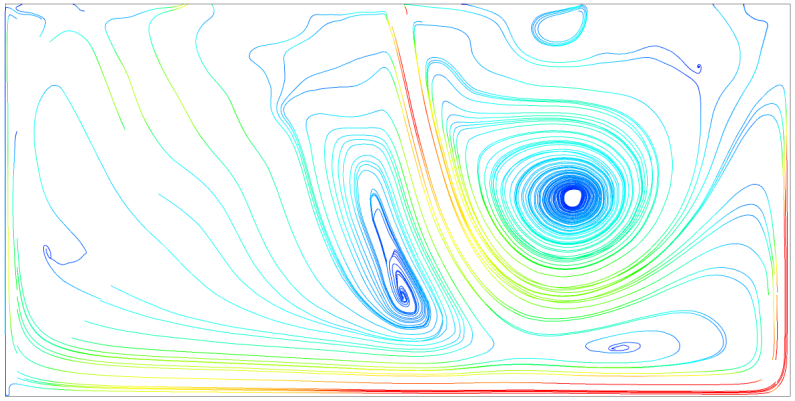

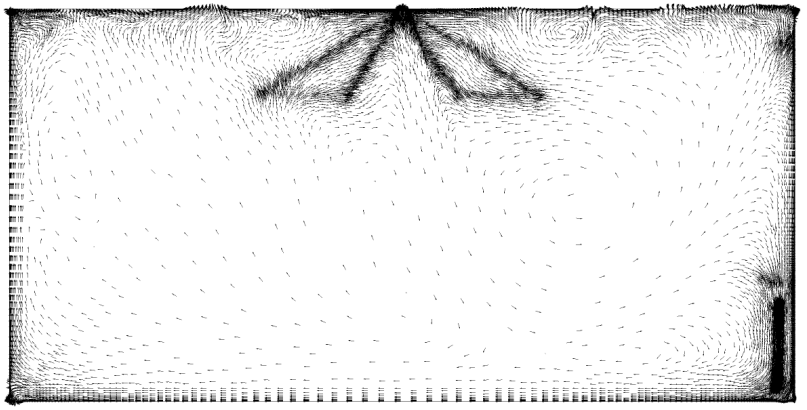

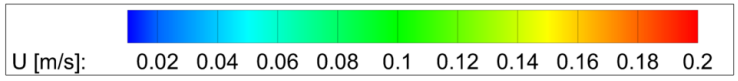
U [m/s]:
0.02
0.04
0.06
0.08
0.1
0.12
0.14
0.16
0.18
0.2

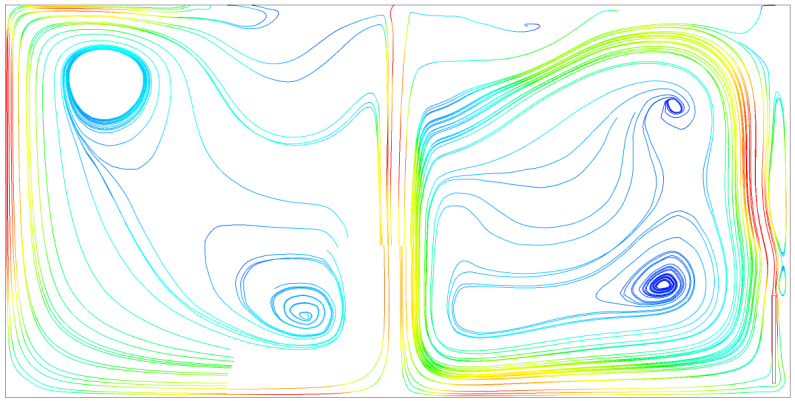

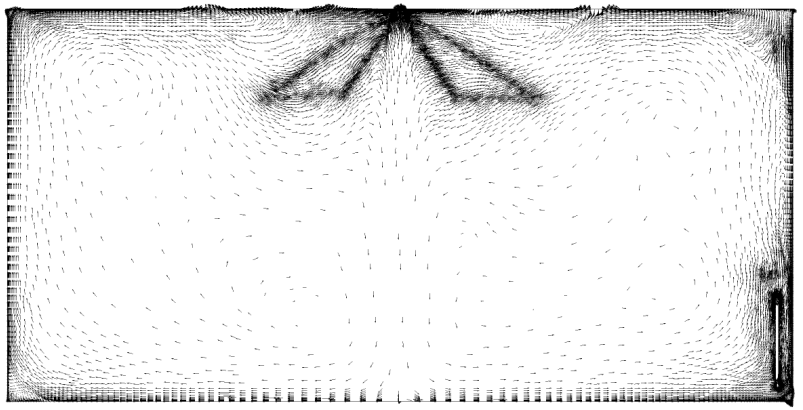

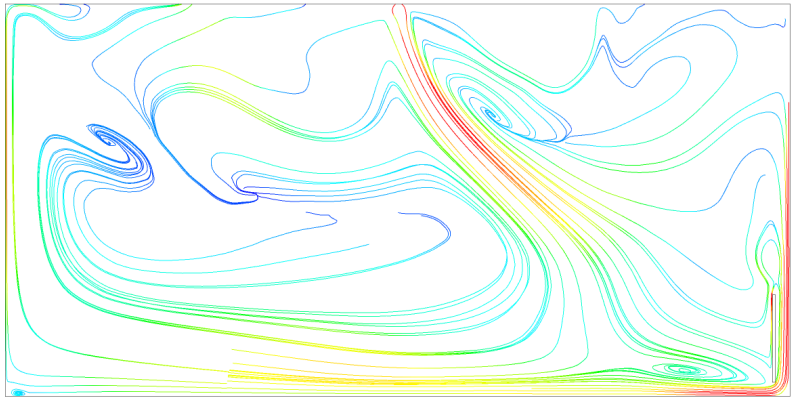

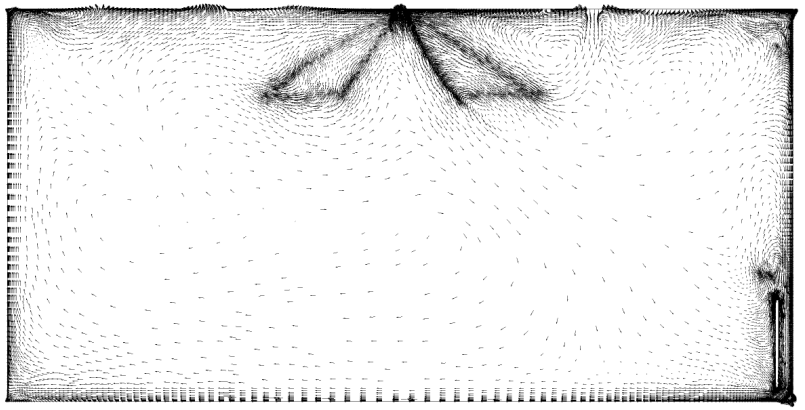

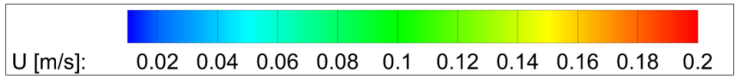
U [m/s]:
0.02
0.04
0.06
0.08
0.1
0.12
0.14
0.16
0.18
0.2

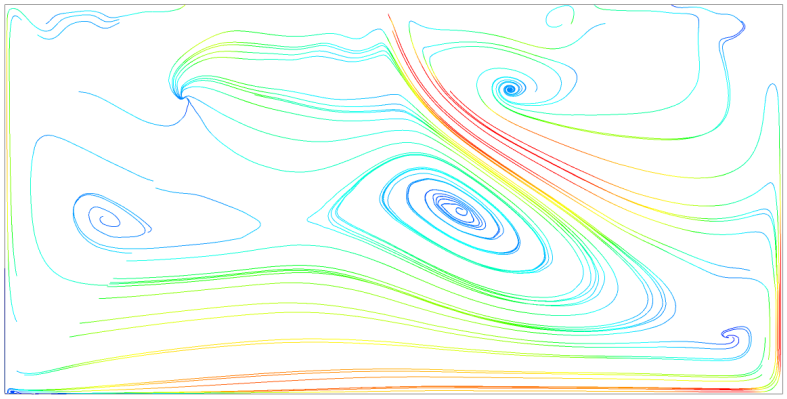

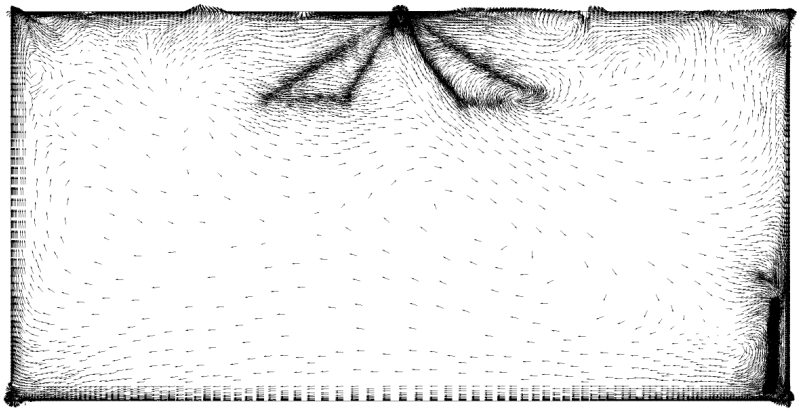

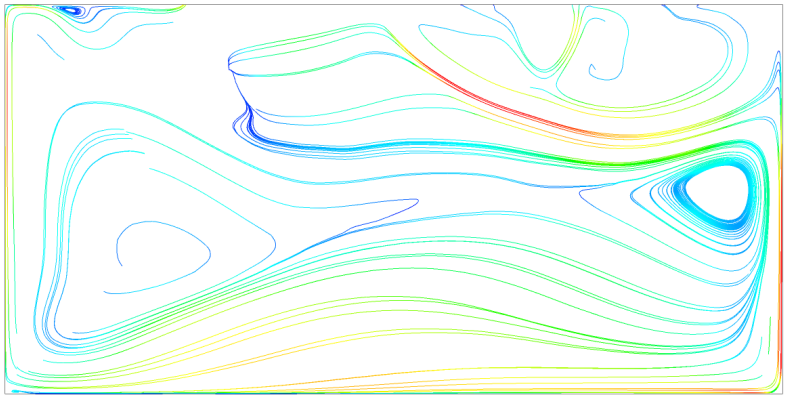

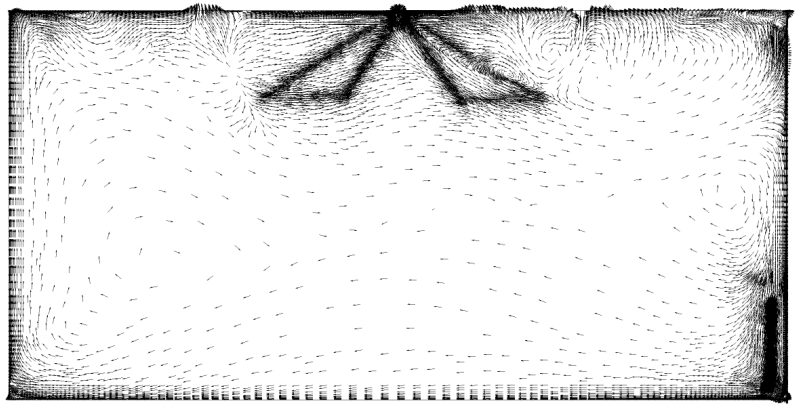

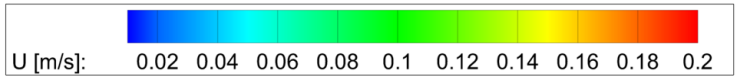
U [m/s]:
0.02 0.04 0.06 0.08 0.1 0.12 0.14 0.16 0.18 0.2